

Onset of Maikop sedimentation in the Talysh (Azerbaijan): climate or tectonics?



Section AZ15 - Arkevan and Pirembel formations in the Talysh Mountains - South Azerbaijan

MSc thesis Annique van der Boon

January 2012

Department of Earth Sciences – Utrecht University

Abstract

The Maikop series are composed of a thick succession of black shales, and are considered the most important source rock for hydrocarbons in the Caspian basin. The type section of this formation is located near the city of Maykop in Russia, north of the Greater Caucasus. Corresponding anoxic sediments can be traced in a vast area from Austria to China. Deposition of these sediments is linked to anoxic conditions that prevailed since the birth of the Paratethys and are related to decreased basin circulation. Due to the lack of (micro) organisms or ash layers, the onset of Maikop deposition has not been dated accurately so far. The Maikop is presently assumed to be of Oligocene to Miocene age. Precise dating of the start of Maikop sedimentation could aid in understanding the role of tectonics and climate change on the onset of anoxia in the Paratethys basin, as both have affected the region during the Paleogene. The Arabia-Eurasia collision has caused uplift, which could have caused a restriction in interaction with the Tethys Sea further south. Alternatively, basin restriction might have been caused by a major glacio-eustatic regression, associated with the transition from greenhouse to icehouse climate around the Eocene-Oligocene transition (EOT). In the Talysh, the mudstone-dominated sedimentary succession of the Pirembel formation is over 1.5 kilometers thick. This formation is generally interpreted as the lower part of the Maikop series. A multidisciplinary stratigraphic approach is used in this study, integrating magneto- and biostratigraphy of the transition to the Pirembel formation, combined with radiometric dating and geochemical analyses of the volcanic formation that underlies the Pirembel formation.

Three sections (AZ14, AZ15 and AZ16) were sampled. Biostratigraphic analyses have aimed at dinoflagellates, large benthic foraminifera and nannoplankton. Additionally, samples have been analyzed using magnetostratigraphy, thin sections and x-ray fluorescence. Ten samples were prepared for Ar-Ar dating. All samples were barren for dinoflagellates. Large benthic foraminifera were found in the base of sections AZ14 and AZ15 and interpreted to be of Priabonian age. Nannoplankton analyses place section AZ15 within Mediterranean nannoplankton zones MNP18 and MNP19, which are also within the Priabonian. Magnetostratigraphic analyses of section AZ14 have not yielded any high quality results due to (at least partly) remagnetization. Magnetostratigraphy places the base of section AZ15 in chron C17n.2n. The youngest chron that seems evident is C16n. A sedimentation rate is estimated for section AZ15 of 18 cm/kyr. Using this rate, the base of the section is estimated at 38 Ma, the base of the Pirembel formation at 37.3 Ma and the top of the section at 35.1 Ma. Deposition of the Pirembel formation, taken by some researchers as the onset of the Maikop series consequently started before the EOT. If the Pirembel formation truly represents anoxic sediments of the Maikop series, the anoxia is most likely related to a restriction in basin circulation caused by tectonics. Slumps and olistostromes are indicative for an active tectonic regime, as well as the presence of around 2 km of volcanics of the Peshtasar formation, just below the Pirembel formation. However, around 37.3 Ma, the formation of the first Antarctic ice sheets is reported, which might result in a drop in sea level, leading to basin restriction. A climatic cause can thus not entirely be ruled out.

Volcanics are trachybasalts and basaltic trachyandesites with trace element signatures characteristic for arc-lavas, and are interpreted to have formed in an arc setting. This is in contrast with previous interpretations that placed these volcanics within a back-arc setting. Basalts were not affected by

assimilation and fractional crystallization processes, and are all primary melts. Three groups are evident within section AZ16, both paleomagnetically and compositionally. These groups probably represent three short, intense episodes of magmatism. The basalts of section AZ14 can be linked to the middle and upper group of section AZ16. All basalts have shoshonitic compositions and are possibly linked to slab-breakoff during the Paleocene-Eocene.

Introduction

The Maikop series were deposited in the Paratethys, an epicontinental sea, which extended from Germany to China during the Paleogene. The type section of the Maikop is near the city of Maykop in Russia, north of the Greater Caucasus. Equivalent sediments to the Maikop have been described in Turkey, Romania, Austria, Turkmenistan, Ukraine and Iran. The Maikop series consist of black shales that are the most important source rock for hydrocarbons in the South Caspian basin and thus of great economic importance. Black shales contain a relatively large amount of unoxidized carbon, and are usually deposited in anoxic, reducing conditions (Passier et al., 1999; Efendiyeva, 2004; Hudson et al., 2008; Johnson et al., 2010). Oxygen levels were lowest during deposition of the lower part of the Maikop series (Rupelian, according to Hudson et al., 2008) but generally ranged from anoxic to suboxic (0.0-0.2 ml/l O₂; Hudson et al., 2008). Anoxia is associated with stagnant water columns, which are related to decreased basin circulation (Tyson and Pearson, 1991; Soták, 2010). The start of Maikop (or equivalent) sedimentation thus marks a major change in conditions in the Paratethys basin. Due to the lack of (micro) organisms, often used for dating, onset of Maikop deposition is still poorly constrained. Precise dating of the Maikop series is important for accurate reconstructions of the paleoenvironment and tectonic setting during the time of birth of the Paratethys. The prevailing hypotheses suggest that deposition of the Maikop has started from the Eocene-Oligocene boundary onwards, continuing into the Miocene (Abrams and Narimanov, 1997; Hudson et al., 2008; Popov et al., 2008). If the onset of anoxia starts around the Eocene-Oligocene transition (EOT), anoxia is likely to have been caused by the eustatic sea level lowering that is observed during this interval (Zachos et al., 2001). This drop in sea level could then result in a cutoff of large-scale oceanic currents in the Tethys Ocean, flowing from the Indian Ocean to the Atlantic Ocean, because during the Cenozoic, ocean circulation was markedly different from that of recent times (Von der Heydt and Dijkstra, 2008). Anoxia might have, in turn, increased carbon burial, leading to further global cooling. If, however, the onset of anoxia already starts during the Eocene, the anoxia might be caused by the collision of Africa and Arabia with Eurasia, resulting in buildup of relief, which could in turn cause a cutoff of oceanic currents. Nonetheless, the exact timing of the Arabia-Eurasia collision is still poorly constrained. If the collision resulted in the first buildup of relief around the EOT, the respective roles of climate and tectonics are difficult to distinguish.

This research aims on dating the onset of Maikop deposition in the Talysh, in order to resolve the onset of anoxic conditions in the Paratethys basin and see whether they are related to climate change at the EOT or collision of Arabia with Eurasia. A multidisciplinary stratigraphic approach is used in this study, based on magnetostratigraphy, biostratigraphy and XRF analyses. Obtaining constraints on timing of the onset of anoxia is crucial for accurate reconstructions of tectonics and paleoenvironments within the Arabia-Eurasia collision zone.

Even though most of the Maikop series is situated very deep in the subsurface of the Caspian basin, good outcrops are located in the Talysh Mountains in Azerbaijan. Over 500 samples were taken of three sections, AZ14, AZ15 and AZ16. Section AZ14 consists of sandstones, siltstones and basalts. Section AZ15 is a sedimentary succession with sandstones, siltstones and shales. Section AZ16 comprises mostly of basalts, with very few sedimentary beds in between. XRF analyses of the basalts were done in order to obtain information on the magmatic setting in which they were formed. Previous interpretations linked basalts to back-arc spreading (Vincent et al., 2005; Verdel et al., 2011) or ocean spreading in a back-arc system (Golonka, 2004). Furthermore, samples of various lithologies (sandstones, siltstones, shales) have been taken for biostratigraphic analyses, and Ar-Ar dating was performed on basalts of the two different formations that contained volcanics.

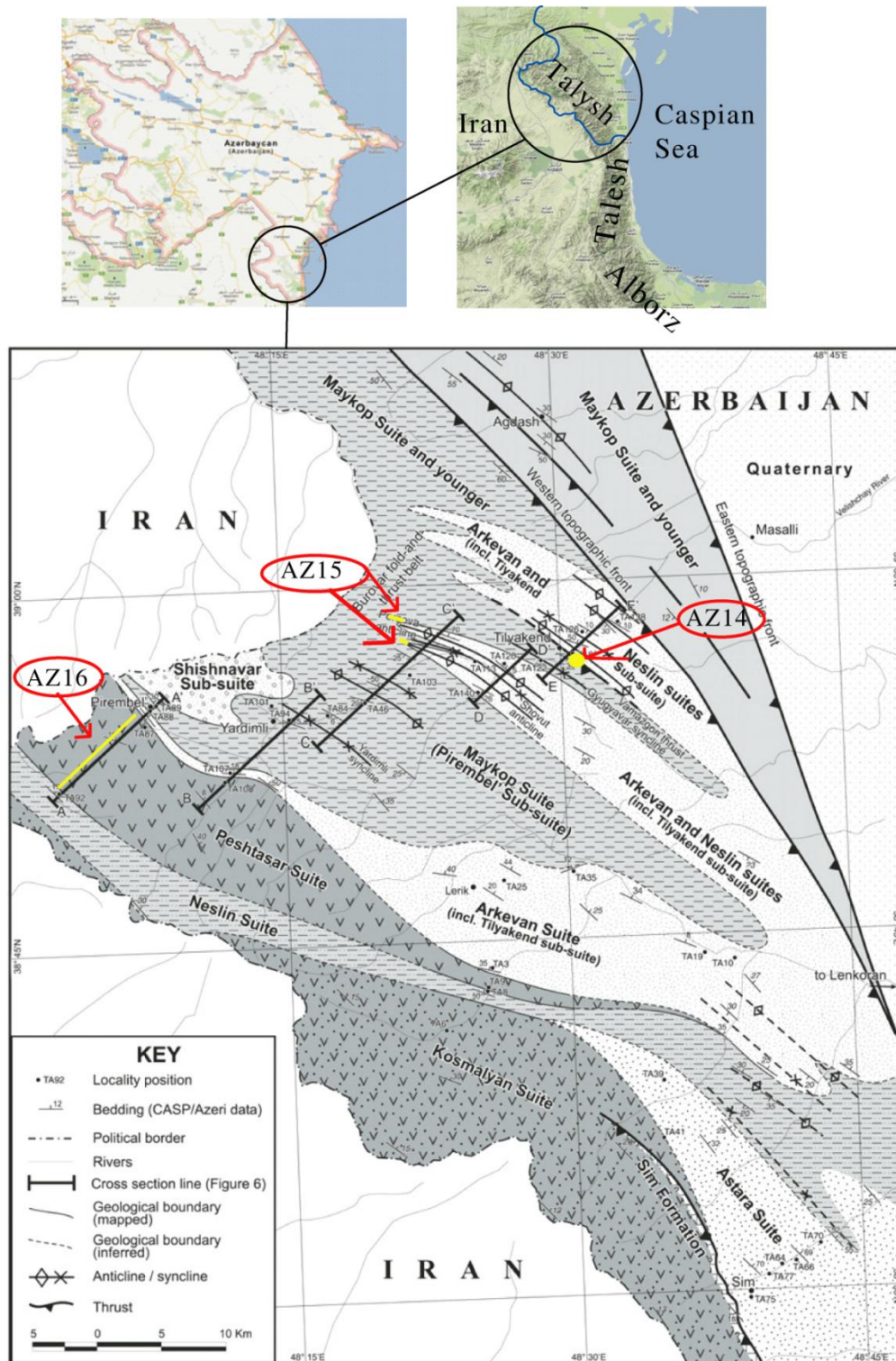


Figure 1: Location of the Talysh, Iranian Talesh and Alborz Mountains (Google maps) and sampled sections of this study plotted on the geological map of Vincent et al. (2005)

Geological background

Regional Geology

The Talysh Mountains are situated in the southernmost part of Azerbaijan, bordering the Caspian Sea. The Talysh is located within the active collision zone between Arabia and Eurasia, and continue into the Iranian Talesh, which forms the western part of the Alborz mountain belt. The Alborz Mountains pass into the Kopet Dagh in the east. (See Figure 2) Lithology of the Talysh is made up of a succession of Eocene volcanics and Eocene-Oligocene sediments. The volcanics are mainly high-K alkali basalts which are interpreted to have formed due to back-arc spreading (Vincent et al., 2005; Asiabanha and Foden, 2012), even though previous studies have shown geochemical signatures characteristic for arcs rather than back-arcs (Vincent et al., 2005; Verdel et al., 2011). Back-arc spreading has been reported for the Mesozoic, according to Zonenshain & Le Pichon (1986). However, no remnants of Mesozoic back-arc related volcanism are found in the Talysh. Only a very limited amount of pre-Paleogene rocks are reported from the Talysh, comprising limestones from the Sim formation, which belong to the sedimentary basement of the Talysh (Vincent et al., 2005). As the Talysh in Azerbaijan is connected to the Alborz, the basalts are linked to the Alborz Magmatic Arc (AMA), which is present in the Iranian Talesh (Asiabanha and Foden, 2012). Further to the south of the Talysh, another magmatic belt of Eocene age is present, the Urumieh-Dokhtar Magmatic Arc (UDMA, see Figure 2). The Zagros-Bitlis suture zone lies even further south of the Urumieh-Dokhtar Magmatic Arc, and is generally assumed to be the area along which the Tethys Ocean closed, (Agard et al., 2011; Asiabanha and Foden, 2012; Mouthereau et al., 2012) due to the subduction of the Arabian plate underneath the Eurasian plate. The UDMA consists of arc magmas related to this subduction (Berberian & King, 1981) and is generally considered as the main magmatic arc, while the AMA is located further away from the subduction zone (Asiabanha & Foden, 2012). This has led to the assumption that the AMA is caused by back-arc spreading (Vincent et al., 2005; Asiabanha & Foden, 2012). The AMA and Talysh are linked by several authors to the Achara-Trialet zone of Turkey and Georgia (see Figure 2). (Brunet et al., 2003; Golonka, 2004; Adamia et al., 2011; Asiabanha and Foden, 2012) However, during the Eocene, these two areas were probably separated by a plate boundary (Van Hinsbergen, personal communication), so this assumption seems unlikely. Also, volcanics from the Talysh are more alkalic (Adamia et al., 2011). As the northward movement of the Arabian plate continued, the back-arc basins were eventually inverted when the Arabian continent collided with Eurasia. Normal marine basins transformed to enclosed basins when the Paratethys emerged, resulting in anoxic conditions (Adamia et al., 2011). After deposition of the Maikop series, the back arc basins in the Paratethys began to close, as the Arabian block began to collide with the island arc further south of the Talysh (Zonenshain & Le Pichon, 1986).

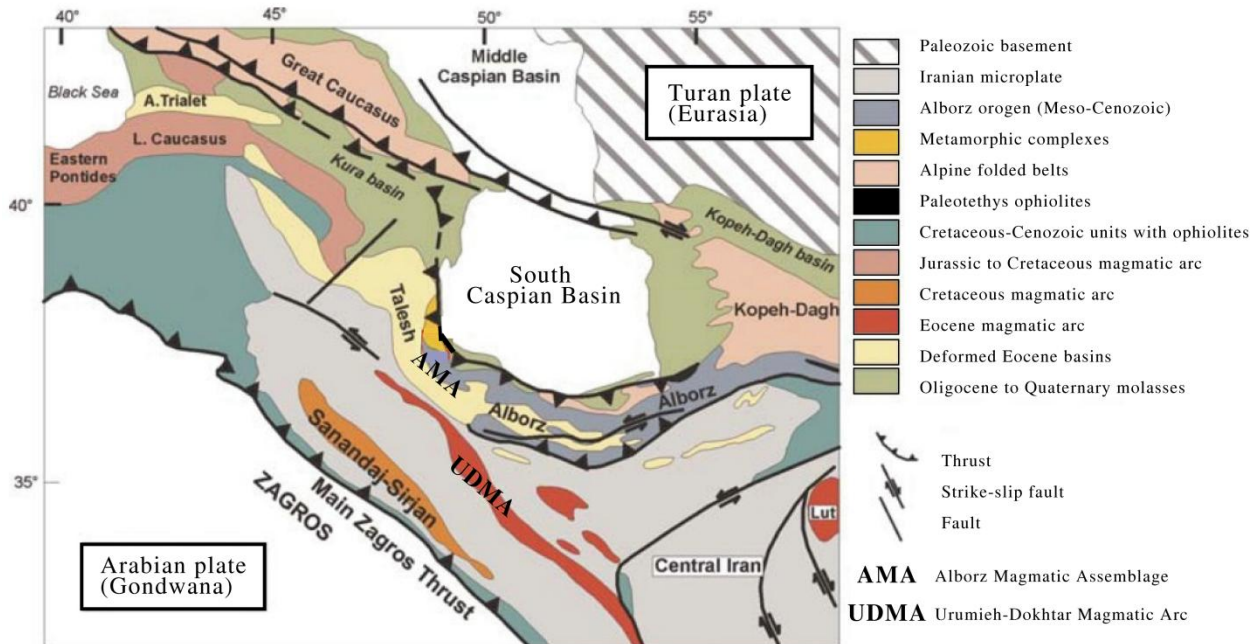


Figure 2: Simplified tectonic map, showing the positions of the Talesh, Alborz Magmatic Assemblage and Urumieh Dokhtar Magmatic Arc (modified after: Zanchetta et al., 2009)

Geology of the Talysh

In the Talysh (apart from the minor amount of Mesozoic limestones of the Sim formation) rocks of Paleogene and younger age are present. Paleocene and Eocene rocks comprise mostly volcanics and volcanogenic sediments, although consensus on the precise age is still lacking (See Table 1 and Table 2) (Azizbekov, 1972; Vincent et al., 2005). Oligocene rocks consist of only sediments and no volcanics. According to Table 1, the Oligocene within the Talysh can be divided into three zones: the Tilyakend formation, the Pirembel formation and the Shishnavar formation. Since the term Maikop is often used as a chronostratigraphic unit, comprising the whole Oligocene and the lower part of the Miocene (Popov et al., 2008), the Tilyakend, Pirembel and Shishnavar formations are all attributed to the Maikop.

The Maikop series throughout Azerbaijan and the South Caspian basin is divided into two subformations. The lower subformation is generally assumed to have been deposited during the Oligocene, while the upper is of Miocene age (Abrams and Narimanov, 1997; Efendiyeva, 2004). This study focuses only on the transition to the Maikop. The two subformations have different oil-generating prospectives, the Oligocene having a lower content of organic matter, but better oil-generating properties compared to the Miocene subformation (Guliyev et al., 2001). The lower subformation is related to the Khadum and Khatian regional stages (Oligocene, (Efendiyeva, 2004). (However, these regional stages are not commonly used, so the regional stages as mentioned in (Popov et al., 2004) are preferred.) These stages roughly correspond to the Pshekhian, Solenovian and Kalmykian stages of the Oligocene, see Figure 3 (Popov et al., 2004). Stratigraphy of the lower subformation is characterized by clayey deposits and sandy-clayey deposits intercalated with conglomerates. The upper subformation is overall more fine-grained and consists of clay-rich laminated shales with few layers of marls and sandstones (Efendiyeva, 2004). The upper subformation is related to the Caucasian, Sakaraulian and

Kozakhurian regional stages (Efendiyeva, 2004; Popov, 2004). The Caucasian stage is not widely used, and is broadly related to the Karadzalganian stage (Popov et al., 2004), see Figure 3. The study of Vincent et al. (2005) suggests that the Shishnavar formation is also Oligocene in age, based on similar sediments across the Iranian border.

A geological map of the Talysh has been made by Russian geologists in 1972. This research (in: Azizbekov, 1972) distinguishes the formations (or suites, the Russian expression that has been adopted by many researchers) as shown in Table 1. According to this study, the Astara formation is of Paleocene age, with the Kosmalyan formation of Lower Eocene age unconformably deposited on top. This unconformity between the Astara and the Kosmalyan formations is not observed in the study of Vincent et al. (2005). The research of Vincent et al. (2005) suggests that the Astara formation (consisting of tuffaceous sandstones, siltstones and mudstones) is the sedimentary lateral equivalent of the Kosmalyan formation (of volcanic origin). Ar-Ar dating on samples from a sill intruded in the Astara formation constrain the lower part of the Astara formation as older than 40.7 Ma, which would mean Lutetian or older (Vincent et al., 2005). The Neslin formation is interpreted as a sedimentary interval between the two main volcanic formations, the Kosmalyan and the Peshtasar formations (Vincent et al., 2005). The Arkevan formation is a sandstone-dominated succession that is interpreted as partly the lateral equivalent of the Peshtasar formation (Vincent et al., 2005). The thickness of the Arkevan formation varies considerably (see Figure 1), having a minimum thickness stratigraphically just above section AZ16, and thickening towards the east. The study of Vincent et al. (2005) mentions that the Tilyakend formation (which, according to Russian literature is part of the Maikop) is lithologically indistinguishable from the upper part of the Arkevan formation and regards the Pirembel formation as part of the Maikop. The transition from sandstone-dominated Arkevan formation to the mudstone-dominated is, according to Vincent et al. (2005) poorly defined, as both formations are deposited by turbidity processes. The Maikop series are classically described as mudstones and shales with fish remains (Popov et al., 2008; Hudson et al., 2008). It remains questionable whether this 'classical' Maikop is at all present in the Talysh, as sediments generally seem more coarse-grained (See Table 1; Azizbekov, 1972; Vincent et al., 2005).

The boundaries between the formations are hard to define, as several formations are interpreted as lateral equivalents of each other. Thorough geological mapping is required, to provide a more detailed geologic map in which this problem may be solved. Samples of this study are assigned to formations based on their locations (according to the schematic geological map of Vincent et al., 2005). Samples from section AZ16, accordingly, are part of the Peshtasar formation. In Figure 1, the locations of AZ14, AZ15 and AZ16 are plotted on the geological map of Vincent et al. (2005). This shows that sections AZ14 and AZ15 are on the boundary between the Arkevan – Neslin – Tilyakend formation and the Pirembel formation. Section AZ16 covers the Peshtasar formation, where the lowest sampled flow, AZ16A, is located just above the sands of the Neslin formation.

Epochs	Stages	Eastern Paratethys units		Hydrological regime	Climate						
Eocene	Priabonian	Maikop Series	Eastern Paratethys units	Beloglianian	Marine polyhaline	Subtropical					
	Rupelian						?	Solenovian			
	Chattian							Pshekhian			
	Oligocene						Aquitanian	Kalmukian	Kara-dzalgalanian	Marine with normal salinity	Humid, warm-temperate
	Early Miocene						Burdigalian	Tarkhanian	Polyhaline	Warm, seasonal, moderately humid	
											Middle Miocene
								Karaganian	Freshening		

Figure 3: Global stages and regional stages of the Eastern Paratethys with hydrological regime and climate (modified after Popov et al., (2004, 2008))

		Formation (suite)			Thickness (m)
Oligocene	Upper	Shishnavar		Sandstone, conglomerate, clay	450-1300
	Middle	Pirembel		Clay, sandstone	220-1100
	lower	Tilyakend	Part of Avdusina fm	Marl, clay, sandstone	Up to 800
Eocene	Upper	Arkevan	Avdusina fm 'd'	Mudstone, siltstone, tuff	Up to 800
	Middle	Peshtasar	Avdusina fm 'c'	Andesite, basalt, tuffbreccia, (minor) shale	1000-1200
		Neslin	Avdusina fm 'b'	Tuff sandstone, tuff conglom, clay, marl, tuffite	500-1000
	Lower	Kosmalyan	Avdusina fm 'a'	(cover?)Basalt, andesite, tuff breccia, tuffite, conglomerate	800-1300
	unconformity	unconformity		unconformity	unconformity
Paleocene		Astara		Tuffs, green silt, mudstone, marl	550-800

Table 1: Stratigraphy of the Talysh, translated from Russian literature (Azizbekov, 1972)

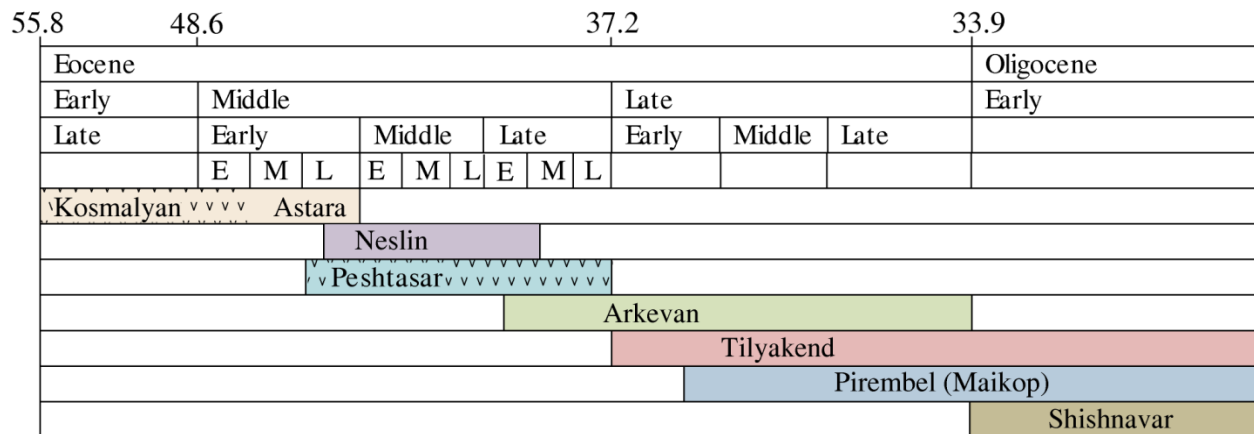


Table 2: Stratigraphy of the Talysh, according to Table 1 from the study of Vincent et al. (2005)

Methods and Materials

During the fieldtrip that was carried out in August 2011, over 500 samples were drilled using a gasoline-powered drilling machine and an electrical drilling machine. Conventional paleomagnetic core plug samples were drilled, orientated by a compass. All core samples were cut to the same size of

approximately 22 millimeters. As the basalts had a very strong magnetic signal, these samples were subsequently cut in half. The samples were subjected to thermal and/or alternating field demagnetization. Temperature increments of 20-60°C were applied to thermally demagnetize the samples in an oven, to a maximum temperature of about 580°C for basalts and about 400°C for sediments. This temperature is chosen to avoid thermal alteration during heating of the samples. Some samples were demagnetized using alternating field (AF) demagnetization after heating. Samples were heated (up to temperatures of 150, 175 or 200°C) before AF demagnetization in order to avoid alteration by a chemical remanent magnetization (CRM). These samples were demagnetized stepwise, applying steps of 5 mT, up to 100 mT. The natural remanent magnetization (NRM) after each demagnetization step were measured on a 2G Enterprise horizontal cryogenic magnetometer equipped with three DC SQUIDS (noise level 3×10^{-12} Am²). Results were plotted in orthogonal demagnetization plots (Zijderveld, 1967) and characteristic remanent magnetization (ChRM) directions were determined using principal component analysis (Kirschvink, 1980). Declination and inclination angles were calculated for both a possible overprint and a pre-tilt signal, before (notc) and after tectonic correction (tc) (if applicable). Mean directions were determined for subsections using standard Fisher statistics. Great-circle analyses were used in order to isolate components that were not completely removed after demagnetization. Magnetic susceptibility of samples was measured at room temperature. Two types of thermomagnetic measurements were done, using Kappabridge and Curie balance.

Magnetic susceptibility

The magnetic susceptibility at room temperature of every second sample of AZ15 was measured, using the AGICO KLY-3. Measured values for the susceptibility are divided by the weight of the sample, which gives the specific susceptibility. Changes in magnetic susceptibility throughout a section may reflect climatic or tectonic changes, as these often lead to a variation in input of detrital material in sediments (Hay, 1996, 1998; B. Ellwood et al., 2000). The variations in magnetic susceptibility could also be caused by changing contributions of para- and diamagnetic minerals, biogenic carbonate production or processes that take place during diagenesis. Diagenetic processes that can play a role are dissolution and sulphidization. Sulphidization creates new magnetic minerals, such as greigite and pyrrhotite (Bernier and Raiswell, 1983; Bernier, 1984; Wilkin and Barnes, 1996; Roberts, 1995).

Thermomagnetic measurements

Curie balance

Samples of different lithologies were measured on the Curie balance, to determine which magnetic minerals are present in the samples. Samples were crushed to powder, of which a small amount was subjected to thermomagnetic analysis in air using a modified horizontal translation Curie balance (Mullender et al., 1993). Six heating and cooling cycles were performed, up to a temperature of 700°C, during which magnetization of the sample is measured.

Kappabridge

Kappabridge measurements were performed on crushed basalt samples, using the AGICO KLY-3 with a CS-3 furnace attachment. Six heating and cooling cycles were performed on powdered samples up to a

temperature of 600°C. Samples are repeatedly heated and cooled, after which the susceptibility is measured.

NRM

Of section AZ14, at least 7 samples were taken of each site. Sediments in between the volcanics were also sampled, leading to a total of 22 sedimentary samples. Demagnetization procedures were similar to those mentioned for section AZ15 for sediments, and AZ16 for volcanics. Great-circle analyses were performed for basalts, when required.

Of section AZ15, 221 samples were demagnetized in various ways. Samples were demagnetized thermally, up to a temperature of 400°C. Another part of the samples was demagnetized using three or five (20°, 100°, 150° and sometimes also 175° and 200°) steps of thermal demagnetization and were further demagnetized using alternating field (AF) demagnetization. Half of the samples were subjected to a temperature of 150° C and subsequently demagnetized using AF demagnetization. The temperature of 150° C was chosen to remove possible overprints caused by weathering (Van Velzen and Zijdeveld, 1995). AF demagnetization was performed from 0 to 100 mT in 15 or 18 steps of 4 to 10 mT in an alternating field demagnetizer, using a robotized 2G DC-SQUID cryogenic magnetometer (noise level $1-2 \times 10^{-12} \text{ Am}^2$) with demagnetization coils attached to the system.

Of section AZ16, 26 sites were sampled. At least 7 cores were taken of each site. All sites were located in different magmatic cooling units (flows or sills). A profile was made onto which all flows were transferred, according to the respective strike. Relative stratigraphic distances were then calculated of the flows on the profile. Samples were demagnetized by AF demagnetization (using 18 steps of 4 to 10 mT) up to 100 mT. Additionally, from each flow, two samples were demagnetized thermally, using 16 steps of 20° to 80° up to a temperature of 580°C.

Ar-Ar dating

Ten sites were selected for Ar-Ar dating, of which two are from the pilot study of 2009. Sanidines, groundmass, hornblende and plagioclase can be used in Ar-Ar dating. This study aimed on selecting sanidines and groundmass. All samples were crushed and sieved through 250 µm, 500 µm and 1000 µm meshes, resulting in four fractions for each sample (<250 µm, 250-500 µm, 500-1000 µm and >1000 µm). Target minerals and groundmass were separated from the rest of the samples by density separation, using heavy liquids. After density separation, the target minerals were etched with HNO₃, in order to clean any impurities. Samples were put in HNO₃ for around 20 minutes (except sample 6, AZ16D, which was accidentally left in HNO₃ for one weekend). To remove any remaining unwanted minerals, another separation step was performed, using a Frantz magnet. All target minerals were then picked using a microscope. Samples containing sanidine were also subjected to HF leaching. Samples were then irradiated, and left for 6 months. As irradiation of the samples took place in late August 2012, measurements have not been performed yet, but will be performed probably in February 2013.

Sample	Sanidine	Groundmass
1 (AZ14A)		X
2 (AZ14D)	X	X
3 (Arkevan, AZ03)	X	X
4 (Pirembel, AZ08)		X
5 (AZ16A)		X
6 (AZ16D)	X	
7 (AZ16N)		X
8 (AZ16S)	X	X
9 (AZ16V)	X	X
10 (AZ16Y)	X	X

Table 3: Samples that were used for Ar-Ar dating. Samples AZ03 and AZ08 were taken during the pilot study of 2009 and are from the Arkevan and Pirembel formations.

Geochemistry

Geochemical analyses of all volcanics of sections AZ14 and AZ16 were performed at the VU in Amsterdam, using x-ray fractionation (XRF) in order to measure the chemical composition. The creation of the beads at the VU was problematic (for a more detailed report of the problems, see the appendix). Samples were crushed using a jawbreaker, then powdered using several agate mills. After powdering, powders were dried overnight in a stove at 110°C. Of each sample, a bead was made, for major element analysis. Samples were oxidized for half an hour, in a muffle furnace, at a temperature of 1000°C. Samples were weighed before and after heating, in order to calculate the loss on ignition (LOI), which is the amount of constituents that the sample loses during heating to 1000°C. This loss is a combination of escaping H₂O, CO₂, F, Cl, S and in parts also K and Na. Added compounds during heating are O₂ (i.e. FeO -> Fe₂O₃) and later CO₂ (CaO -> CaCO₃). After oxidation, about 1.0 gram of sample was mixed with four times this amount of flux (lithiummetaborate, LiBO₂), to lower the melting point. Samples were subsequently shaken for 10 minutes. The mixture of sample and flux was placed in a platinum crucible in the PerI'X3 furnace, in which the powder is oxidized (although it is assumed that all oxidation has already taken place in the oven), melted and cast onto a platinum dish. Pellets are created of dried, unoxidized powder, which is mixed with a binding resin (EMU powder). About 4.5 grams of sample are mixed with 10 percent EMU and mixed for 15 minutes. Pellets are pressed under a pressure of 20 tons. Beads and pellets are analyzed using different programs of XRF, on the Panalytical MagiX Pro (PW2440). Beads are analyzed using the Majorrh1-4 program, which measures the major elements: Na, Mg, Al, Si, P, K, Ca, Ti, Mn, Fe and Ba. Because samples were oxidized before casting of the bead, the actual constituents that are measured are: Na₂O, MgO, Al₂O₃, SiO₂, P₂O₅, K₂O, CaO, TiO, MnO, Fe₂O₃ and BaO. Pellets were analyzed using four different programs: SPEL, Reehex27, Metals and VCrCoBaSc. The SPEL program, measures the amounts of Rb, Sr, Y, Zr, Nb, Mo, Pb, Th and U. The Metals program measures the metals Ni, Cu, Zn, Ga, Hf, Ta, W, Dy, Er and Yb. Rare earth elements (REE) La, Ce, Pr, Nd and Sm were analyzed with the Reehex27 program. The elements V, Cr, Co, Ba and Sc were analyzed with the VCrCoBaSc program. Calibration of the Panalytical MagiX Pro was done using standards. Accuracy and precision for measurements is based (Handley et al., 2007) on the measurement of four international standards that were analyzed between 2003 and 2011 (and can be found on <http://www.falw.vu/~petrolab/xrf>).

Of all samples, the magnesium number is calculated. The magnesium number is a differentiation index that is based on the relative amounts of magnesium and iron in the rock. The magnesium number (M' or M#) is calculated by transforming all Fe₂O₃ to FeO, as the iron in the magnesium number is assumed to be Fe²⁺. This is done by dividing the weight percentage of Fe₂O₃ by 1.11. The amounts of magnesium and iron are subsequently divided by their molecular weights, to get the atomic ratio.

Petrography

Of each sampled unit of section AZ14 and AZ16, at least one polished thin section was made (by O. Stiekema), to assess the petrography and to select good samples for Ar-Ar dating of groundmass.

Biostratigraphy

In the lower part of sections AZ14 and AZ15, large benthic foraminifera were found. These foraminifera were analyzed by W. Renema, of Naturalis (Leiden). Of section AZ15, 11 sample bags were filled with black very fine silts (MP samples). These were analyzed for dinoflagellates by A. Grothe of Utrecht University, and for nannoplankton by G. Villa of the University of Parma.

Results

Lithostratigraphy and structures

Section AZ14 is located near Tilyakend. The section consists of sandstones, siltstones with sills and basalt flows in between. The section, according to Russian literature (see Table 1), is probably part of the Tilyakend formation. The study of Vincent et al. (2005) however, notices that the Tilyakend and Arkevan units are lithologically indistinguishable.

The lithostratigraphic log of section AZ15 is shown in Figure 4. Around 110 meters, there is a distinct change in lithology. Above this level, hardly any thick sand layers are present, whereas they are abundant below this level. Sands that are 1 meter thick or more are horizontally exaggerated, to show that thick sand beds decrease in abundance higher up in the stratigraphy. As mentioned in the study of Vincent et al. (2005) many synsedimentary deformation features, such as slumps and olistostromes are present, primarily in the lower part (Arkevan formation) part of AZ15. Also shown are the stratigraphic positions of the MP samples, which are used for biostratigraphic analyses. The part that is considered Maikop contains many dark grey to black very fine silt layers. Shales in the classical sense (that have a mud grain size, so no grains can be distinguished) are scarce, however.

Of section AZ16, no lithostratigraphic log is made, as different volcanic units were hard to distinguish in the field. In between the sampled sites there are probably more flows or sills, but this would require a more detailed study. The Peshtasar formation, according to the study of Vincent et al. (2005) is made up of lavas and pillow lavas with some interbedded sediments. Blocks of sediments and sedimentary intercalations within the section were found, between sites AZ16F and AZ16G and between AZ16K and AZ16L, indicating a period of magmatic quiescence. No pillows were observed, either in the field, or by examination of photographs by S. Branca (Istituto Nazionale di Geosifica e Vulcanologia - Sezione di Catania) and M. van Bergen (Utrecht University). Thin sections show rather large phenocrysts, and many

thin sections have a groundmass that is made up of plagioclase phenocrysts and is thus not as fine-grained as would be expected for pillow basalts. Furthermore, no preferred orientation of phenocrysts was found, or any other structures indicating flow (see appendix).

Many small faults are present in the area. Movement along faults seems to be in the order of meters to tens of meters. In particular section AZ15 contained many faults. Both normal faults and reverse faults are observed. Section AZ16 seemed more or less continuous, as well as section AZ14. However, section AZ14 may contain a fault, as the dip of the layers above flow AZ14F is towards the opposite direction, compared to all layers underneath the layer that contains AZ14.12. Figure 1, in which the location of the sampled sections is matched with the map of Vincent et al. (2005), shows that AZ14 is located near a thrust. The large scale anticlines as mentioned by Vincent et al. (2005) are the two locations along which section AZ15 is located. The axes of the anticlines run roughly NW-SE, which is parallel to the thrust faults mentioned by Vincent et al. (2005).

AZ 15

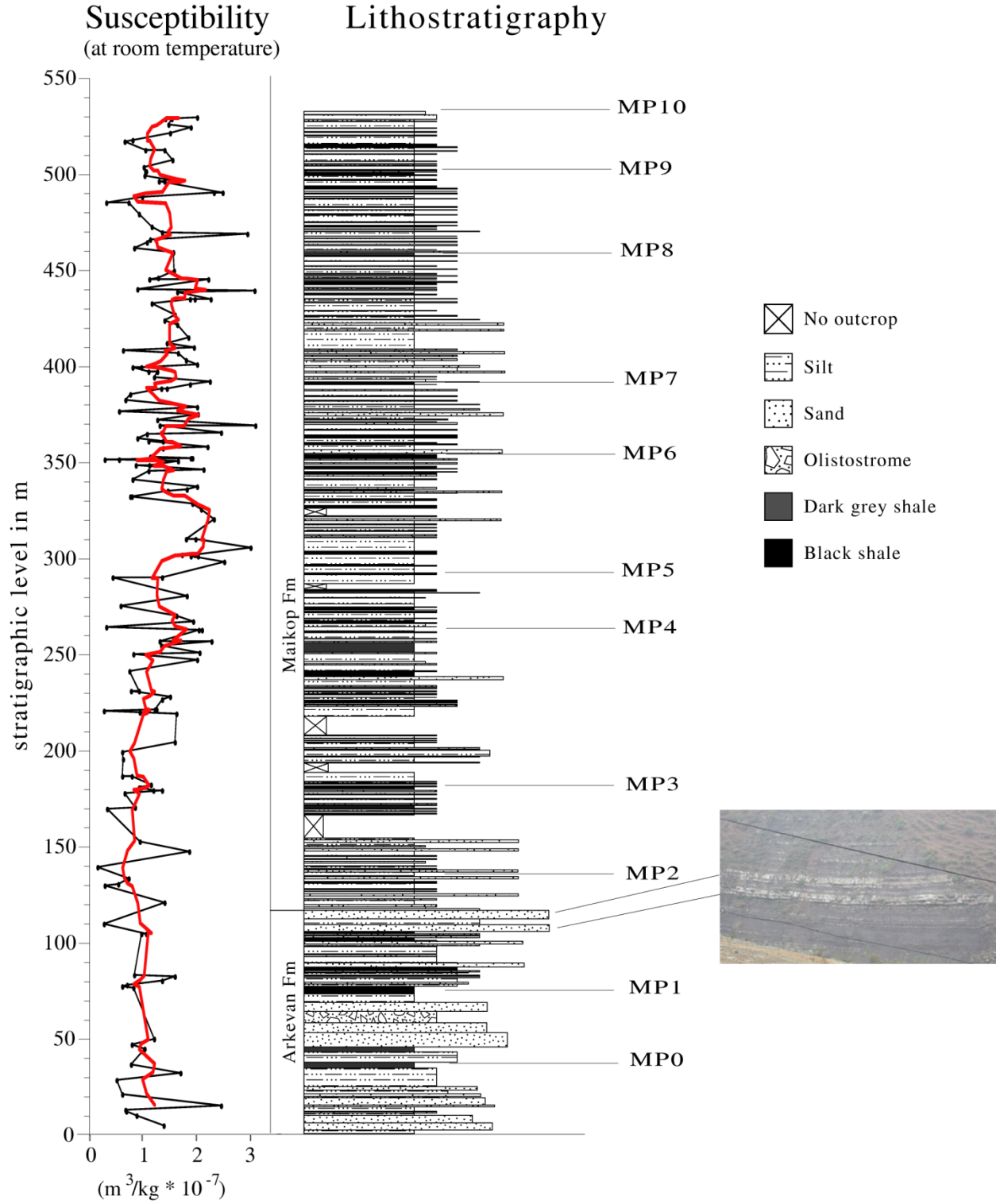


Figure 4: Magnetic susceptibility (in black) and moving average over 5 points (red line) and lithostratigraphic log of section AZ15 with photograph of marker beds that mark the end of the sandstone-dominated succession (Arkevan formation).

Rock magnetism

Magnetic susceptibility

From section AZ15, magnetic susceptibility at room temperature was measured from every second sample. From Figure 4 can be seen that the magnetic susceptibility is quite variable, but the moving average over 5 samples shows that the magnetic susceptibility is on average lower in the lower half of the section.

Curie balance

From section AZ15, three different lithologies were measured; results are shown in Figure 5 for all lithologies. Magnetization decreases gradually upon heating and shows reversible behavior up to a temperature of around 400°C. Above this temperature, magnetization significantly increases and the behavior is not reversible anymore. Up to a temperature of 500°C, the magnetization increases, after which it decreases up to a temperature of 580°C. For sample 15.26 (siltstone), a very slight decrease can be seen also at 680°C. The decrease in magnetization up to about 400°C is most likely caused by the breakdown of iron sulfides. The increase in magnetization from 400°C to 500°C is caused by oxidation of iron sulfides that are converted to magnetite. The iron sulfide is probably pyrite, as pyrite usually breaks down at 380°C to 420°C. The mineral that is formed is broken down again at 580°C, which is the Curie temperature of magnetite. Furthermore, the Curie balance of sample AZ15.26 shows another (small) decrease in magnetization at a temperature of 680°C, which corresponds to the Curie temperature of hematite, so this sample possibly contains some hematite as well.

Samples of AZ16 show quite different behavior. Overall, the signal is stronger than that of samples of AZ15, which is expected for basalts. The sharp increase in magnetization above around 400°C that is seen at samples of AZ15 is not observed in the basalts of AZ16. For 16A and 16B, the behavior is reversible up to a temperature of around 350°C, after which a slight increase can be seen. At a temperature of around 520°C, the magnetization remains constant. 16C does not show this increase around 350°C, but also the magnetization is constant at temperatures above 520°C. Some samples exhibit two inflexions in the result upon cooling (thick black line) that are not expressed to the same amount in the other samples. The increase around 350°C reflects exsolution of titanomagnetite, which leads to the creation of titanomaghemite (L. de Groot, personal communication). Sample 16C does not exhibit this kind of behavior. As this sample probably contains purer magnetite, instead of titanomagnetite, the breakdown of magnetization is closer to the Curie temperature of magnetite, which is around 580°C.

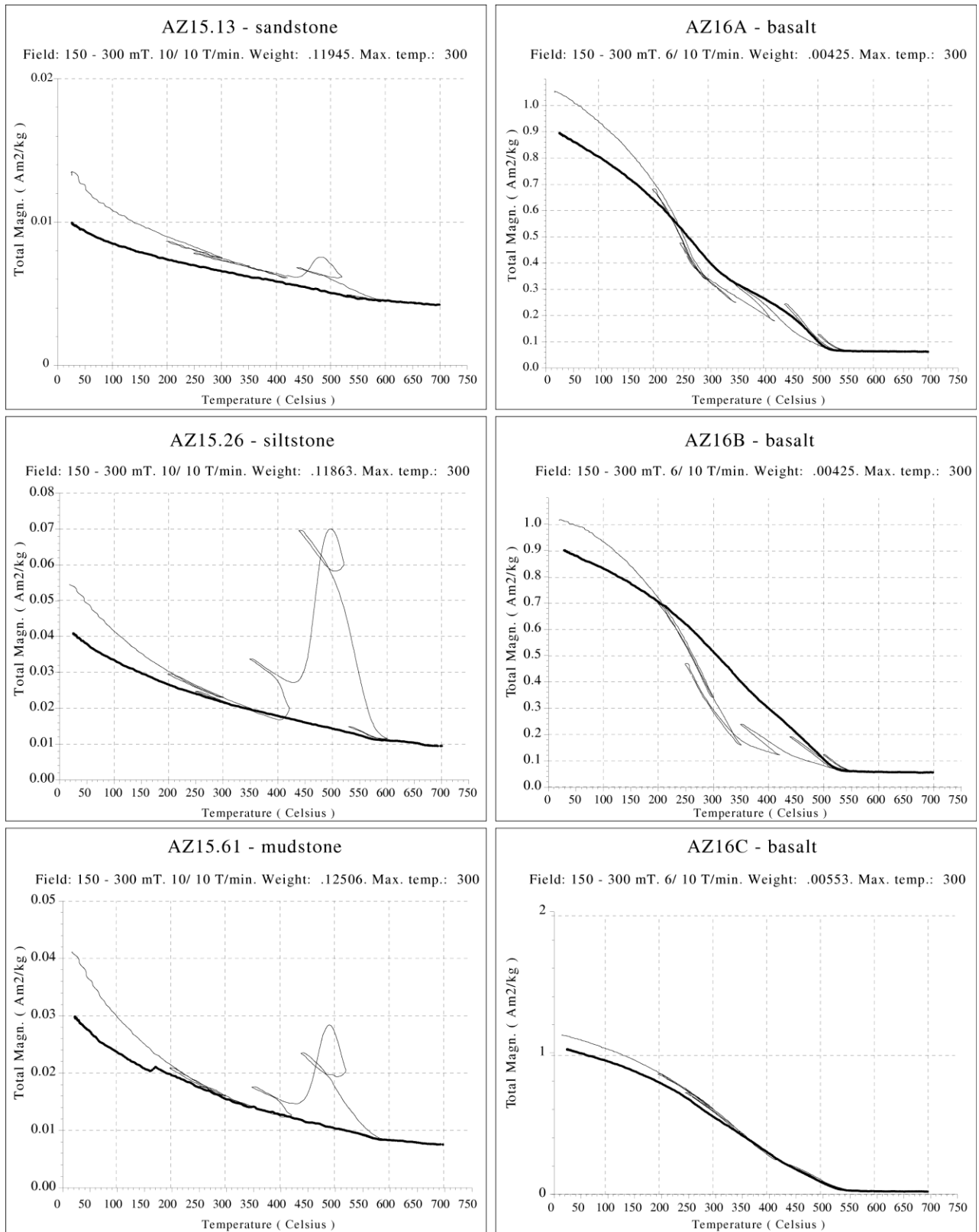


Figure 5: Curie balance results of three samples of AZ15 and three of AZ16. Thin black lines represent six heating and cooling cycles. Thick black line represents the cooling curve.

Kappabridge

All basalts (A-Z) from section AZ16 are measured on the Kappabridge. Results can be divided into two groups, examples of which are shown in Figure 6. The first group, of which 16A is a representative, has Curie temperatures of on average between 220°C and 270°C and are associated with sharp peaks in susceptibility. Curie temperatures of the second group, of which 16C is an example are in general higher, between 320°C and 520°C and show no peaks, but rather gentle inflexions. All samples show that susceptibility is reduced to zero at a temperature of around 580°C, which is the Curie temperature of magnetite. The three groups that are seen in the paleomagnetic results and the geochemistry (as mentioned later on in this thesis) are not recognized in the results of the Kappabridge. There is however a correspondence to the color of the thin sections (see next section on petrography). The difference in Curie temperature seems to depend on the speed of cooling, as generally, the sills have higher Curie temperatures than the flows. As from the thin sections, the difference between flows and sills is not always very clear; this relation is a general one and does not apply to four of the 26 samples. The magnetic signal in the basalts of AZ16 is most likely carried by titanomagnetite (Fe_2TiO_4), and the Curie temperature is linked to the relative amount of Ti in Fe_2TiO_4 (Dunlop and Özdemir, 1997). If there is more Ti in the titanomagnetite, the Curie temperature becomes lower. If the magnetite is purer and has less Ti, the Curie temperature is higher. It is very likely that the amount of Ti in titanomagnetite is dependent on the duration of crystallization, and thus on cooling time. If the cooling time is longer, crystallization will proceed more optimal, resulting in 'cleaner' magnetite with less titanium.

Petrography

A thin section of one sample of each flow was made. As can be seen from the appendix, and Figure 6, the thin sections are very different in color. Examination of thin sections using a polarizing microscope shows that the difference in color reflects a difference in grain size of the groundmass. The darker thin sections have a more fine-grained groundmass with small phenocrysts, while the lighter thin sections all have a very coarse groundmass, with many large phenocrysts. At macroscopic scale, there is no clear difference between the three groups.

All thin sections contain relatively large plagioclase phenocrysts within a finer grained groundmass and are thus porphyritic basalts. Grain size of the groundmass depends on the speed of cooling. Some samples have a groundmass that is completely crystallized. These are interpreted to have experienced slow cooling, which would be possible if they are intrusive. These samples are thus assumed to be sills. In Table 6 that contains XRF data, it is listed which samples are considered flows and which are considered sills. This interpretation is fairly in line with the Kappabridge results and Curie balance results that have been shown in the previous sections. It is possible that pillow lavas are present, but no radially distributed cooling cracks, concentric layers of vesicles parallel to the outer surface and rounded and tubular morphological shapes with striated outer glassy surfaces (that are all typical for pillow lavas) were observed (S. Branca, personal communication).

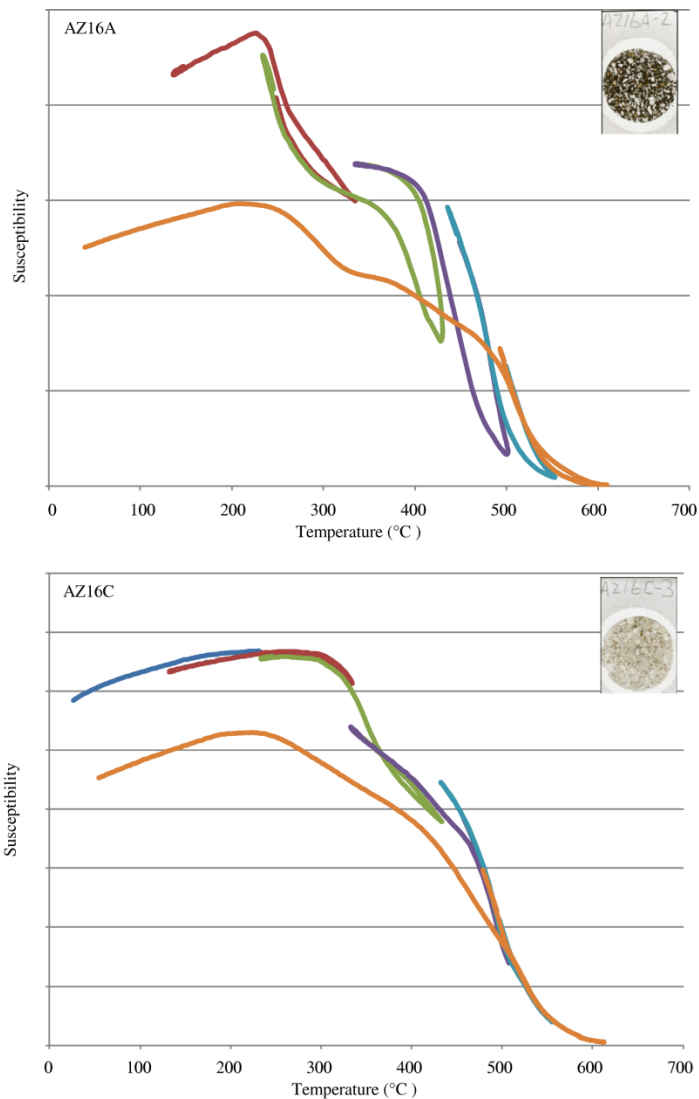


Figure 6: Kappabridge plots for AZ16A (flow) and AZ16C (sill) with thin sections in PPL. Different colors of lines represent different heating and cooling cycles.

Biostratigraphy

In section AZ14 and in the lower part of section AZ15, large benthic foraminifera were found (Nummulites). These were analyzed by W. Renema (Naturalis Leiden) and interpreted to be of (Middle) Priabonian age.

Of section AZ15, samples MP0-MP10 were analyzed for biostratigraphy. Even though all MP samples were barren of dinoflagellates, nannoplankton was present. Several species of nannoplankton were found, as shown in Table 4 and Figure 7. Of the ten samples (MP1-MP10) that were sent out for nannoplankton analysis, five samples were barren. Sample MP1 contained an assemblage characteristic for Mediterranean nannoplankton zone (MNP) 18A (according to Fornaciari et al., 2010). Samples MP2 and MP3 comprised an assemblage that placed them in MNP18B. Samples MP4, MP5 and MP6 were barren. Samples MP7, MP8 and MP9 belong to MNP19. Sample MP10 was also barren.

Sample	<i>C. floridanus</i>	<i>C. pelagicus</i>	<i>C. erbae</i>	<i>C. reticulatum</i>	<i>D. bisectus</i>	<i>D. scrippsae</i>	<i>D. saipanensis</i>	<i>E. formosa</i>	<i>I. recurvus</i>	<i>L. cf. arcanus</i>	<i>L. minutus</i>	<i>R. daviesii</i>	<i>R. samodurovii</i>	<i>Reticulofenestra</i> sp. (3-5 µm)	<i>R. umbilicus</i>	<i>S. cf. radians</i>	<i>Tr. pulcher</i>	<i>Z. bijugatus</i>	Okada and Bukry, 1980	Fornaciari et al., 2010
AZ MP 10																			?	?
AZ MP 9	x	x		x	x	x		x	x				x							
AZ MP 8																			CP 15b	MNP 19
AZ MP 7		x		x		x		x	x			x	x	x						
AZ MP 6																				
AZ MP 5																			?	?
AZ MP 4																				
AZ MP 3				x	x						x								CP 15a	MNP 18B
AZ MP 2				x	x			x			x				x		x			
AZ MP 1	x		x	x	x		x									x	x			MNP 18A

Barren

Table 4: results of nanoplankton analysis by G. Villa and a correlation of MNP zones to the GPTS of Cande and Kent (1995), according to Fornaciari et al. (2010).

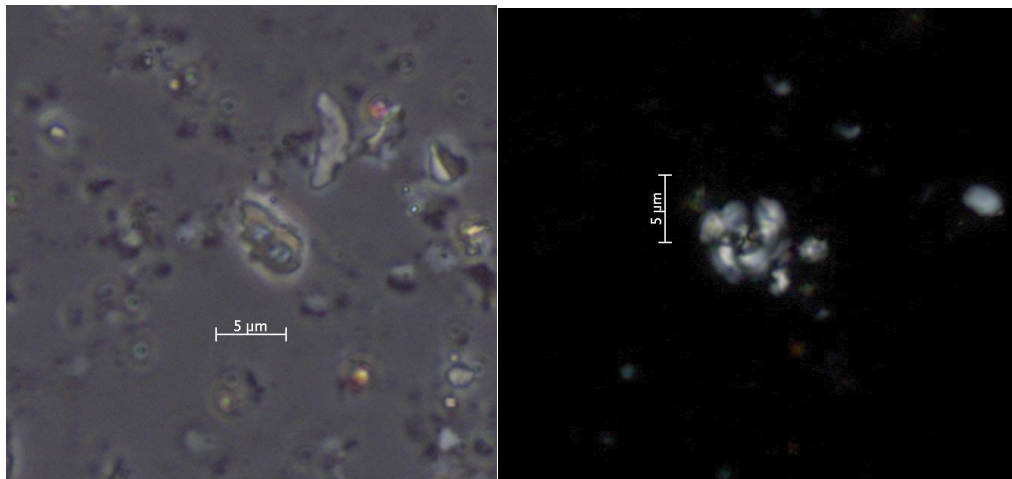


Figure 7: On the left picture *I. recurvus*, from sample MP9, on the right picture *C. reticulatum*, from sample MP7 (scale bar is 5 µm for both pictures)

ChRM/Magnetostratigraphy

AZ14 - Sediments

The sedimentary samples of section AZ14 show results that are ambiguous. Figure 8 shows representative Zijderveld diagrams, both tc and notc for samples 14.1 and 14.10. Sample 14.1 contains a low temperature normal component, clusters at higher temperatures and does not decrease towards

the origin. It is therefore not possible to determine the high temperature component. There could be a high temperature reversed component, as the demagnetization direction is not towards the origin. However, the reversed component is more likely to reflect a post-tilt reversed overprint, as the direction of the notc diagram represents a more reasonable reversed signal than the tc diagram. The normal component is probably of such an influence that the direction of the reversed component, when plotted, does not yield the ChRM for the timing of deposition. Sample 14.10 contains two components, goes through the origin but does not cluster. Sample 14.10 has a low temperature normal component, and a high temperature reversed component. The direction of this reversed component is probably partly overprinted by a normal component, in such a way that no good direction can be obtained anymore. Nonetheless, the tc diagram is more likely to reflect a reversed direction, compared to the notc diagram, so a post-tilt reversed overprint seems unlikely for this sample. A considerable part of the samples has a very weak signal, similar to sample 14.4, that is shown in Figure 8. No gradual decrease is observed in these samples and all measurements plot randomly around the origin. As no direction can be obtained from these samples, they are rejected for magnetostratigraphic analyses.

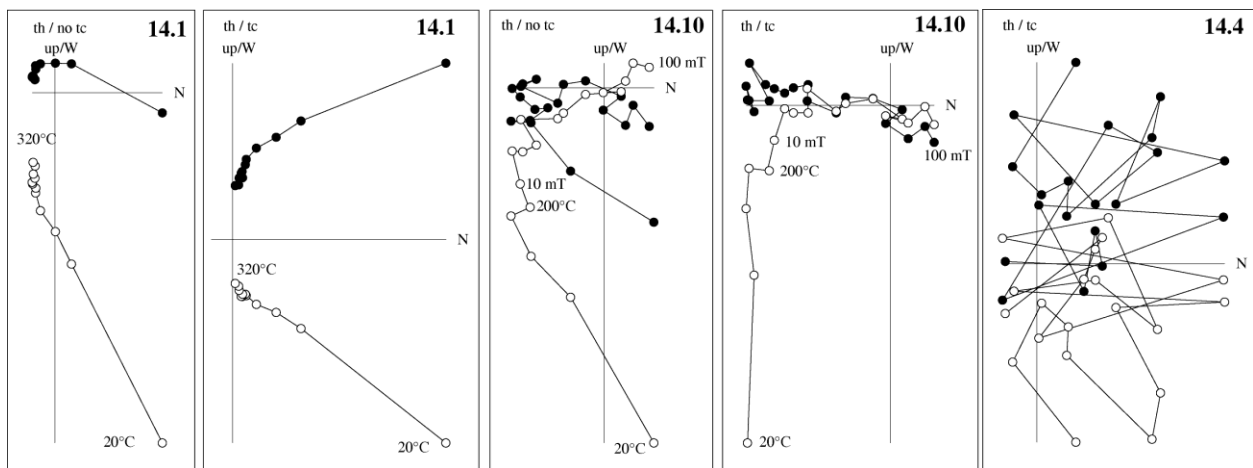


Figure 8: Zijderveld diagrams of samples of sediments of section AZ14.

AZ14 – Basalts

Representative Zijderveld diagrams for section AZ14 have been plotted in Figure 9, from flows 14A and 14D. Samples have many different types of behavior. Most samples have a low coercivity/low temperature normal component. High coercivity/high temperature components rarely decrease towards the origin, like AZ14A.7 and AZ14D.2. Other samples have only a normal component, such as sample AZ14D.3, while others have a positive inclination but a declination of around 180 degrees, like AZ14D.12. As behavior is very different, samples are also analyzed using great-circle analysis, as shown in Figure 10. Some samples are similar to the results of the basalts of AZ16, such as 14A.7 and 14A.11b, which have three components. Interpretation of the results is preferably done in the same way as AZ16, in which the medium coercivity component (roughly from 20-60 mT) is interpreted to reflect the ChRM at timing of deposition. Unfortunately, for AZ14, samples do not show such uniform behavior as for AZ16. Some samples have completely normal directions. All samples that are labeled with the same

letter are within the same unit, thus there are no sediments in between. It would be expected that these samples would all have the same directions, similar to samples of AZ16. This, however, is not the case we conclude that some samples have an unremoved component. This behavior is interpreted to reflect a partial (or sometimes complete) overprint. In case of a partial overprint, directions can be obtained using great-circle analysis. This analysis has been performed for basalt 14D, as shown in Figure 10. The result of the great-circle analysis is quite different from principal component analysis, as can be seen from Figure 13.

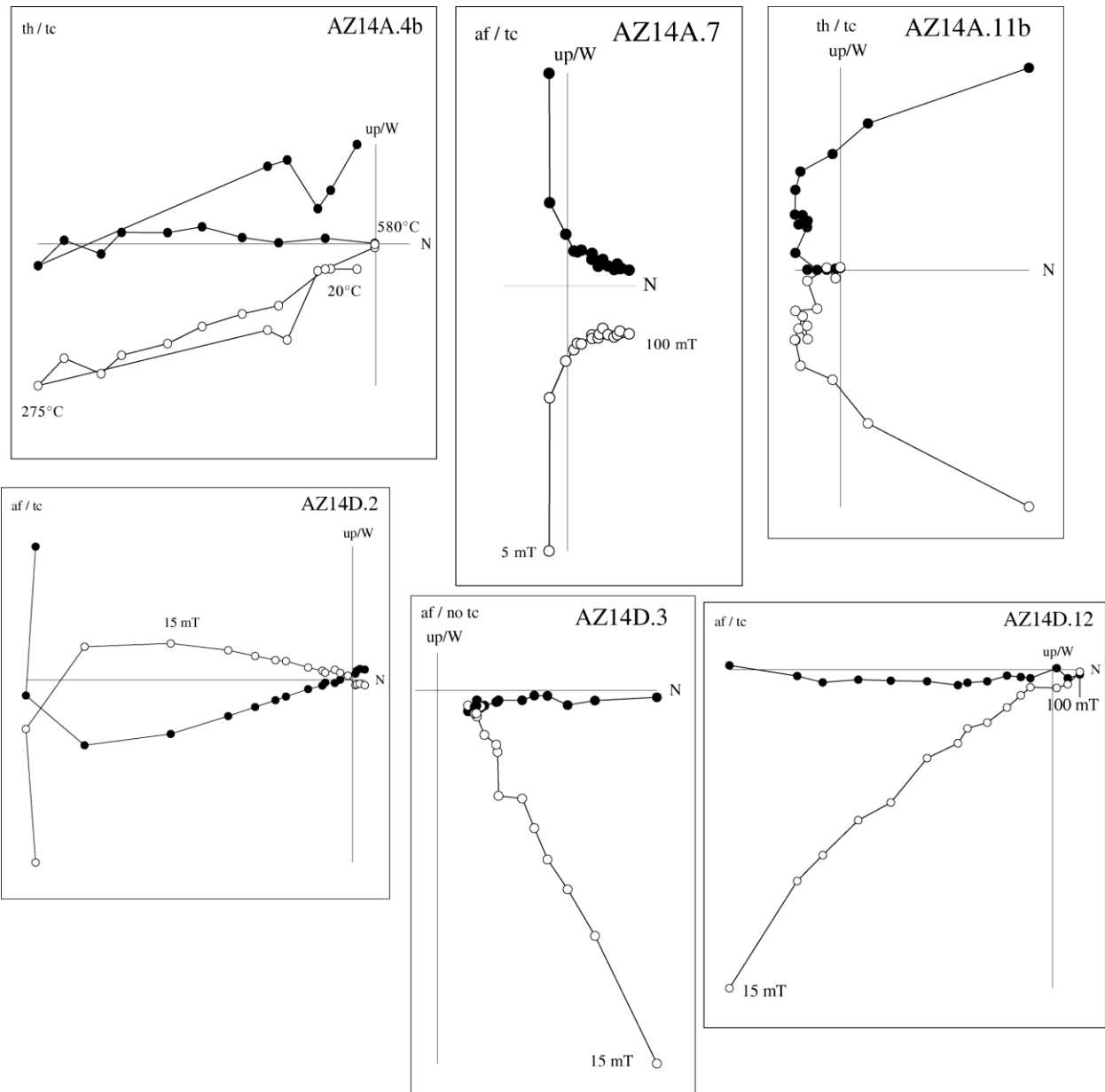


Figure 9: Representative Zijdeveld diagrams of basalts of section AZ14

ni	N	dec	inc	k	a95	am95	t95
8	10	160.3	-17.6	71.2	5.8	7.8	24.73

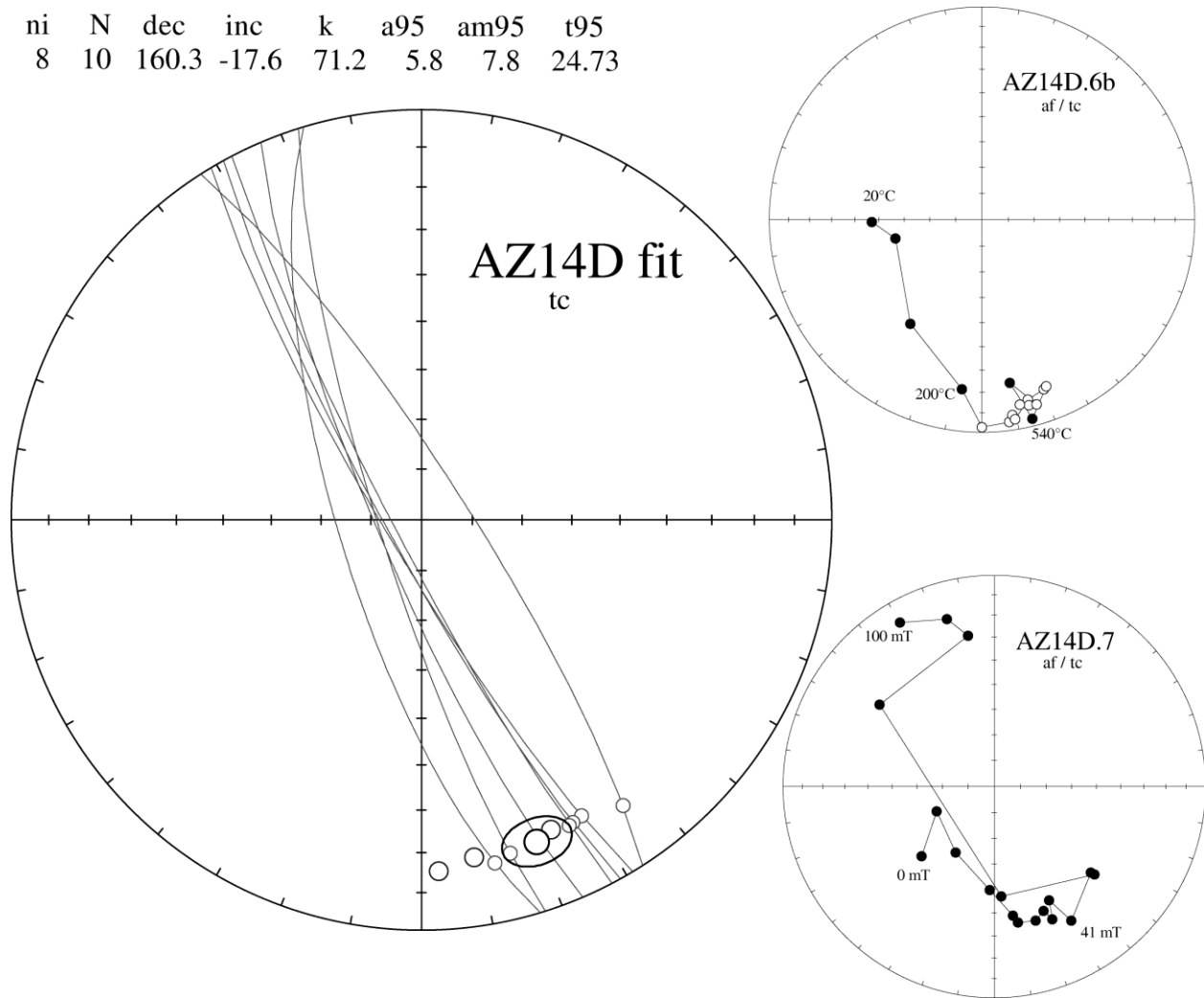


Figure 10: Great-circle fits and corresponding direction of AZ14D (left). Blue circles are setpoints (interpreted directions); red circles are great circle solutions. Small black circle is average direction of great circle fits, with a95 (larger black circle around average). Demagnetization diagrams of two samples are shown on the right.

AZ15

The different demagnetization methods are of little influence on the results of the sediments from section AZ15. In Figure 11, representative Zijdeveld diagrams (both tc and notc are shown when insightful) of samples of section AZ15 are presented. Sample 15.135 has demagnetization behavior that is very different from other samples. Decrease in demagnetization is very constant and slightly saw tooth-like. Sample 15.166 has a low temperature normal component, but is very weak and plots randomly around the origin after only a few temperature steps. Sample 15.113 has a low temperature normal component and a high temperature reversed component. The direction of the reversed component is steeper tc than notc. Sample 15.181 has a normal component for low and medium coercivity. At high coercivity, points plot more randomly. In notc the inclination is steeper than tc. Sample 15.49 has a low temperature steep normal component (notc) and a reversed component at high temperatures (tc). Sample 15.221 has a reversed low coercivity component and a normal high coercivity

component (tc) which has a negative inclination in notc. The last four steps, from 70-100 mT plot randomly.

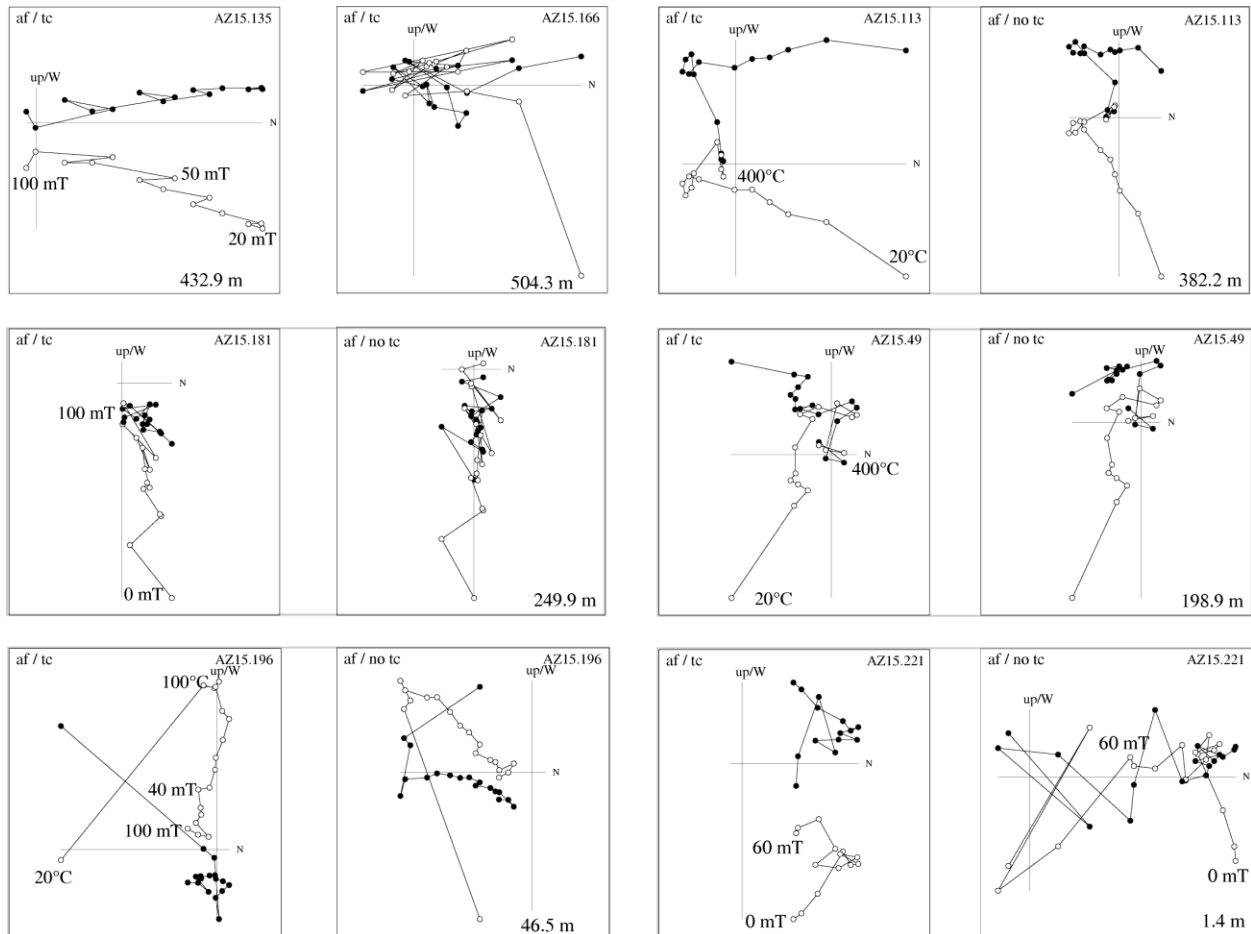


Figure 11: Representative Zijdeveld diagrams of section AZ15 with stratigraphic level of the samples. TC and NOTC results are shown when insightful.

In section AZ15, like in section AZ14, many types of demagnetization behavior occur. Many samples show directions that probably do not represent the direction of the magnetic field at time of deposition, which is most likely caused by either early (sometimes reversed) or present-day field overprints. To separate reliable and unreliable directions, results are categorized based on their reliability.

Results have been categorized in 5 categories: 1. Reversed: these samples most likely show a primary reversed signal. 2. Reversed?: these samples possibly show a primary reversed signal. 3. Unknown: these samples are either very weak, or have such an overprint that the primary direction is unrecognizable. 4. Normal?: these samples possibly show the primary normal signal. 5. Normal: these samples most likely show a primary normal signal.

For samples that show directions for tc that are very plausible, combined with highly unlikely directions for notc, the NRM most likely represents the ChRM at time of deposition. These samples are assigned to the categories Reversed and Normal (based on the direction).

Samples that have t_c and $notc$ results that do not differ very much and seem to go to the origin (for normal directions) or towards reversed (for reversed directions) and do not seem to represent an overprint, are categorized as Normal? and Reversed?

If the direction for the $notc$ diagram is better than that of the t_c diagram, this could be an indication for a post-tilt overprint. Some samples seem to have a post-tilt reversed overprint (see Figure 11) such as 15.196, which has a plausible reversed direction high temperature component in $notc$. However, the t_c direction is very unlikely. If there is suspicion that the high coercivity/high temperature component is caused by an overprint (if $notc$ directions are more plausible than t_c directions), the result has been categorized as Unknown. Also samples that have a very weak signal and plot randomly, like 15.166, as well as samples that have an abnormal demagnetization pattern, like 15.135, are assigned to this category.

AZ16

All samples were demagnetized using AF demagnetization up to 100 mT. Also, of each flow, two samples were selected for additional thermal demagnetization. Results of the AF and thermal demagnetization are intrinsically the same. Almost all flows have multiple components, as can be seen from Figure 12. The low coercivity component, if present, is generally removed at 20 mT (or 275°C). Many samples contain a highest coercivity component that is observed above 60 mT (or temperatures above 500°C). The low coercivity component most likely does not represent the magnetic field at the time of emplacement of the basalt, but reflects a viscous overprint. Also the highest coercivity component does not seem to represent the magnetic field at the time of deposition, but might be some kind of weathering-related overprint, or even a gyroremanent magnetization (GRM). All samples are therefore interpreted using (roughly) the medium coercivity (temperature) component that is removed from 20-60 mT (or 300-500°C). This component is then plotted for all samples in an equal area plot, and an average declination and inclination are calculated. As AF demagnetized results have slightly better quality, these are used for calculating averages. Data are shown in Figure 12, Figure 13, Figure 15 and Table 5 (appendix).

When all samples are plotted in an equal area plot, there are three groups are distinct. These groups can be distinguished in the sampling sequence as well. The lower group contains units A-K. The middle group contains units L-P as well as unit T. The upper group contains unit Q-S, and V-Z. However, unit U is different, as it belongs to the middle group (L-P, T) in terms of declination and inclination, but seems to be in the upper group, looking at the log. However, in this interval, there is very little stratigraphic distance between the flows, see Figure 14 and Figure 15. Therefore a slight inaccuracy in strike and dip, GPS location or lateral variation in thickness of flows or sills (this last option is considered most likely) can lead to a relative stratigraphic position of U in the upper group, instead of the middle group. As this is probably the case, unit U is accounted to the middle group. Remarkable is that samples have a steeper inclination before tilt correction (see Table 5), which might be caused by non-horizontal deposition.

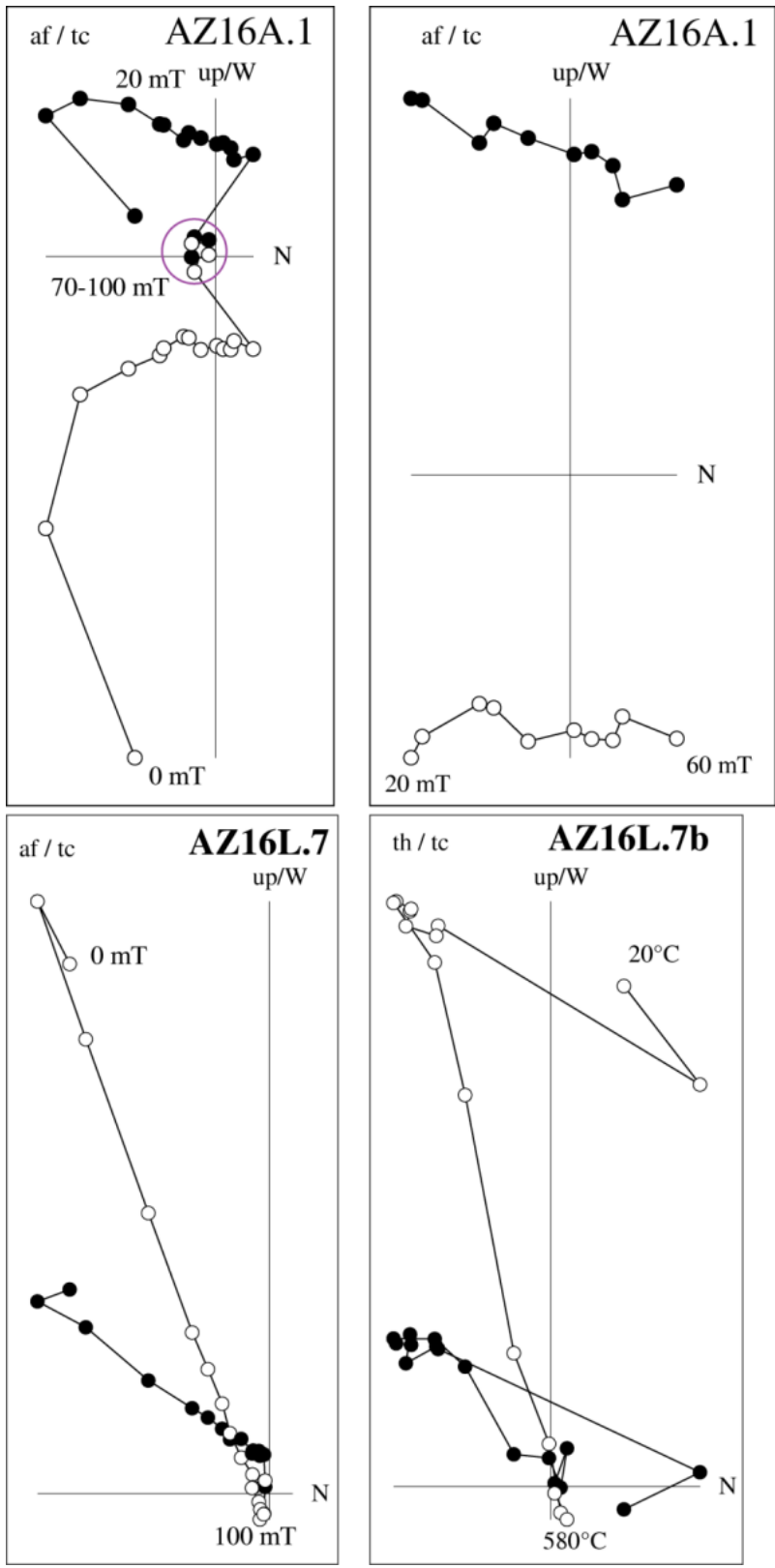


Figure 12: Upper half: Zijderveld diagram of AZ16A.1, left side are results of all steps, right side are steps that are used for interpretation of ChRM. Purple circle contains interval from 60-100 mT. Lower half: Zijderveld diagrams of sample 16L.7 (AF demagnetization) and 16L.7b (thermal demagnetization)

Site	N	dec	inc	k	a95	rsum
AZ16(A-K)	11	209.6	-7.7	31.8	8.2	10.685
AZ16(L-P)	7	220.2	-57.6	91.0	6.4	6.934
AZ16(Q-Z)	8	139.7	-10.3	55.9	7.5	7.875
AZ14	5	186.6	8.6	5.8	34.8	4.310

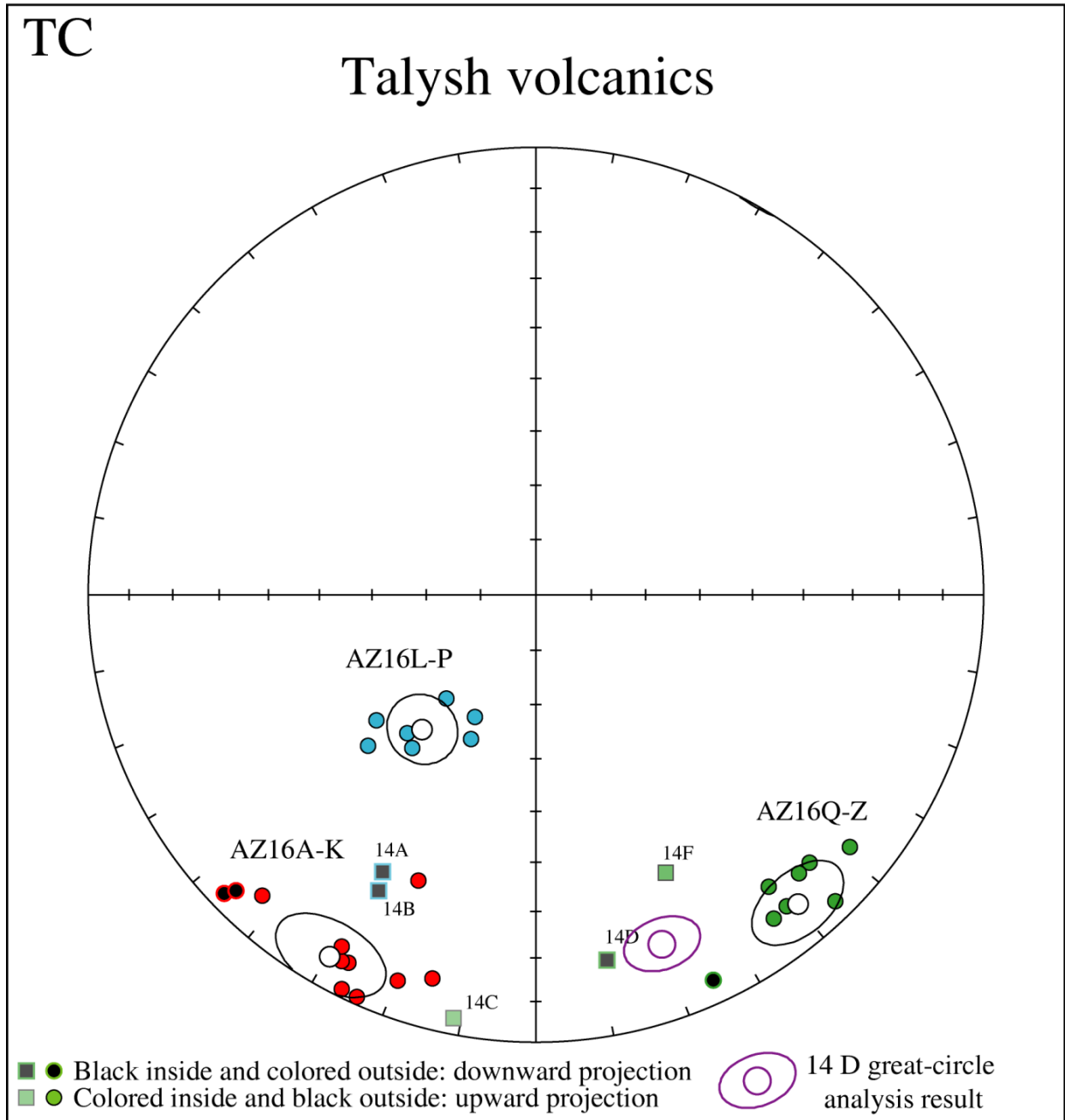


Figure 13: Equal area plot of averages per flow of AZ16 after 45 degree cutoff. Averages of AZ14 flows have been plotted without a95, except for 14D great-circle analysis which is the average direction after great-circle analysis with a95 plotted. For explanation of colors, see Figure 14.

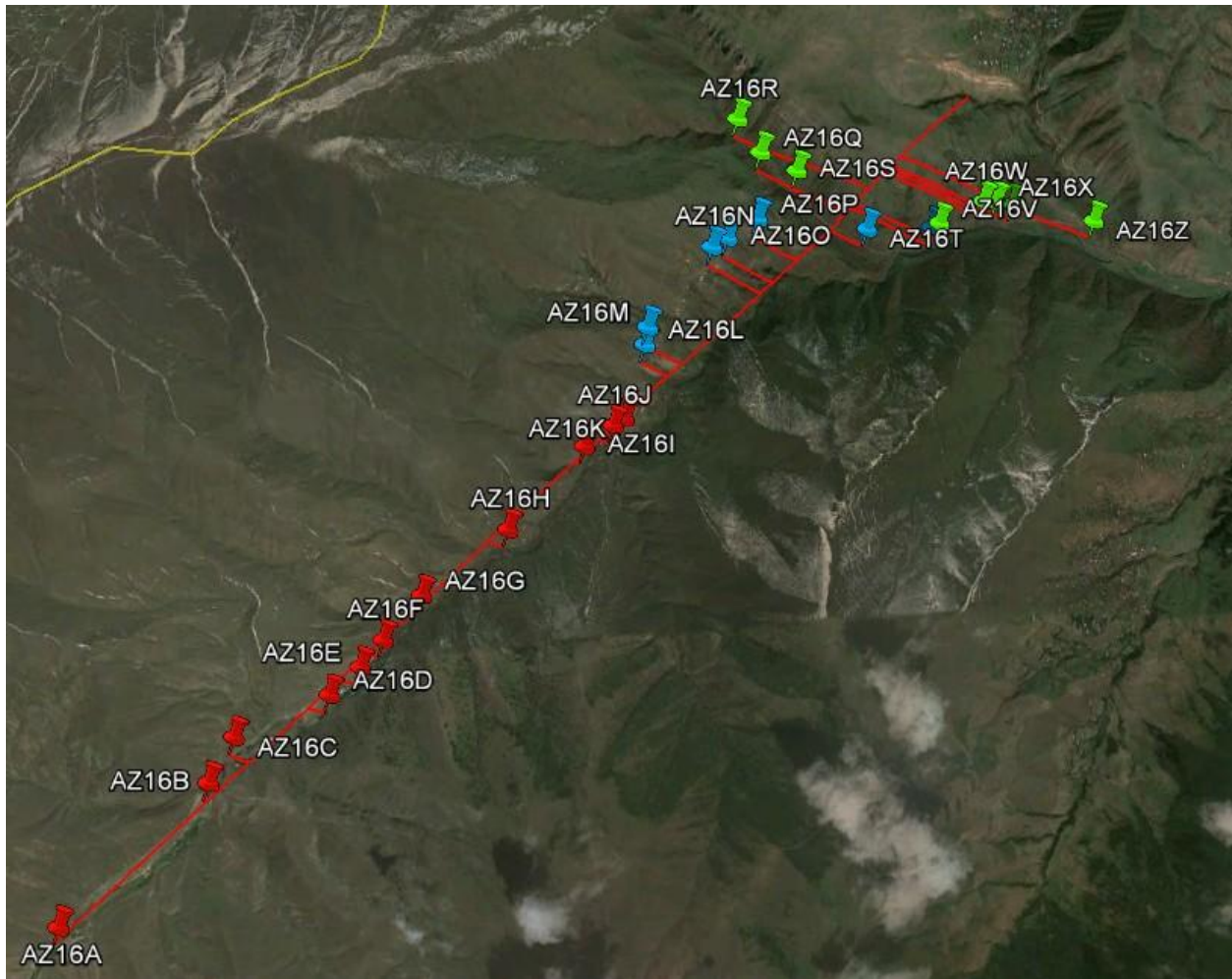


Figure 14: Locations of samples and strikes along which they are transferred to the profile line. Colors represent different groups. Red = lowest group, containing AZ16A-K, blue = middle group, containing AZ16L-P,T and U, green = upper group, containing AZ16Q,R,S,V-Z.

AZ16

ChRM

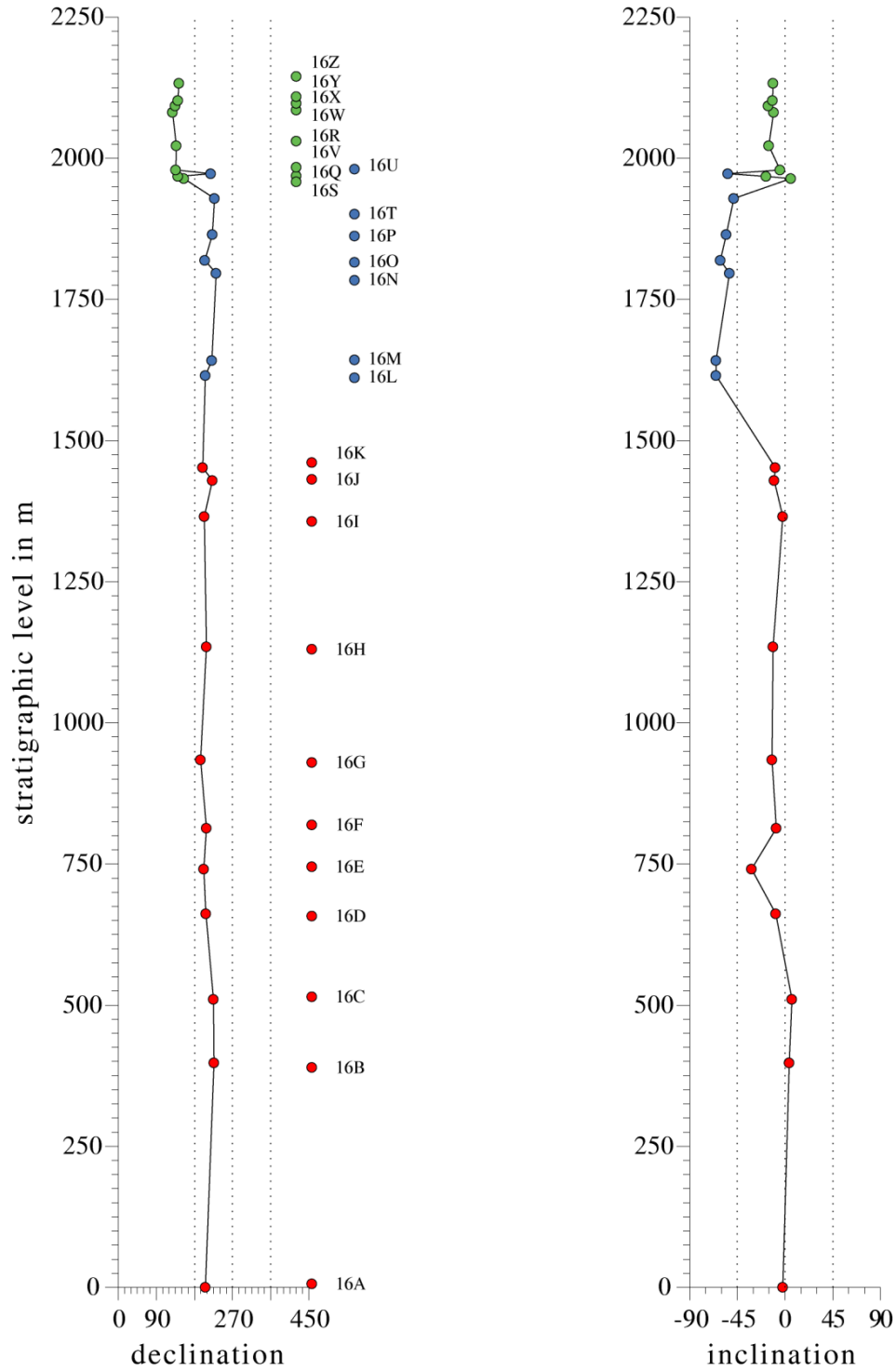


Figure 15: Declination and inclination of averages of sites from AZ16, after 45 degree cutoff. Colors are similar to previous figure.

Geochemistry

Although some problems occurred during creation of beads, when evaluating the results, no significant differences can be seen between the beads that were correctly made and the other beads. It is therefore concluded that the influence of all machine problems is negligible and all results can be accepted. Loss on ignition (LOI) was generally low (between 0.65 – 1.99 wt%), indicating that samples were fresh. Four samples showed LOI values of 2.90, 2.33, 2.04 and 2.06. However, these values are still within the range of samples that are considered suitable for geochemical analyses (e.g. Handley et al., 2007).

XRF results show that all samples are very similar in chemical composition of all elements. According to the IUGS classification of alkalis, samples are trachybasalts and basaltic trachyandesites (see Figure 16). Samples have no normative quartz, low Fe-enrichment, a high alkali content ($\text{Na}_2\text{O}+\text{K}_2\text{O} >5\%$), high $\text{K}_2/\text{Na}_2\text{O}$, are enriched in P, Rb, Sr, Ba, Pb and light rare earth elements (LREE). Furthermore, samples show a low TiO_2 (<1.3%) content and have a high, variable Al_2O_3 (14-19%). Thus, samples show shoshonitic compositions (Morrison, 1980), see Figure 17. All samples have a high magnesium number (M'), between 69 and 79. The M' of primary mantle magmas is 70. From Figure 18, it can be concluded that all samples are near or within the range of primary mantle magmas. Samples do not show a trend in major element composition, as trends (plotted either versus SiO_2 or stratigraphic level) of all major elements are generally flat.

The N-MORB normalized spider diagram (see Figure 20) shows that, compared to average N-MORB (Sun and McDonough, 1989), samples all exhibit an Nb trough, a Th spike, an enrichment in the large ion lithophile elements (Rb, Ba, K, Pb and Sr) and a relative depletion in heavy rare earth elements (Dy, Y, Er and Yb).

Samples from AZ14 and AZ16 plot within the same reach and are thus assumed to represent the same formation. This was also assumed by the study of Vincent et al. (2005). The three groups that were observed in AZ16 in terms of magnetic signal are also observed in the plots of many elements. However, they are most clear in plots of some metals (e.g. Th, U, Zr, Nb) when plotted versus SiO_2 content (see Figure 19 for the example of Th). From these plots it becomes clear that volcanics from AZ14A and AZ14B belong to the middle unit of section AZ16, which contains AZ16L-P, T and U. Furthermore, AZ14C, AZ14D and AZ14F belong to the upper unit of section AZ16, which contains AZ16Q, R, S and V-Z. This interpretation is also consistent with the great-circle analysis of AZ14D, as shown in Figure 13. Sample AZ16A is an outlier in many geochemical plots. This flow was sampled just above sands of the Neslin formation, and if it truly represents the beginning of the volcanic episode, it might have experienced some crustal or sediment contamination.

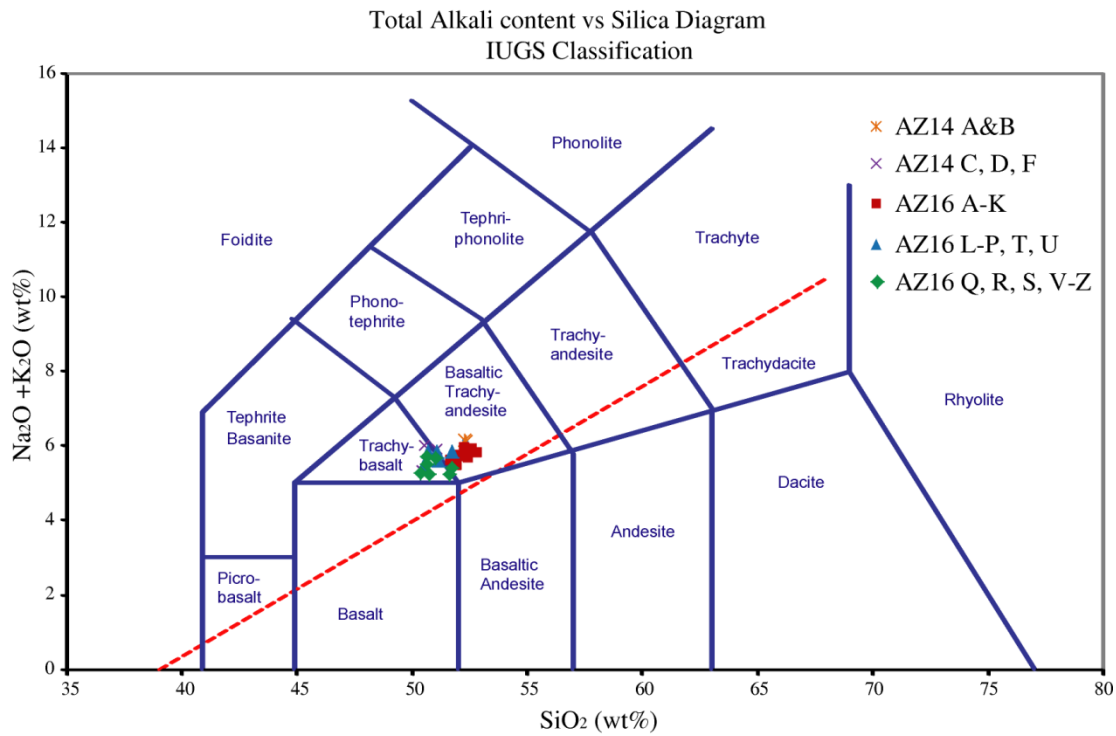


Figure 16: Total alkali amount versus SiO_2 content (IUGS Classification). Red line represents the boundary between subalkaline (below the red line) and alkaline compositions

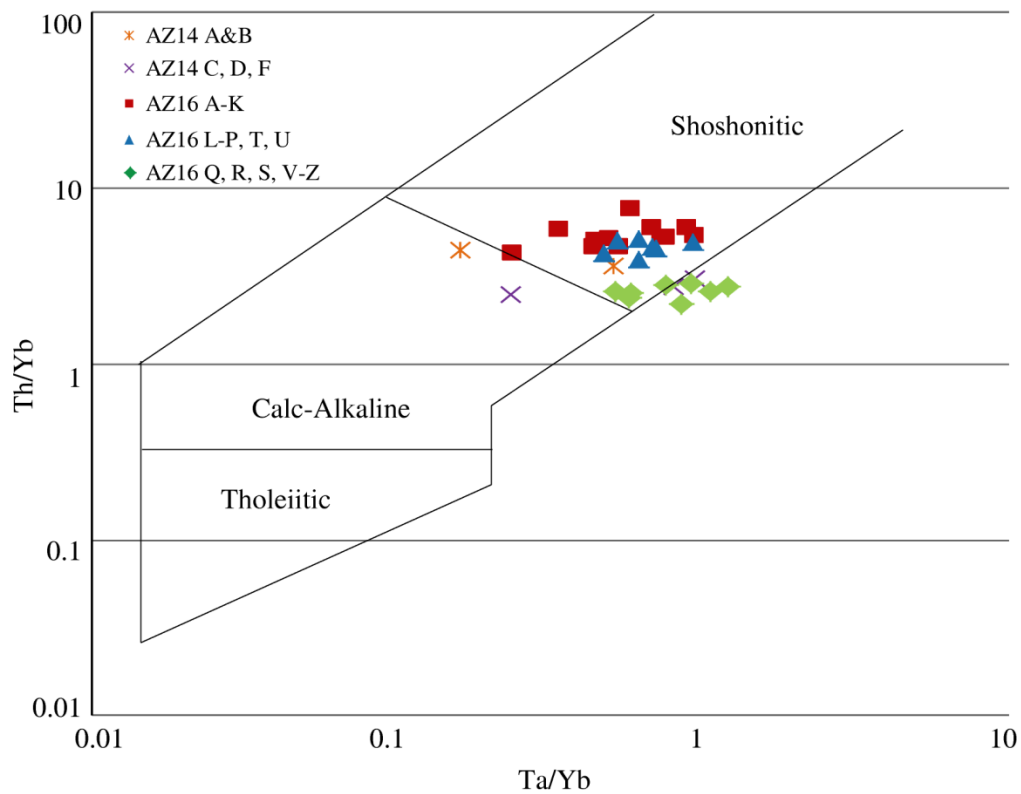


Figure 17: Th/Yb vs. Ta/Yb plot showing shoshonitic composition for most samples

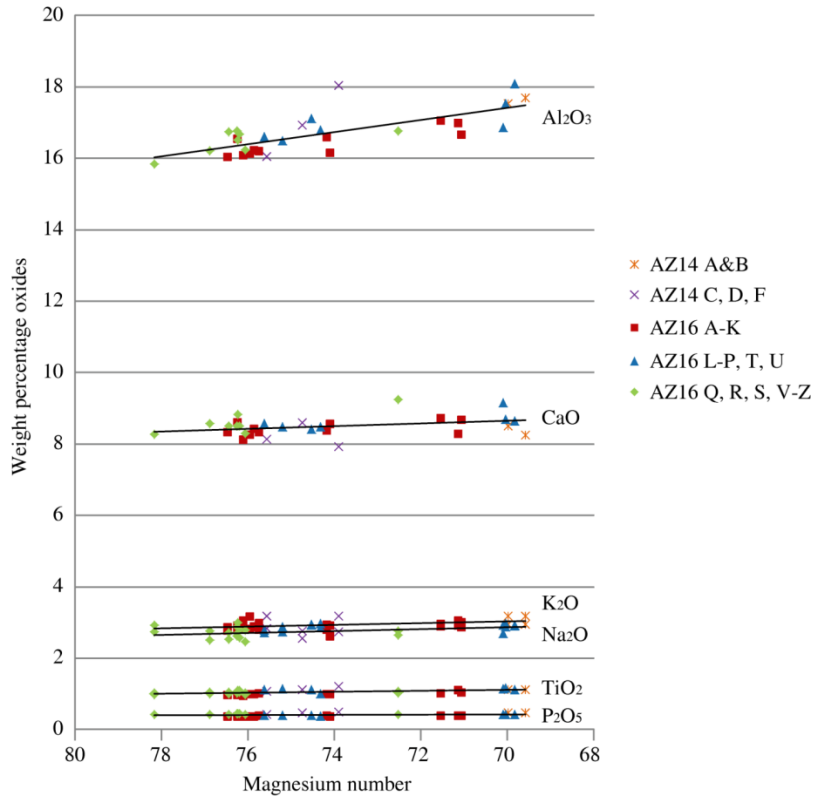


Figure 18: Weight percentages of oxides are plotted relative to the magnesium number ($100 \times \frac{\text{Mg}}{\text{Mg} + \text{Fe}}$)

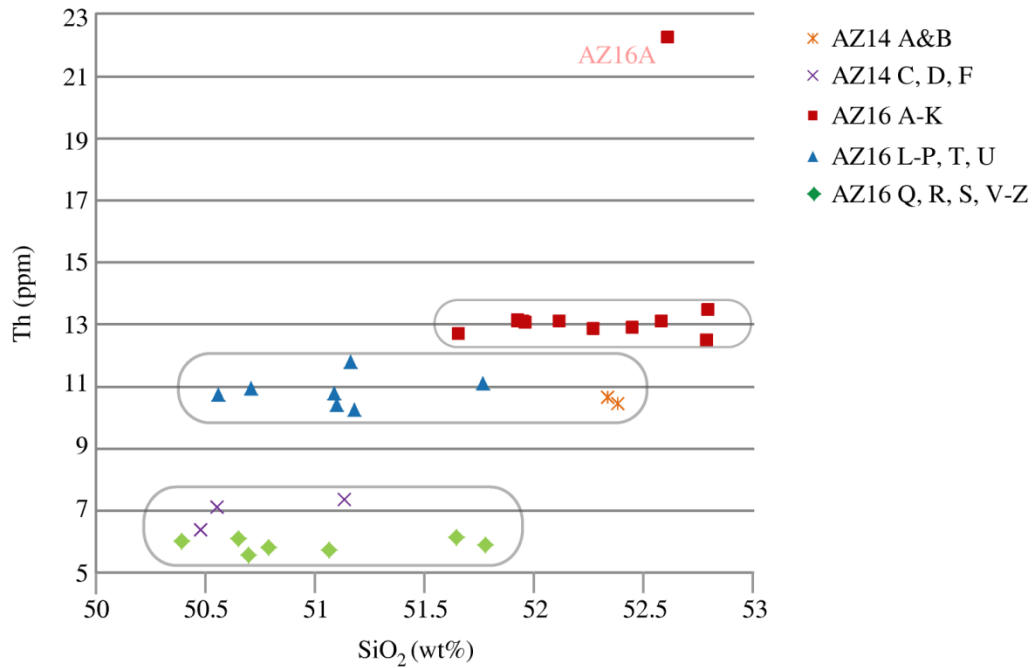


Figure 19: Abundance of Th plotted versus amount of SiO₂. Three groups are distinct, AZ16A is the only outlier.

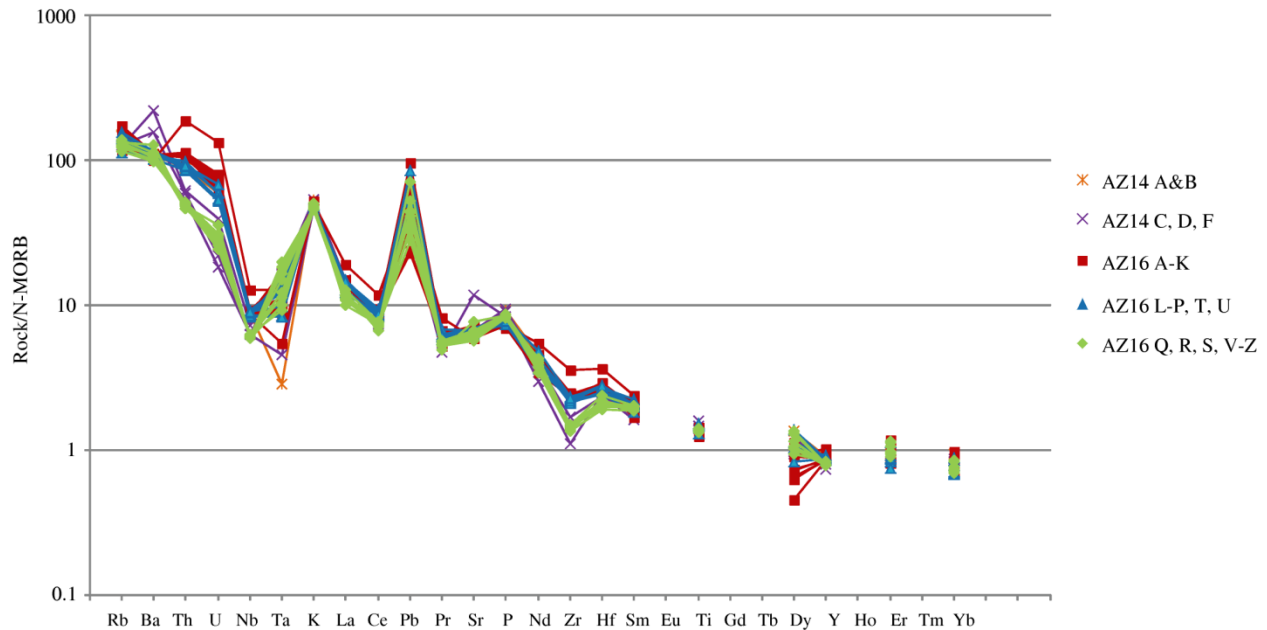


Figure 20: N-MORB normalized spider diagram. N-MORB normalization values from Sun and McDonough (1989) are used.

Discussion

Lithostratigraphy and structures

At 120 meters above the base of the section AZ15, there is a distinct change in sediments, from sands to silts. This change in lithology is interpreted to represent the boundary between the Arkevan formation and the Pirembel formation (Maikop series). This exact level is chosen as the two thick sand layers that are shown in Figure 4 mark the change from a sandstone-dominated to a siltstone/mudstone-dominated succession. The Maikop series in the Talysh consist of many silty layers, instead of the typical black shales that are found in Russia and the Kura basin (Popov et al., 2008; Hudson et al., 2008). Black shales in the classical sense (having mud grain size) are scarce, so the question remains whether the formation that is sampled here is chronostratigraphically equivalent to the Maikop that is described at the type-section in Russia.

The Talysh is generally considered to be a region that was in extension during the Eocene (Vincent et al., 2005; Verdel et al., 2011; Asiabanha and Foden, 2012, etc.). The extensional regime changed during the Late Eocene to Early Oligocene, to transtensional (Vincent et al., 2005) or compressional (Ismail-Zade et al., 1995). However, during this study, no evidence for Eocene extension or compression has been found. It is clear that deformation was ongoing at time of deposition, by the observations of slumps and olistostromes, but these could be explained by both modes of deformation. Russian studies that were performed during the 1960's and 1970's are often hard to obtain and not translated. The suggestion of extension in these works, combined with small number of studies in the area ever since, have led to the belief that extension was widespread. For example, according to Golonka (2004): "(Ali-Zade et al., 1996; Gasanov, 1992, 1996; Brunet et al., 2003). Vincent et al. (2002) link Talysh extension with major extension and ocean spreading within the adjacent South Caspian Basin." Even though the crust of the SCB is strongly thinned, (Motavalli-Anbaran et al., 2011) it is unlikely that any ocean spreading has taken

place after the Mesozoic, as the lithosphere of the South Caspian basin (SCB) is now relatively thick, cold and dense. Figure 21 shows a tomographic cross section through west Iran, the Talysh, and the SCB. Colors represent differences in the velocities with which seismic waves travel through the earth. The velocity of a wave is higher if material is denser. For the earth, colder material is generally denser and thus associated with higher velocities. The tomographic image thus shows parts that are relatively warm, associated with lower velocities (in red) and parts that are relatively cold, associated with higher velocities. From Figure 21, it can thus be concluded that the Talysh and SCB have a cold and thick lithosphere, which is in contrast with ocean spreading during the Late Eocene. The pink arrow indicates a colder zone which might represent the remnant of the subducted Neotethys slab. This slab cannot be traced very deep into the mantle, but there is another cold zone (represented by the purple arrow) which might indicate a detached slab, as suggested by Agard et al. (2011). Furthermore, if ocean spreading had taken place during the Late Eocene, geologic evidence (i.e. remnants of oceanic crust) would be expected to support this hypothesis. Altogether, the region might have been in extension during the Late Eocene, but the formation of new oceanic crust seems implausible and is not supported by tomographic evidence.

Magnetostratigraphy

Altogether, paleomagnetic results from both the sediments as well as the basalts of section AZ14 are too ambiguous to construct a reliable magnetostratigraphy. The quality of most samples of section AZ15 was relatively poor, so the directional data would yield little information. Instead, the interpretation and quality of the samples is shown in Figure 22, together with examples that are characteristic for the groups. This has resulted in a (low resolution) magnetostratigraphy, which is combined with the results of the nannoplankton analysis. The nannoplankton zones of Fornaciari et al. (2010) are correlated to the polarity time scale of Cande and Kent (1995). Ages have changed slightly for the different reversals in the interval of zones MNP18 and 19, compared to the GPTS of Gradstein et al. (2012). However, this does not make much difference for the correlation, as is shown in Figure 23. The lowest reversed interval is most likely C17n.1r, which yields an age for the reversal to C17n.1r of about 37.9 Ma. The highest reversed interval is most likely C16n.1r, which leads to an age for the reversal to C16n.1r of 36.1 Ma. Within this interval, there is roughly 330 meters of stratigraphy, corresponding to an average sedimentation rate of about 18 cm/kyr. However, almost 100 meters of this interval is part of the Arkevan formation, which contains many sand layers. Accumulation rates of the sands might be higher than those of the silts of the Pirembel formation; hence the sedimentation rate for the Pirembel formation is more likely to be lower than 18 cm/kyr. Taking the sedimentation rate of 18 cm/kyr, the age at the top of the sampled section can be calculated.

The top part (thus from 350 to 530 m) is 180 m of stratigraphy, thus equivalent to 1 Myr. This places the top of the section around 35.1 Ma. Underneath the reversal to C17n.1r, there is about 20 meters of stratigraphy, leading to an age of around 38 Ma for the base of the section. Consequently, the whole section is estimated to cover the time span from 38-35.1 Ma. The transition from the Arkevan formation to the Pirembel formation at 120 meters is then dated at roughly 37.3 Ma. Using a higher sedimentation rate for the Arkevan formation would lead to a younger Arkevan-Pirembel boundary.

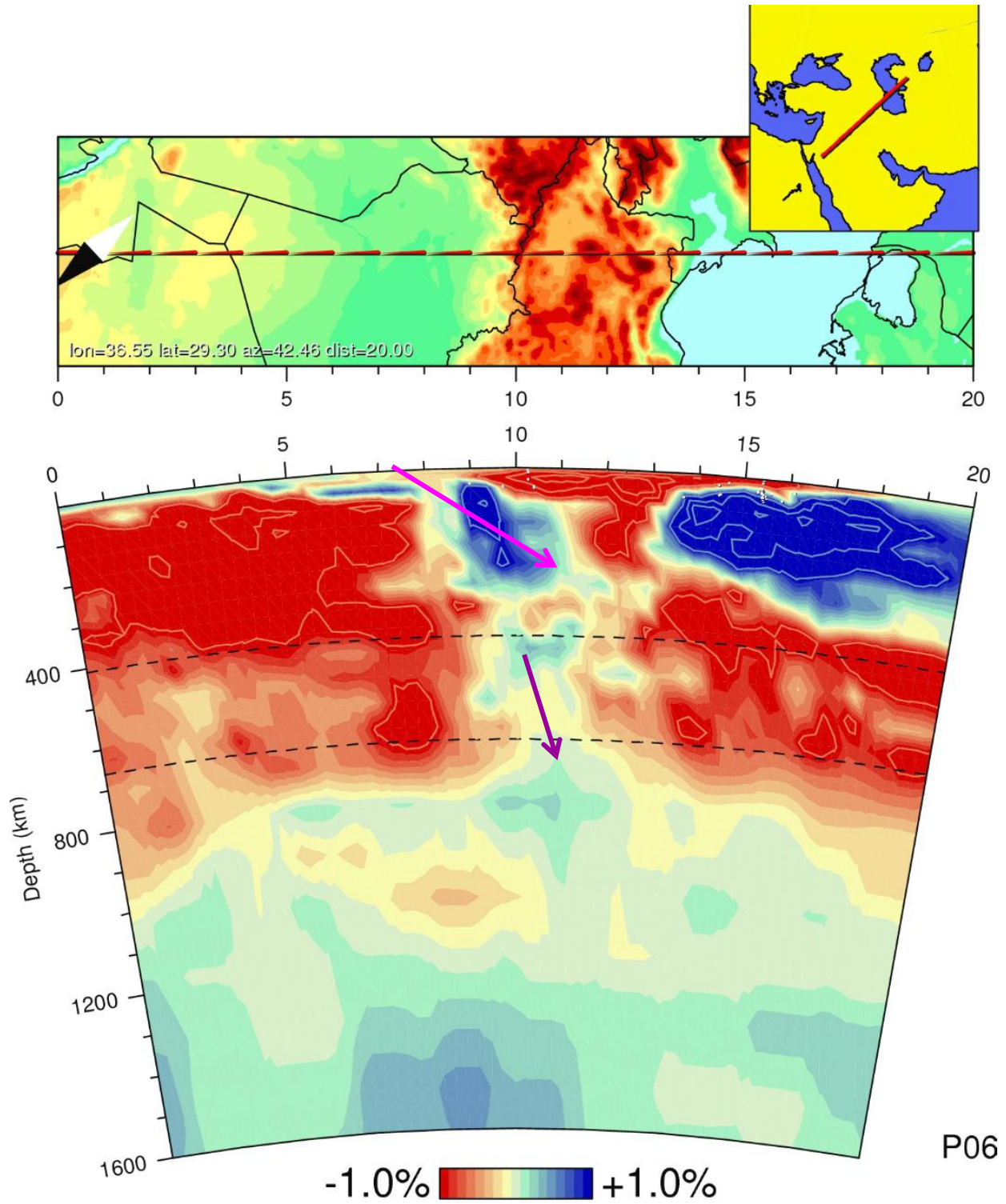


Figure 21: Seismic tomography (from: W. Spakman) through the Talysh and South Caspian basin. Colors represent differences in seismic velocities. Blue parts have higher seismic velocities, and are thus associated with relatively cold material. Red parts have lower seismic velocities, and are associated with relatively warm material. Pink arrow indicates possible subducted Neotethys slab. Purple arrow indicates possible detached part of Neotethys slab.

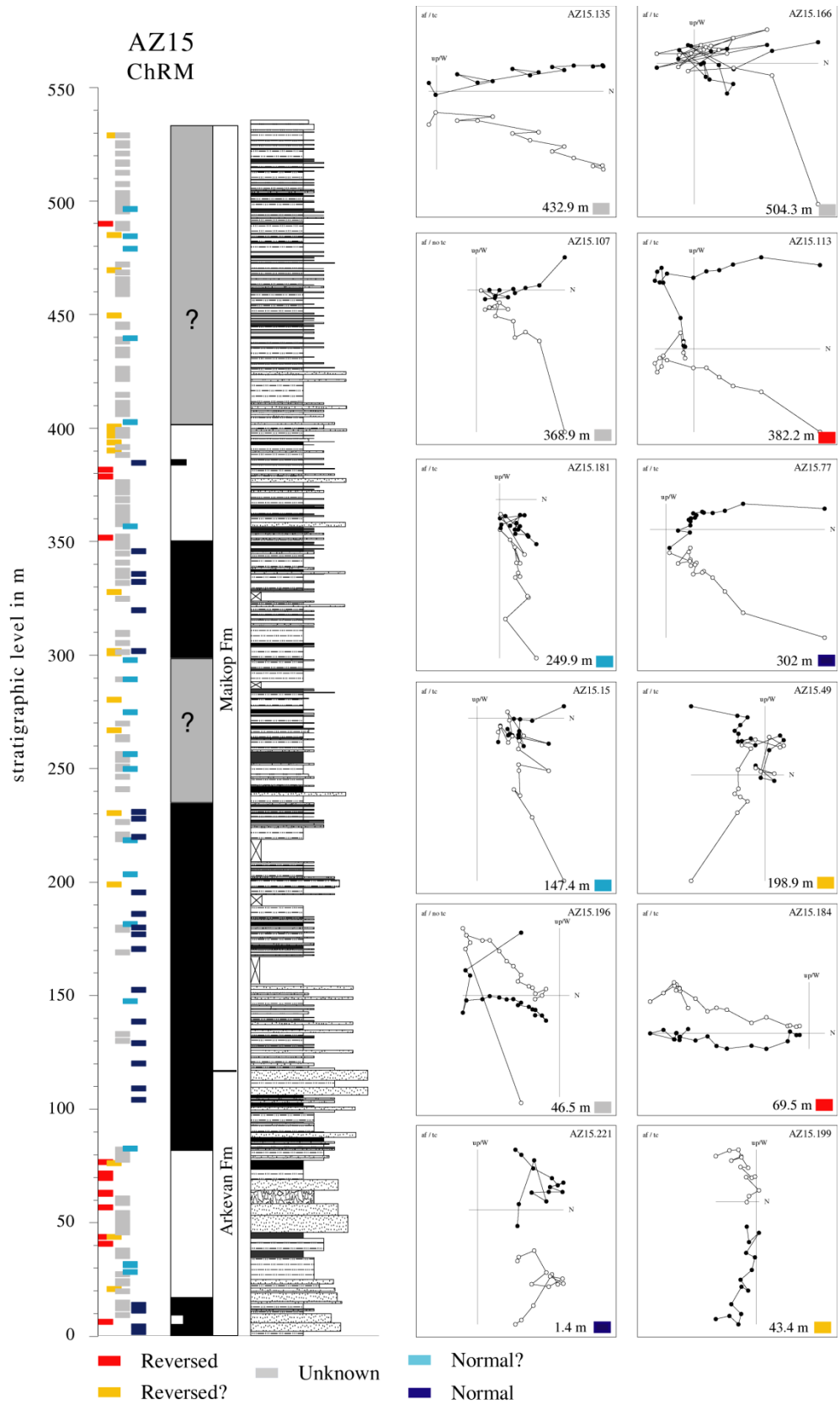


Figure 22: Interpretation of paleomagnetic results with examples of each group and stratigraphic log

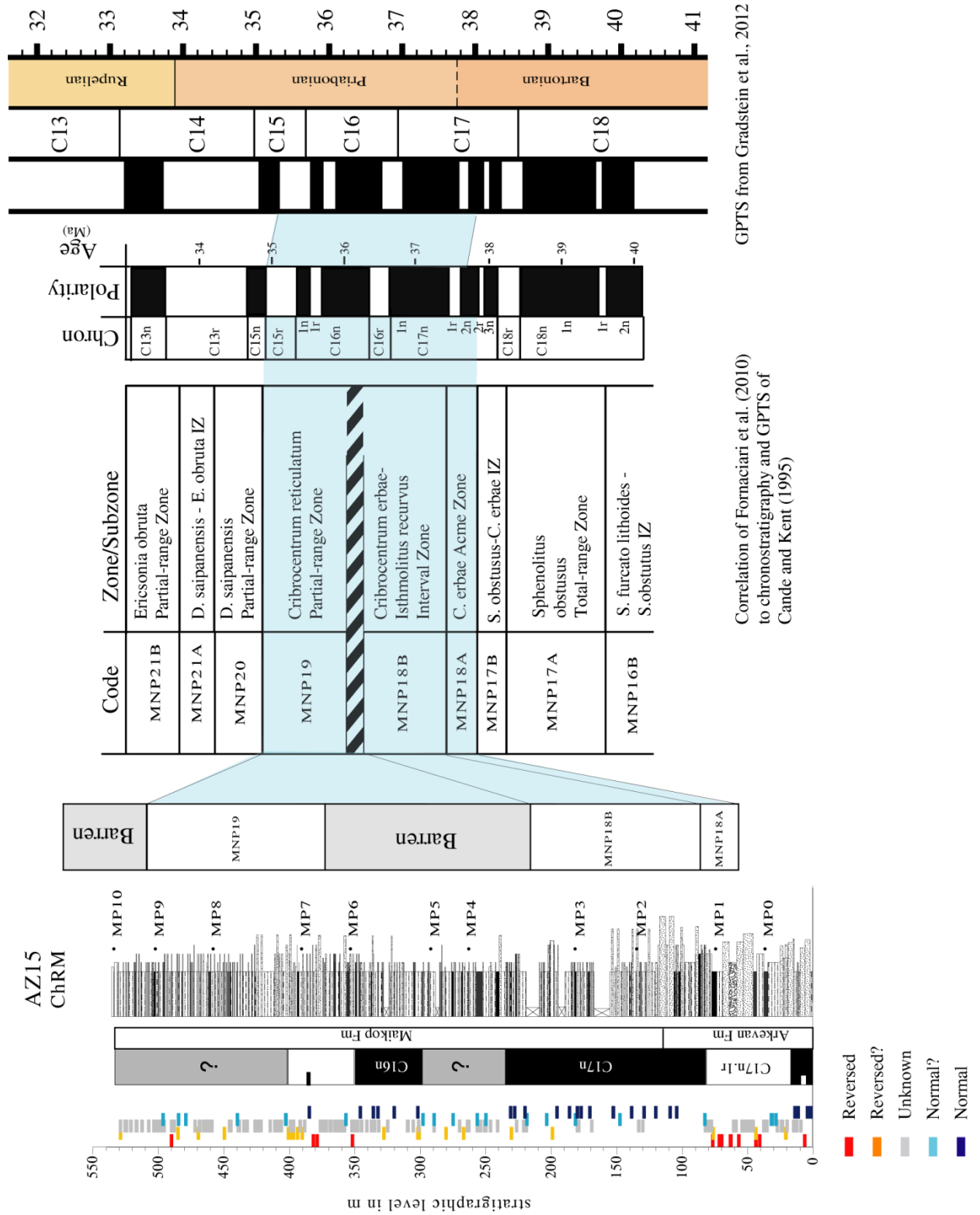


Figure 23: Correlation of the magnetostratigraphy of section AZ15 to the GPTS of Gradstein et al. (2012)

It can thus be concluded that, if the Arkevan formation – Pirembel formation boundary indeed represents the onset of Maikop sedimentation in the Talysh, deposition of the Maikop series does not start at the EOT (which takes place around 33.9 Ma). Maikopian deposition already starts 3.4 Myr earlier, around 37.3 Ma. It is very likely that the onset of anoxia is related to tectonics, since the Peshtasar formation consists of 2 km of volcanics and is located stratigraphically just below the Pirembel formation. Also the upper part of the Arkevan contains slumps and olistostromes, which are indicative of syn-sedimentary deformation. It is possible that the onset of anoxia in the Paratethys basin is a diachronous event, and furthermore, the Maikop series were not deposited everywhere in the basin. For instance, no Maikop sediments have been found in Tajikistan and the Tarim basin in China (Bosboom et al., submitted), even though marine transgressions reaching those areas have been dated at about 37 Ma, which is after the onset of Pirembel sedimentation in the Talysh. Another explanation might be that anoxic conditions were only present in deeper parts of the basin. However, the Maikop of the Talysh was probably deposited in relatively shallow water, based on the grain-size and deltaic nature of the underlying Arkevan deposits (Vincent et al., 2005).

Paleogeographic maps such as those of Popov et al. (2004) and Berberian and King (1981), the latter of which is shown in Figure 25, indicate that during the Oligocene, the whole Talysh region was already uplifted and erosion was taking place. The Alborz in Iran, and possibly parts of the Iranian Talysh were already partly uplifted during the Late Eocene. Furthermore, Davoudzadeh et al. (1997) agree that the northern Alborz and the South Caspian coastal areas were land masses throughout the Eocene. Thence, coastlines could not have been very far away. The study of Berberian and King (1981) suggests that the Zeivar formation in Iran is equivalent to the Maikop. Zeivar deposits are only reported on the southeastern border of the Caspian Sea (Berberian and King, 1981). Late Eocene and Early Oligocene deposits of the Alborz comprise sediments that have a very different character than those of the Talysh, indicating that the two areas were not part of the same basin during that time. Uplift of the Talysh is estimated by Berberian and King (1981) after Late Eocene movements.

A general fining upwards trend is evident within section AZ15 (see Figure 4), from the upper Arkevan to the top of the section. A possible explanation is that tectonic movements caused subsidence of the Talysh basin, which led to a decrease in grain-size of the deposits. Additionally, this deepening of the basin could have led to decreased circulation, resulting in anoxic bottom conditions.

Nonetheless, a climatic cause for the onset of anoxia cannot be entirely ruled out, as around 37.3 Ma, the first Antarctic ice-sheets began to form, according to Zachos et al. (2001), coinciding with the boundary between the Arkevan and the Pirembel formation (see Figure 24). It is possible that the formation of these ice-sheets resulted in a sea-level drop that caused restriction of large-scale currents, leading to a decrease in basin circulation of the Paratethys basin. However, the sea level curve of Miller et al. (2005) shows a clear peak at 37.3 Ma. It is deemed unlikely that such a rapid rise and consecutive fall in sea level would have led to a prolonged restriction of the basin, as the sea level before and after this peak seems to be around the same level. Also, the $\delta^{18}\text{O}$ curves of both Zachos et al. (2001) and Miller et al. (2005) do not show any increase around this time, which would be expected for a major eustatic sea-level drop.

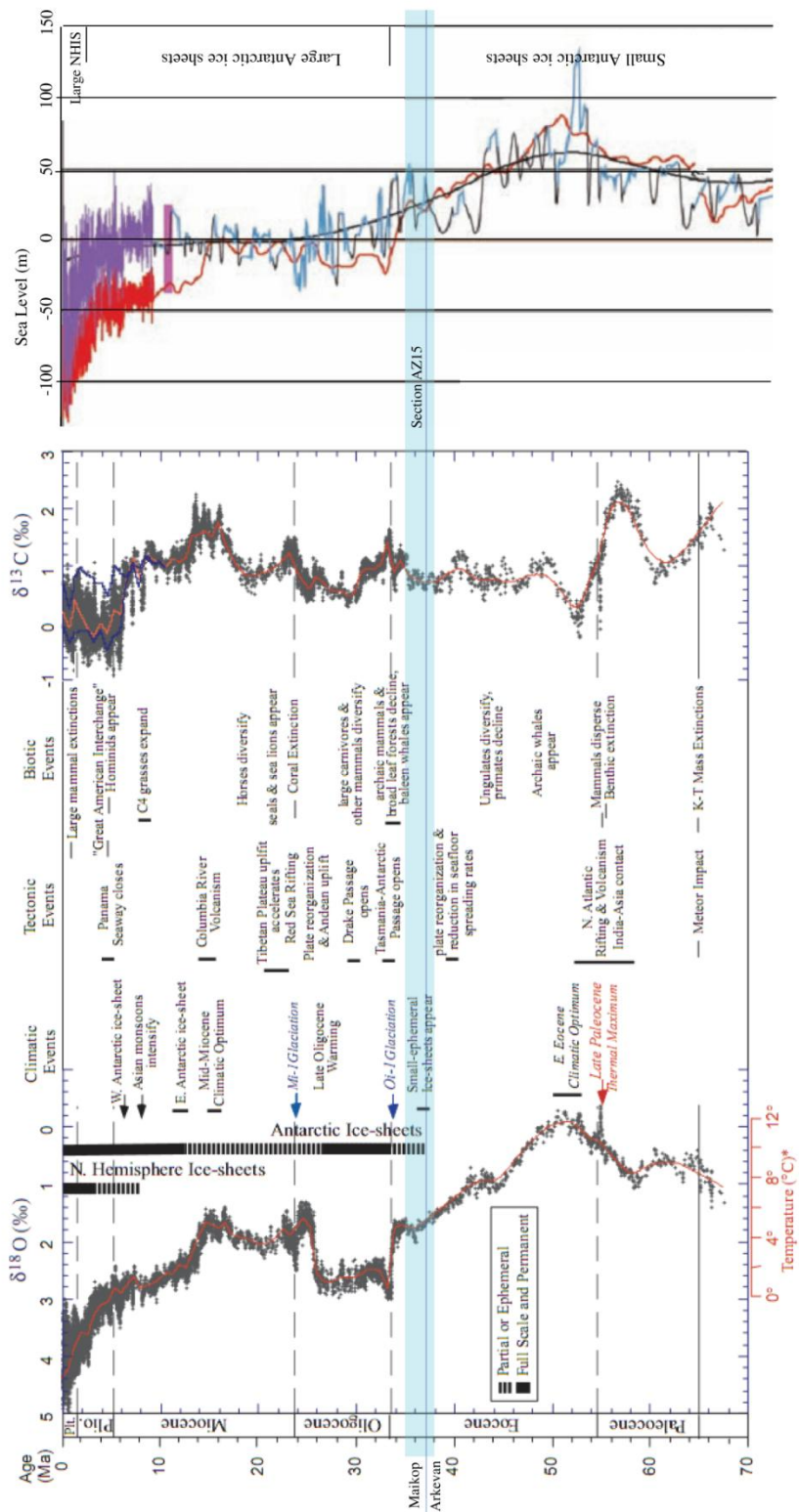


Figure 24: Age of section AZ15 and the Arkevan - Maikop boundary (Modified after Zachos et al. (2001) and Miller et al. (2005)) Light blue line in the right part represents the sea-level reconstruction of Miller et al. (2005) derived by backstripping (7-100 Ma), purple line is the global sea-level derived from $\delta^{18}\text{O}$ (0-7 Ma), red line is reconstruction from $\delta^{18}\text{O}$ of benthic foraminifera (0-100 Ma).

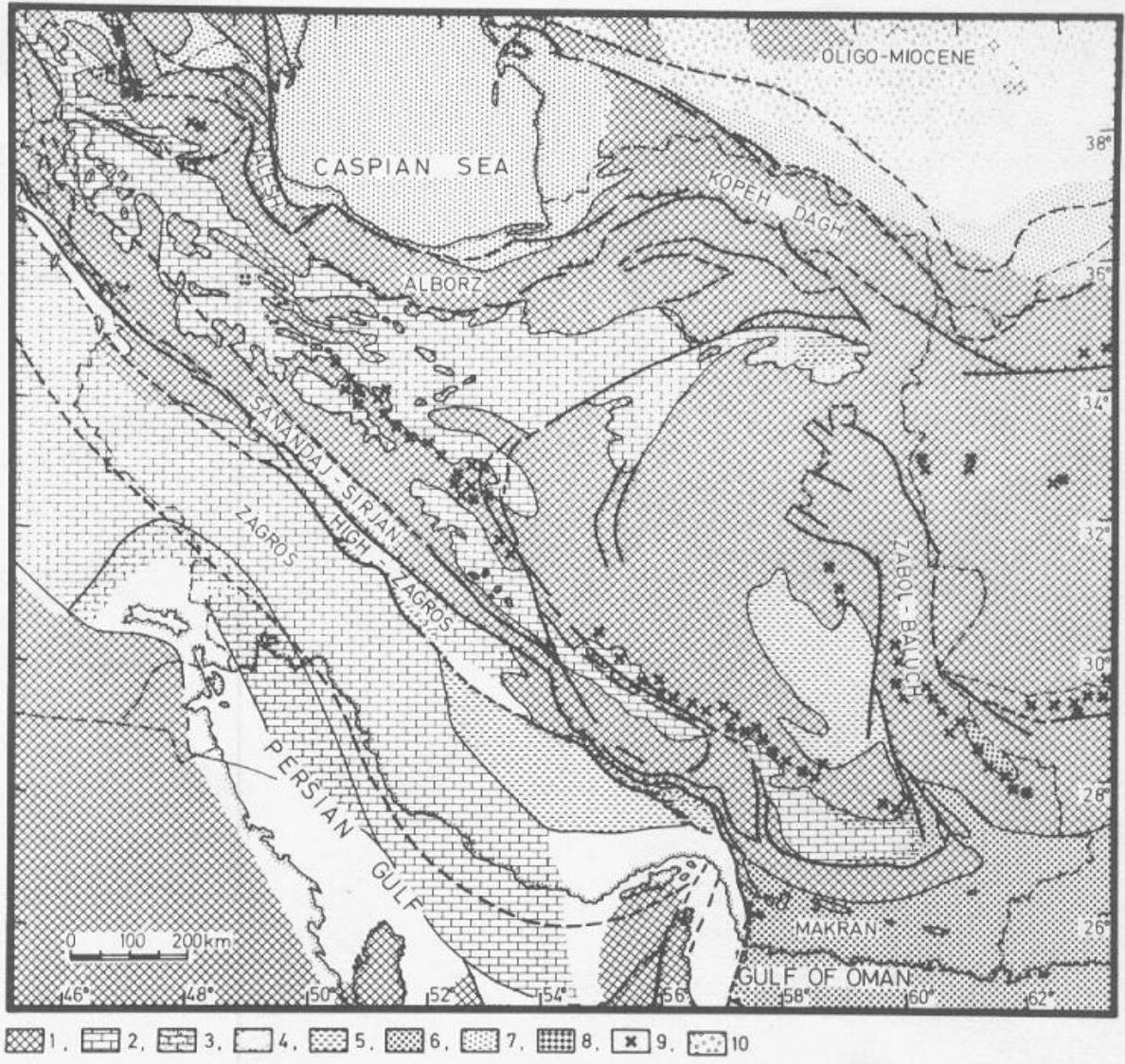


Figure 25: Paleogeographic map of Iran during Oligocene-Miocene, from Berberian and King (1981). Relevant legend: number 1: Mountainous regions, area of erosion and non-marine sedimentation; and number 7: Molasse (Zeivar Fm and Maikop Series composed of conglomerate, clay and tuffaceous sandstone) in northwestern Iran and Vindobonian marls in the Caspian region (Berberian and King, 1981)

Volcanics

The region of the Talysh has probably experienced little north- or southward movement due to the Arabia-Eurasia collision since the Eocene, so a radical difference in inclination compared to the present-day field is not expected. The value of the present day field (GAD value) is around 58°. Whether any rotations should be expected remains unclear, although a counterclockwise rotation of 20° has been suggested by Khalafly (2001). However, the three distinct groups from section AZ14 and AZ16 cannot represent the average magnetic field for the Eocene. It is unlikely that the values for the three groups are caused by overprinting, because an overprint would lead to very similar directions for all three groups. It is also unlikely that they are three different blocks that have rotated and tilted, as no faults or

folds have been observed within section AZ16 that would be needed to explain the results. Although the groups lie quite far apart in order to explain secular variation (e.g. (Knight et al., 2004)), it seems the most likely interpretation. According to Vincent et al. (2005), the Peshtasar formation was deposited over roughly 2 Myr, based on Ar-Ar dating of a flow on the bottom and on the top of the section. As the three groups represent three spot-readings of the magnetic field and do not average-out secular variation, it is highly unlikely that the Peshtasar formation was deposited by a uniform extrusion during 2 Myr. Instead, the Peshtasar formation was probably deposited during three short-lived magmatic pulses, of a maximum duration of hundreds to thousands of years. This results in eruption speeds that are quite large, as the lower group, consisting of AZ16A-AZ16K spans 1.5 km stratigraphically. However, the horizontal extent of the basalts is probably not very large, based on the map of Vincent et al. (2005) as is shown in Figure 1.

It is still possible that there is time in between the groups, such that the lower and upper group have a considerable time gap (of 2 Myr) in between them, to explain the results of the Ar-Ar analysis of Vincent et al. (2005), but in that case, more sediment in between the groups would be expected. Only very minor amounts of sediment have been found in section AZ16.

No uncertainties (aside from standard analytical uncertainties) are given for the Ar-Ar ages of Vincent et al. (2005). However, if the adopted ages are correct, an age can be estimated for each of the groups. On the base of the Peshtasar section, (close to location AZ16A of this research) an age of 40.5 Ma is assigned to sample TA92.6. The base of the Peshtasar section is correlated to sample TA9.1, where an age of 39.7 Ma is assigned. TA82 is located near section AZ14 of this research. An age of 39.2 Ma is assigned to this location. Integrating these ages with the three groups leads to an age of 40.5 Ma for the lower group. The middle group has an age of 39.2 Ma, as this can be correlated with sample TA82.1. The upper group then has an age of 38.3 Ma. It remains unclear how the age of 39.7 Ma for sample TA9.1 fits in, because that is 0.8 Myr younger than the lowest group, but 0.5 Myr older than the age of the middle group (see also Figure 31 in the appendix).

Geochemistry

Lavas very rarely reach the surface without experiencing processes that modify their chemical composition. Lavas are usually affected by processes as crustal assimilation (AFC), fractional crystallization (FC), partial melting or magma mixing, which leads to evolved compositions. Magmas that are derived directly from the mantle are called primary magmas. These magmas have undergone less differentiation on their way to the surface and are characterized by a high magnesium number. As all trends of major elements are flat, processes that are mentioned before are unlikely to have affected the composition of the magma. Also, magnesium numbers of the samples of this study are near or within the range of primary mantle magmas. These two factors indicate a lack of magma-evolution, which is consistent with the hypothesis that the three groups represent short-lived episodes of volcanism. As the three groups of magmas are all near the range of primary magmas, they are not affected by AFC and FC and also have different geochemical compositions, they probably represent three non-related magma-chambers.

The mid-ocean ridge normalized trace element abundance patterns (also known as spider diagrams, see Figure 20) of the samples are very similar to island arc volcanoes found in other parts of the world (e.g. Handley et al., 2007). The anomalies in Nb, Ta and Zr are also clear evidence for relation of the magmas to a subduction zone (Baier et al., 2008). If the volcanism took place in a back-arc setting, these anomalies might still be present, as back-arcs are always related to subduction. Back-arc basin basalts (BABB) usually vary in geochemical composition anywhere between MORB-like signatures and arc-like signatures. Ideally, a comparison of the back-arc and the related arc would be made. In this case, that would be the UDMA. However, no high quality average geochemical data from this arc have been found, so a comparison with other arcs is made. In Figure 26, relevant trace element ratios (K/Rb and Ce/Pb) are plotted together with a comparison of the Mariana arc and Mariana back-arc (Gribble et al., 1998). The Mariana arc is chosen, as Late Cretaceous volcanism from the region had a geochemical signature resembling that of the Mariana arc (Kazmin et al., 1986). This figure shows that all samples fall entirely within the range of samples from the arc. None of the samples from the Talysh plot within the range of the Mariana back-arc. The Ce/Pb ratio may in theory reflect a contamination with sediment, but this is unlikely, as the samples have low Ce/Pb ratios, compared to the Mariana back-arc, whereas sediment contamination would yield higher Ce/Pb ratios.

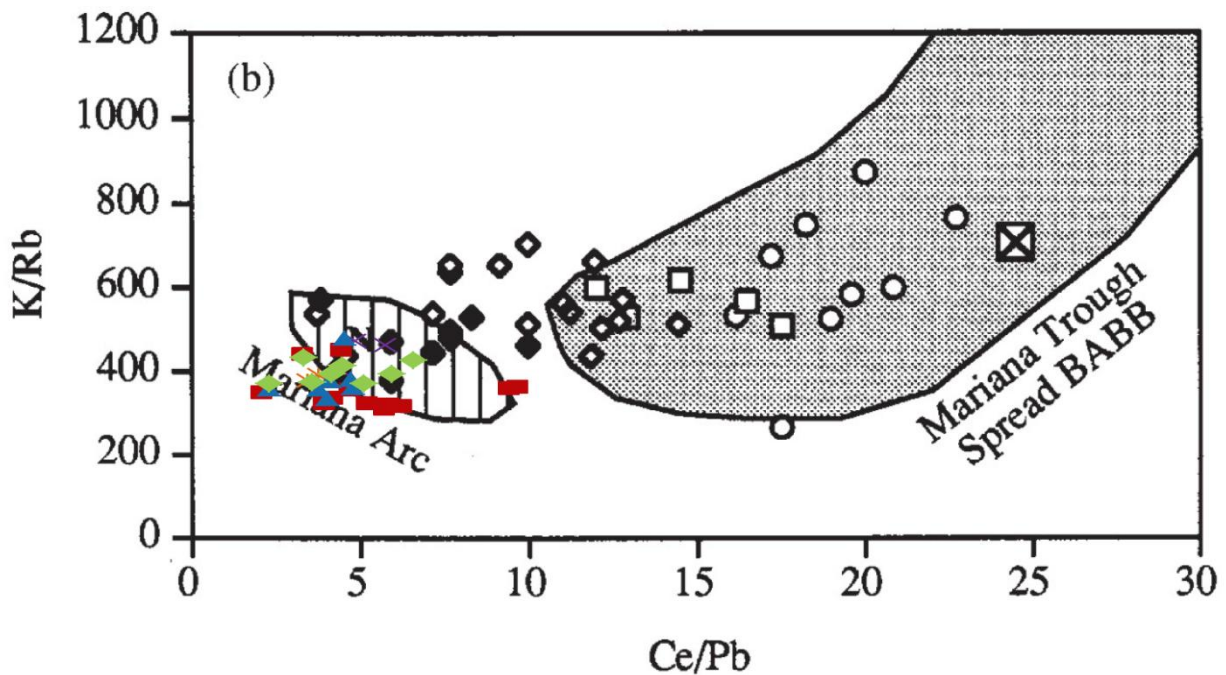


Figure 26: K/Rb ratio relative to Ce/Pb ratio and a comparison with the Mariana arc and Mariana back-arc (from: Gribble et al., 1998). Legend is equal to previous figures.

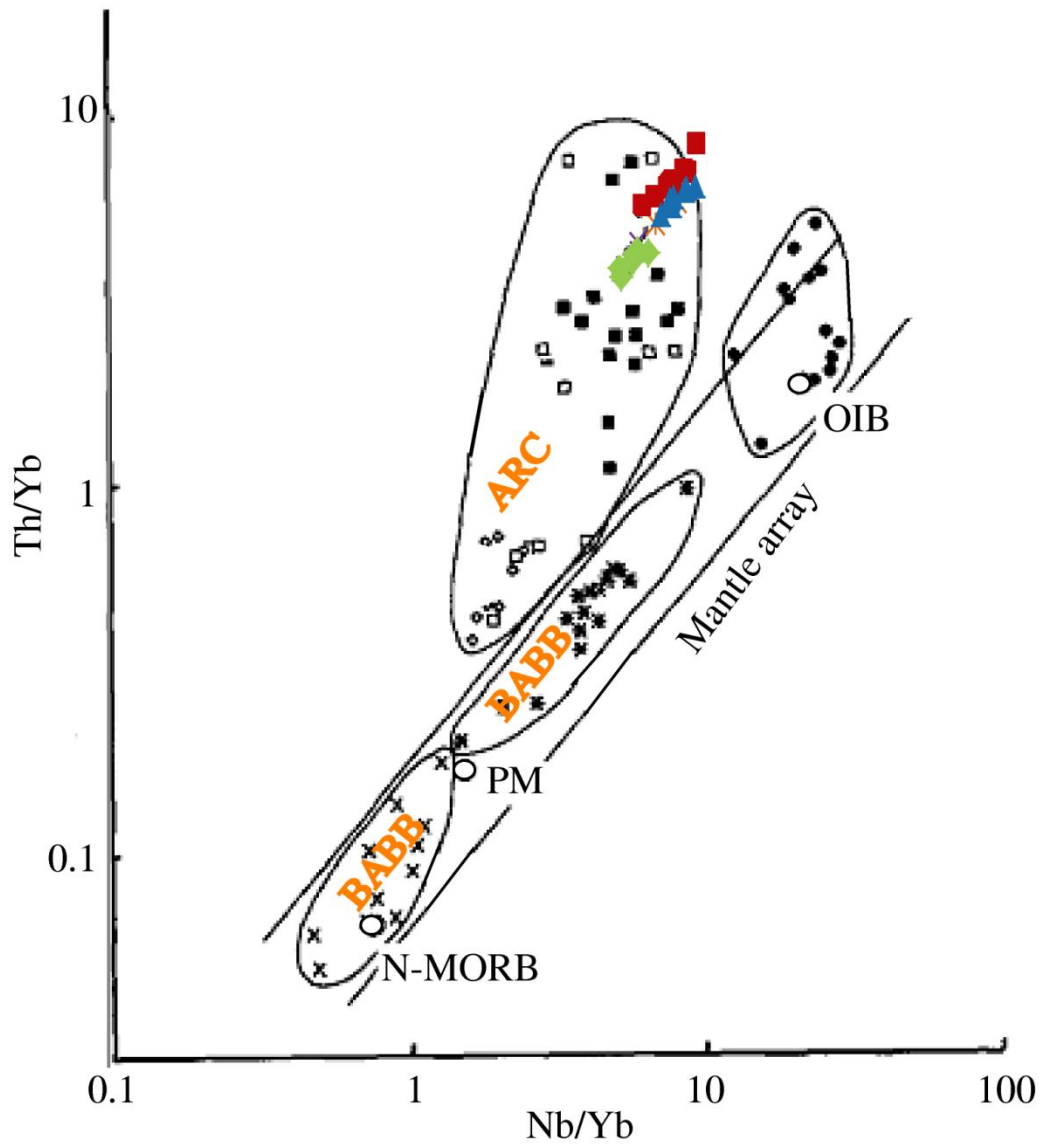


Figure 27: Th/Yb ratio relative to Nb/Yb ratio and a comparison with the Japan Sea back-arc (Modified after: (Poulet et al., 1994)). The ARC field represents arc-related lavas; BABB field represents back-arc basin basalts. OIB = ocean island basalt, PM = primary mantle, N-MORB = normal mid-ocean ridge basalt. Other legend is equal to previous figures.

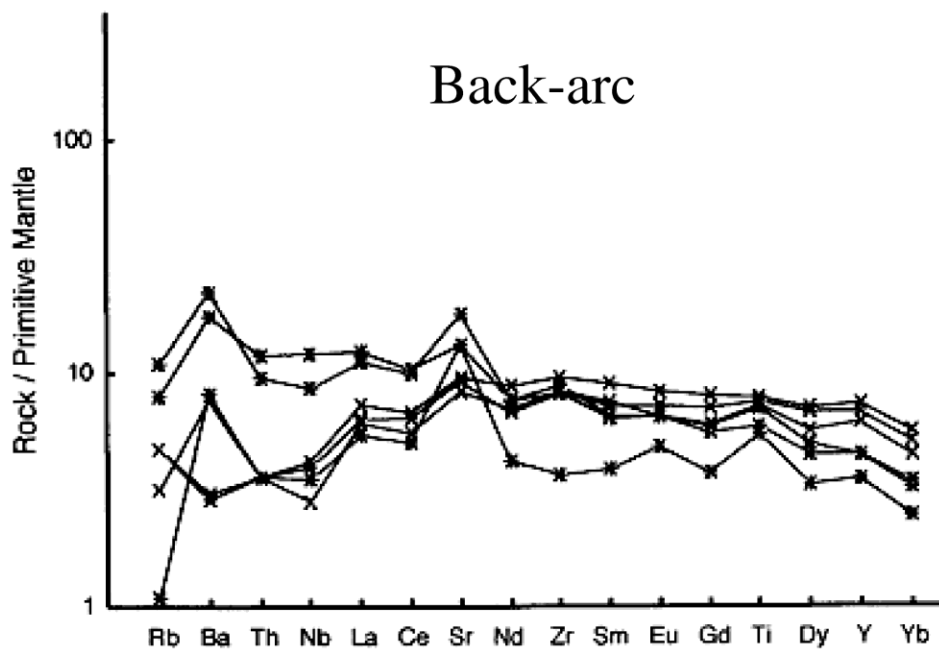
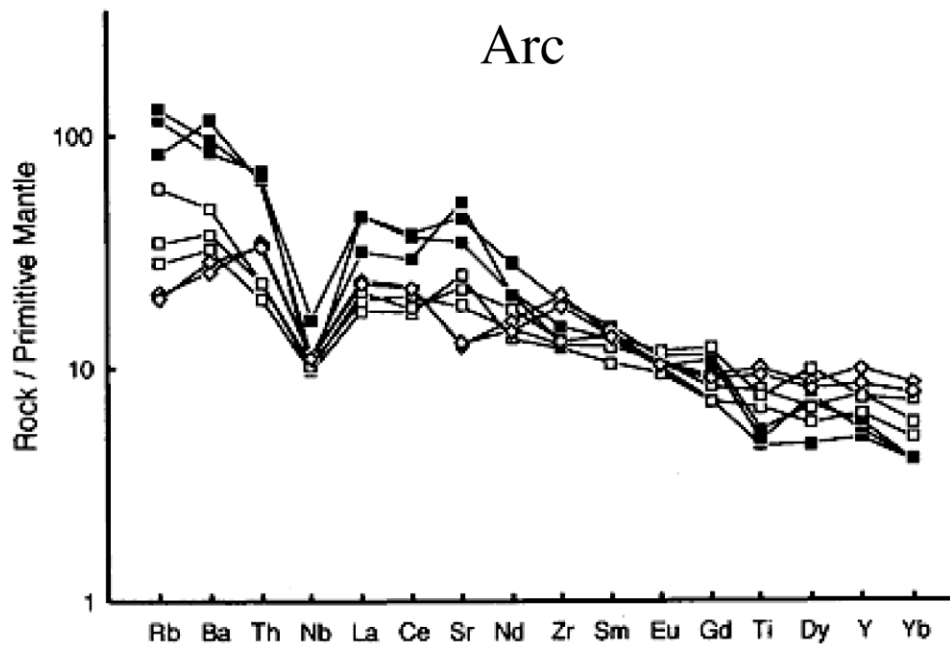


Figure 28: Spider diagrams of arc basalts (ARC field in Figure 27) and back-arc basalts (BABB in Figure 27). (Modified after: Poulet et al., 1994)

In Figure 27, the ratios of Th/Nb versus Nb/Yb are plotted on top of the comparison of different types of basalt from the Japan Sea (Poulet et al., 1994). The Talysh samples all plot in or near the ARC field,

which are arc-like lavas (Poucllet et al., 1994). BABB fields represent back-arc basin basalts, but none of the Talysh samples plot within this reach.

The spider diagram patterns (Figure 20) are also all characteristic for continental arc basalts (Poucllet et al., 1994; Verdel et al., 2011). Arc-like signatures have typical Nb troughs, Th spikes, LILE and Sr enrichment and relative HREE depletion. All samples of this study exhibit these characteristics. Back-arc basin characteristics include: a low LILE content, no Th anomaly, and a flat REE pattern. None of the basalts of this study seem to represent back-arc basin basalts. When patterns are compared with groups 1 (arc lavas) and group 2 (BABB) of Poucllet et al. (1994) (see Figure 28), they are much more similar to the arc lavas than the BABB. Spider diagrams from Asiabanha and Foden (2012), Vincent et al. (2005) and Verdel et al. (2011) show the same patterns. (The difference in normalization with N-MORB or primitive mantle has little effect on the patterns. For the primitive mantle normalized spider diagram, see appendix.) The scenario that Golonka (2004) proposes, in which volcanism is linked to ocean spreading in a back-arc basin is thus deemed highly improbable and any evidence for this scenario is lacking.

The study of Verdel et al. (2011) finds similar arc-like trace element patterns, but these are explained by addition of slab-derived fluids in a back-arc extensional setting. A scenario is proposed which involves a steep slab subducting beneath Eurasia, which flattens during the Cretaceous, steepens again during the Eocene (in order to explain extension that is linked to rollback) and is in the pre-Cretaceous steep position during the Oligocene in order to explain OIB-like signatures found in Oligocene basalts. This scenario is considered unlikely, because Verdel et al. argue that Eocene volcanism is not linked to a flat slab (Verdel et al., 2011), even though the flat slab is still present in their final figure (which is Figure 8 in: Verdel et al., 2011). Furthermore, if the flat slab is still present, rollback is unlikely to take place (Sdrolias and Müller, 2006).

Shoshonitic compositions of Eocene volcanics have been reported also from the UDMA and other parts of Iran (Verdel et al., 2011; Torabi, 2009; Dilek et al., 2010). Shoshonites are usually found in (subduction-related) arcs. Arcs often exhibit a progression along the tholeiite – calc-alkaline – shoshonite path. Shoshonites are generally formed later, stratigraphically higher and are associated with greater heights above the Benioff zone. Therefore, they are usually found in mature arcs. In regions that are tectonically active and unstable, shoshonites are associated with deformation of the arc, near the termination of subduction, or when there is a transition between two subduction regimes that have a different orientation (Morrison, 1980). Shoshonites are often associated with slab breakoff (Dilek et al., 2010; Verdel et al., 2011). It is thus possible that the shoshonites of the Talysh represent short-lived episodes of volcanism caused by cessation of subduction or breakoff of the Neotethys slab. This is in agreement with the scenario as proposed by Agard et al. (2011), which involves Paleocene-Eocene slab breakoff, large shifts in arc magmatism and episodes in which upper crustal extension takes place. As the AMA is located further away from the trench, the exact relation with the UDMA remains unclear. If the AMA and UDMA have the same timing, it is possible that two parallel subduction zones (e.g. Zonenshain and Le Pichon, 1986; Kazmin et al., 1986) existed. If they do not have exactly the same timing, the two arcs might represent a shift in arc magmatism.

Conclusions

Different dating methods were used to determine the age of the transition from the Arkevan formation to the Pirembel formation. This transition is generally assumed to be the onset of sedimentation of the Maikop series within the Talysh.

All analyzed samples were barren of dinoflagellates. Large benthic foraminifera (Nummulites) were found in the lower parts of sections AZ14 and AZ15 and interpreted as Priabonian. No magnetostratigraphy could be established for section AZ14 due to (at least partly) remagnetization. A low resolution magnetostratigraphy was obtained for the upper part of the Arkevan formation and lower part of the Pirembel formation in section AZ15. This magnetostratigraphy was combined with a biostratigraphy based on nannoplankton assemblages. Even though half of the samples were barren, the other half of the samples contained nannoplankton assemblages that are characteristic for zones MNP18 and MNP19 (Bartonian - Priabonian). This integrated magneto- and biostratigraphy places the base of section AZ15 within chron C17n.2n. The youngest chron that seems evident is C16n. Within the interval between the base of C17n.1r (37.9 Ma) and the base of C16n (36.1) Ma, there is circa 330 meters of stratigraphy. This leads to an estimate of the sedimentation rate for section AZ15 of 18 cm/kyr. Deposition rates might be higher for the Arkevan formation, since this formation is composed of coarser material. Using the average rate of 18 cm/kyr, the base of the section is estimated at 38 Ma, the Arkevan – Pirembel boundary at 37.3 Ma and the top of the section at 35.1 Ma. If this boundary truly represents the onset of Maikop sedimentation and consequently the onset of anoxia, the anoxia started some 3.4 Myr before the EOT. Thus, the anoxia is probably related to a decrease in circulation caused by tectonics. Slumps and olistostromes that are present in the upper part of the Arkevan formation are indicators of an active tectonic regime, as well as the presence of around 2 km of volcanics of the Peshtasar formation, which is stratigraphically just below the Pirembel formation. Although around 37.3 Ma the formation of the first Antarctic ice-sheets is reported (Zachos et al., 2001), therefore, a climatic cause for the change in sedimentation cannot be ruled out. The effect of this glaciation on the global sea-level cannot be established due to the resolution of the sea-level reconstruction.

Paleomagnetic analyses of the volcanics of section AZ16 show three distinct groups. Paleomagnetic therefore do not represent a continuous record of secular variation, but are interpreted to represent three distinct (and very different) intervals, each interval showing some secular variation over a relatively short time. Therefore, emplacement must have taken place over a relatively short amount of time, 10^2 - 10^3 yr. for each group. Extrusion (or intrusion, because some volcanic units are sills) rates must have been very high, since the lower group has a stratigraphic thickness of 1.5 kilometers. The lower group consists of sites AZ16A-K, the middle group of sites AZ16L-P, T and U, and the upper group of sites AZ16Q, R, S, V-Z. These groups are also distinct in the geochemistry. Based on equal geochemical composition, AZ14A and B belong to the middle group of AZ16 and AZ14C, D and F belong to the upper group of AZ16. The paleomagnetic results of AZ14 do not correspond with the three groups, since AZ14 is interpreted to be (partly) remagnetized. Volcanics of AZ14 and AZ16 are all trachybasalts and basaltic trachyandesites with trace element signatures characteristic for arc-lavas. Consequently, it is interpreted that volcanics formed in an arc-setting, which is in contrast with previous interpretations that assumed volcanics were formed in a back-arc setting. Major element geochemistry shows that samples have

shoshonitic compositions. Melts were not affected by assimilation and fractional crystallization processes and are all primary melts. Ar-Ar ages for the basalts of section AZ14 and AZ16 are expected in early 2013, but based on the relative stratigraphic position and the age of the Nummulites found in the lower part of section AZ14, sections AZ14 and AZ16 can be assigned a Late Eocene age. Volcanism is probably linked to a major phase of Eocene shoshonitic volcanism, which occurred predominantly in Iran. This episode of volcanism is linked to breakoff of the Neotethys slab during the Paleocene-Eocene, which also caused episodic extension of the upper crust.

Suggestions for further research

To get more information about the geochemistry, ICP-MS analyses should be performed, to get abundances of even more elements. In order to obtain more information on the volcanic formations, isotope studies (Sr, Nd and Hf for example) could be performed. These data should ideally be compared with samples from the UDMA, which is generally accepted as the main arc of the region. To assess the tectonic regime in which the large scale volcanism developed, field studies concerning sedimentation and structures should be performed in the Talysh region, involving the construction of cross-sections. Finding the time-equivalent formations of the Peshtasar, Arkevan and Maikop in Iran would lead to a better understanding of the paleogeography of the region, because the Lower and Upper Red formations are of Eocene age and are reported to consist of continental redbeds. The time-equivalent formation of the Maikop is the Qom formation, which consists of marine mixed carbonate-siliciclastic deposits. This is quite different from the anoxic shales of which the Maikop is composed, indicating that they were probably deposited in different basins. Geochemical studies of the Pirembel formation would allow comparison with the Maikop series in Maykop, Russia and the Kura basin, Azerbaijan. It might then be established whether the Pirembel formation really is equivalent to the Maikop series.

Acknowledgements

This research was partly financed by the Molengraaff fund. I would like to thank everyone at Fort Hoofddijk, in particular my supervisors Wout Krijgsman and Cor Langereis. I would also like to thank Elmira Aliyeva, Eldar Huseynov, Gingiz Aliyev and Kamram Aliyev, from the Geological Institute in Baku as well as Maud Meijers (Nice University) for her help in the field. At the VU Klaudia Kuiper, Roel van Elsas, Sergei Matveev and Christel Bontje. At the UU Manfred van Bergen, Arjen Grothe, Otto Stiekema, Wim Spakman and Douwe van Hinsbergen. Furthermore W. Renema (Naturalis Leiden) for the large benthic foraminifera analysis, G. Villa (University of Parma) for nannoplankton analysis. Also I would like to thank Stefano Branca of the Istituto Nazionale di Geosifica e Vulcanologia - Sezione di Catania for looking at the photographs of section AZ16.

References

- Abrams, M. a., Narimanov, A. a., 1997. Geochemical evaluation of hydrocarbons and their potential sources in the western South Caspian depression, Republic of Azerbaijan. *Marine and Petroleum Geology* 14, 451–468.
- Adamia, S., Zakariadze, G., Chkhotua, T., Sadradze, N., Tsereteli, N., Chabukiani, A., Gventsadze, A., 2011. Geology of the Caucasus : A Review. *Turkish Journal of Earth Sciences* 20, 489–544.
- Agard, P., Omrani, J., Jolivet, L., Whitechurch, H., Vrielynck, B., Spakman, W., Monié, P., Meyer, B., Wortel, R., 2011. Zagros orogeny: a subduction-dominated process. *Geological Magazine* 148, 692–725.
- Asiabanha, A., Foden, J., 2012. Post-collisional transition from an extensional volcano-sedimentary basin to a continental arc in the Alborz Ranges, N-Iran. *Lithos* 148, 98–111.
- Azizbekov, S.A., 1972. Geology of the USSR: Azerbaijan SSR (in Russian), v.57. Nedra, Moscow.
- B. Ellwood, E. Crick, A. El Hassani, S. Benoist, R. Young, 2000. Magnetosusceptibility event and cyclostratigraphy method applied to marine rocks: detrital input versus carbonate productivity *Geology* 28, 1135–1138.
- Baier, J., Audétat, A., Keppler, H., 2008. The origin of the negative niobium tantalum anomaly in subduction zone magmas. *Earth and Planetary Science Letters* 267, 290–300.
- Berberian, M., King, G.C.P.C.P., 1981. Toward a paleogeography and tectonic evolution of Iran. *Canadian Journal of Earth Sciences* 18, 210–265.
- Berner, R.A., 1984. Sedimentary pyrite formation: An update. *Geochimica et Cosmochimica Acta* 48, 605–615.
- Berner, R.A., Raiswell, R., 1983. Burial of organic carbon and pyrite sulfur in sediments over phanerozoic time: a new theory. *Geochimica et Cosmochimica Acta* 47, 855–862.
- Brunet, M.-F., Korotaev, M. V., Ershov, A. V., Nikishin, A.M., 2003. The South Caspian Basin: a review of its evolution from subsidence modelling. *Sedimentary Geology* 156, 119–148.
- Davoudzadeh, M., Lammerer, B., Weber-Diefenbach, K., 1997. Paleogeography, stratigraphy, and tectonics of the tertiary of Iran. *Neues Jahrbuch fur Geologie und Palaontologie - Abhandlungen* 205, 33–67.
- Dilek, Y., Imamverdiyev, N., Altunkaynak, Ş., 2010. Geochemistry and tectonics of Cenozoic volcanism in the Lesser Caucasus (Azerbaijan) and the peri-Arabian region : collision-induced mantle dynamics and its magmatic fingerprint. *International Geology Review* 4-6, 536–578.
- Dunlop, D.J., Özdemir, Ö., 1997. *Rock Magnetism - Fundamentals and Frontiers*.

- Efendiyeva, M. a., 2004. Anoxia in waters of the Maikop paleobasin (Tethys Ocean, Azeri sector), with implications for the modern Caspian Sea. *Geo-Marine Letters* 24, 177–181.
- Golonka, J., 2004. Plate tectonic evolution of the southern margin of Eurasia in the Mesozoic and Cenozoic. *Tectonophysics* 381, 235–273.
- Gradstein, F.M., Ogg, J.G., Schmitz, M., Ogg, G., 2012. *The Geologic Time Scale 2012*.
- Gribble, R.F., Stern, R.J., Newman, S., Bloomer, S.H., O’Hearn, T., 1998. Chemical and Isotopic Composition of Lavas from the Northern Mariana Trough: Implications for Magmagenesis in Back-arc Basins. *Journal of Petrology* 39, 125–154.
- Guliyev, I.S., Tagiyev, M.F., Feyzullayev, A.A., 2001. Geochemical Characteristics of Organic Matter from Maikop Rocks of Eastern Azerbaijan. *Lithology and Mineral Resources* 36, 324–329.
- Handley, H.K., Macpherson, C.G., Davidson, J.P., Berlo, K., Lowry, D., 2007. Constraining Fluid and Sediment Contributions to Subduction-Related Magmatism in Indonesia: Ijen Volcanic Complex. *Journal of Petrology* 48, 1155–1183.
- Hay, W.W., 1996. Tectonics and climate. *Geologische Rundschau* 85, 409–437.
- Hay, W.W., 1998. Detrital sediment fluxes from continents to oceans. *Chemical Geology* 145, 287–323.
- Hudson, S.M., Johnson, C.L., Efendiyeva, M. a., Rowe, H.D., Feyzullayev, A. a., Aliyev, C.S., 2008. Stratigraphy and geochemical characterization of the Oligocene–Miocene Maikop series: Implications for the paleogeography of Eastern Azerbaijan. *Tectonophysics* 451, 40–55.
- Ismail-Zade, A.D., Veliev, M.M., Mamedov, M.M., Bagirov, A.E., 1995. Tectonic position of the Talysch mafic-ultramafic complex. *Geotectonics* 29, 184–186.
- Johnson, C.L., Hudson, S.M., Rowe, H.D., Efendiyeva, M. a., 2010. Geochemical constraints on the Palaeocene-Miocene evolution of eastern Azerbaijan, with implications for the South Caspian basin and eastern Paratethys. *Basin Research* 22, 733–750.
- Kazmin, V.G., Knipper, A.L., Sbortshikov, I.M., Zonenshain, L.P., Boulin, J., Ricou, L.-E., 1986. Volcanic belts as markers of the Mesozoic-Cenozoic active margin of Eurasia. *Tectonophysics* 123, 123–152.
- Kirschvink, J.L., 1980. The least-squares line and plane and the analysis of palaeomagnetic data. *Geophysical Journal International* 62, 699–718.
- Knight, K.B., Nomade, S., Renne, P.R., Marzoli, a., Bertrand, H., Youbi, N., 2004. The Central Atlantic Magmatic Province at the Triassic–Jurassic boundary: paleomagnetic and $^{40}\text{Ar}/^{39}\text{Ar}$ evidence from Morocco for brief, episodic volcanism. *Earth and Planetary Science Letters* 228, 143–160.
- Miller, K.G., Kominz, M.A., Browning, J. V, Wright, J.D., Mountain, G.S., Katz, M.E., Sugarman, P.J., Cramer, B.S., Christie-Blick, N., Pekar, S.F., 2005. The Phanerozoic Record of Global Sea-Level Change. *Science* 310, 1293–1298.

- Morrison, G.W., 1980. Characteristics and tectonic setting of the shoshonite rock association. *Lithos* 13, 97–108.
- Motavalli-Anbaran, S.-H., Zeyen, H., Brunet, M.-F., Ardestani, V.E., 2011. Crustal and lithospheric structure of the Alborz Mountains, Iran, and surrounding areas from integrated geophysical modeling. *Tectonics* 30, TC5012.
- Mouthereau, F., Lacombe, O., Vergés, J., 2012. Building the Zagros collisional orogen: Timing, strain distribution and the dynamics of Arabia/Eurasia plate convergence. *Tectonophysics* 532-535, 27–60.
- Mullender, T.A.T., Velzen, A.J., Dekkers, M.J., 1993. Continuous drift correction and separate identification of ferrimagnetic and paramagnetic contributions in thermomagnetic runs. *Geophysical Journal International* 114, 663–672.
- Passier, H.F., Bosch, H.J., Nijenhuis, I.A., Lourens, L.J., Bottcher, M.E., Leenders, A., Sinninghe Damsté, J.S., De Lange, G.J., De Leeuw, J.W., 1999. Sulphidic Mediterranean surface waters during Pliocene sapropel formation. *Nature* 397, 146–149.
- Popov, S. V., Rögl, F., Rozanov, A., Steininger, F.F., Shcherba, I.G., Kovac, M., 2004. Lithological-Paleogeographic maps of Paratethys. 10 Maps Late Eocene to Pliocene. *Courier Forschungsinstitut Senckenberg* 250, 1–46.
- Popov, S. V., Sychevskaya, E.K., Akhmet'ev, M.A., Zaporozhets, N.I., Golovina, L.A., 2008. Stratigraphy of the Maikop Group and Pteropoda Beds in northern Azerbaijan. *Stratigraphy and Geological Correlation* 16, 664–677.
- Pouclot, A., Lee, J.-S., Vidal, P., Cousens, B., Bellon, H., 1994. Cretaceous to Cenozoic volcanism in South Korea and in the Sea of Japan: magmatic constraints on the opening of the back-arc basin. *Geological Society, London, Special Publications* 81, 169–191.
- Roberts, A.P., 1995. Magnetic properties of sedimentary greigite (Fe₃S₄). *Earth and Planetary Science Letters* 134, 227–236.
- Roberts, A.P., Chang, L., Rowan, C.J., Horng, C.-S., Florindo, F., 2011. Magnetic properties of sedimentary greigite (Fe₃S₄): An update. *Reviews of Geophysics* 49, RG1002.
- Sdrolias, M., Müller, R.D., 2006. Controls on back-arc basin formation. *Geochemistry Geophysics Geosystems* 7.
- Soták, J., 2010. Paleoenvironmental changes across the Eocene-Oligocene boundary: insights from the Central-Carpathian Paleogene Basin. *GEOLOGICA CARPATHICA* 61, 393–418.
- Torabi, G., 2009. Subduction-related Eocene Shoshonites from the Cenozoic Urumieh-Dokhtar Magmatic Arc (Qaleh-Khargooshi Area , Western Yazd Province , Iran). *Turkish Journal of Earth Sciences* 18, 583–613.

- Tyson, R. V., Pearson, T.H., 1991. Modern and ancient continental shelf anoxia: an overview. Geological Society, London, Special Publications 58, 1–24.
- Velzen, A.J., Zijdeveld, J.D.A., 1995. Effects of weathering on single-domain magnetite in Early Pliocene marine marls. *Geophysical Journal International* 121, 267–278.
- Verdel, C., Wernicke, B.P., Hassanzadeh, J., Guest, B., 2011. A Paleogene extensional arc flare-up in Iran. *Tectonics* 30, 1–20.
- Vincent, S.J., Allen, M.B., Ismail-Zadeh, A.D., Flecker, R., Foland, K. a., Simmons, M.D., 2005. Insights from the Talysh of Azerbaijan into the Paleogene evolution of the South Caspian region. *Geological Society of America Bulletin* 117, 1513.
- Von der Heydt, A., Dijkstra, H. a., 2008. The effect of gateways on ocean circulation patterns in the Cenozoic. *Global and Planetary Change* 62, 132–146.
- Wilkin, R.T., Barnes, H.L., 1996. Pyrite formation by reactions of iron monosulfides with dissolved inorganic and organic sulfur species. *Geochimica et Cosmochimica Acta* 60, 4167–4179.
- Zachos, J., Pagani, M., Sloan, L., Thomas, E., Billups, K., 2001. Trends, rhythms, and aberrations in global climate 65 Ma to present. *Science (New York, N.Y.)* 292, 686–93.
- Zijderveld, J.D.A., 1967. AC demagnetization of rocks: analysis of results, in: Collinson, D.W., Creer, K.M. (Eds.), *Methods in Paleomagnetism*. Elsevier, Amsterdam, pp. 254–286.
- Zonenshain, L.P., Pichon, X.L.E., 1986. Deep basins of the black sea and caspian sea as remnants of mesozoic back-arc basins. *Tectonophysics* 123, 181–211.

Appendix

flow	stratigraphic height	notc		tc		tectonic correction		GPS coordinates	
		dec	inc	dec	inc	dec	inc	N	E
16A	0	206	-19.5	206.2	-2.1	291	17	38.86672	48.05018
16B	397.6	227.1	-11.3	226.6	4	291	17	38.87484	48.06173
16C	509.9	225.6	-9	225.4	6.5	291	17	38.8775	48.06395
16D	661.9	207.5	-25.4	207	-8.5	291	17	38.87975	48.07098
16E	740.9	205.9	-39.4	202.3	-31.5	291	17	38.88131	48.07336
16F	813.7	208.4	-7.9	207.9	-8.1	291	17	38.8829	48.07519
16G	934.1	205.6	-28.5	187.9	-11.9	291	17	38.88549	48.07825
16H	1134.4	209.8	-27.9	208.9	-11.1	291	17	38.88925	48.08513
16I	1365.1	218.3	-4.9	204	-1.9	291	17	38.89417	48.09118
16J	1429.1	224.4	-25.8	222.3	-10	291	17	38.89596	48.09346
16K	1452.2	200	-26.5	199.7	-9.2	291	17	38.89577	48.09434
16L	1615.4	209.6	-77.1	206.5	-65.1	293	12	38.90005	48.09632
16M	1641.8	235.2	-76	220.8	-65	293	12	38.90105	48.0966
16N	1796.2	242.5	-62.5	231.9	-52.6	293	12	38.90586	48.1018
16O	1819.1	205.1	-73.1	204.2	-61.1	293	12	38.90645	48.10301
16P	1865.3	231.7	-66.3	222.9	-55.3	293	12	38.90757	48.10542
16T	1928.3	235.9	-58.7	228	-48.2	293	12	38.90729	48.11422
16S	1964.0	155	-7.9	155.3	5.8	295	21	38.9109	48.10873
16Q	1968.0	133.6	-25.8	141.4	-17.7	295	21	38.9119	48.10588
16U	1972.6	225.6	-65.1	206.5	-65.1	293	12	38.90733	48.11948
16V	1979.1	132.8	-11.8	135.7	-4.8	290	22	38.90757	48.12012
16R	2021.7	129.8	-22.1	136.7	-15.5	295	21	38.91399	48.10417
16W	2080.9	123.8	-24.1	128.8	-10.9	290	22	38.5453	48.07425
16X	2092.5	127.6	-21.5	134.4	-15.6	290	22	38.54528	48.07487
16Y	2102.3	135.7	-20.1	141.2	-11.6	290	22	38.54519	48.07571
16Z	2132.6	138.3	-20.5	143.7	-11.2	290	22	38.54451	48.07971

Table 5: Stratigraphic level, averages per flow, tc and notc, tectonic correction and GPS coordinates of every sampled flow/sill of section AZ16

Sample Setting	AZ14A Sill	AZ14B Sill	AZ14C Sill	AZ14D Sill	AZ14F Flow	AZ16A Flow	AZ16B Flow	AZ16C Sill	AZ16D Sill	AZ16E Sill
<u>Major Elements (Wt%)</u>										
Fe2O3	9.27	8.44	9.97	9.54	8.48	8.34	8.84	8.56	8.94	8.84
MnO	0.15	0.18	0.18	0.16	0.15	0.15	0.16	0.16	0.17	0.16
TiO2	1.12	1.12	1.12	1.08	1.20	1.10	0.96	0.97	0.99	0.98
CaO	8.25	8.51	8.61	8.13	7.93	8.27	8.32	8.33	8.31	8.26
K2O	3.17	3.18	2.77	3.19	3.17	3.04	2.87	3.15	2.98	3.15
P2O5	0.47	0.47	0.46	0.43	0.48	0.37	0.36	0.37	0.38	0.36
SiO2	52.34	52.38	50.48	50.55	51.13	52.61	51.66	52.79	51.95	52.27
Al2O3	17.70	17.53	16.92	16.06	18.04	16.98	16.03	16.64	16.18	16.12
MgO	4.83	4.48	6.71	6.72	5.46	4.67	6.54	6.18	6.35	6.35
Na2O	2.95	2.94	2.55	2.82	2.73	2.91	2.76	2.88	2.79	2.81
BaO	0.08	0.08	0.07	0.11	0.15	0.07	0.07	0.08	0.07	0.08
LOI	1.40	1.12	1.99	2.90	2.33	1.08	0.65	0.83	0.74	0.89
Total	100.33	99.31	99.83	98.78	98.93	98.50	98.55	100.103	99.10	99.38
<u>Trace Elements (ppm)</u>										
Ba	684.96	694.62	645.38	984.51	1374.29	624.07	669.58	697.60	670.95	687.95
Ce	70.80	69.11	55.08	56.00	64.27	87.90	63.54	65.59	65.65	63.28
Co	26.91	28.51	32.77	34.25	29.97	29.28	30.82	28.45	29.76	30.11
Cr	163.33	176.77	235.12	243.82	287.19	173.55	283.34	250.22	271.28	258.78
Cu	99.99	100.28	95.40	69.05	107.46	70.55	64.94	59.69	69.26	58.90
Dy	5.71	6.13	4.45	5.66	4.31	4.19	5.20	3.36	3.01	2.96
Er	2.80	2.69	2.45	2.58	3.13	3.13	2.87	2.51	3.22	2.42
Ga	19.00	19.22	17.80	16.40	20.12	18.91	17.62	17.96	17.77	17.63
Hf	5.10	5.21	4.52	5.00	4.80	7.54	5.73	5.07	5.26	5.58
La	36.22	37.02	29.46	29.62	37.75	47.48	35.09	35.65	34.18	33.71
Mo	2.49	2.18	1.82	1.10	0.88	2.55	1.94	1.83	2.12	2.02
Nb	20.72	21.20	14.60	14.80	17.00	29.48	20.10	20.27	20.14	20.40
Nd	33.29	30.49	28.42	21.63	28.06	39.63	29.79	30.02	32.58	25.09
Ni	65.18	70.57	88.47	95.90	93.82	77.97	89.29	78.37	86.47	84.89
Pb	19.74	17.74	12.10	9.77	13.07	14.16	13.90	12.39	11.41	10.79
Pr	8.72	8.27	7.04	6.32	8.00	10.71	7.88	7.91	8.10	6.90
Rb	84.10	81.67	70.08	71.07	69.67	93.04	65.44	91.94	92.89	95.47
Sc	23.51	24.55	24.41	23.01	27.11	23.61	24.45	23.71	22.65	22.70
Sm	5.69	5.31	5.00	4.30	5.27	6.26	5.21	5.00	5.51	4.42
Sr	554.34	564.57	578.39	1055.45	606.34	527.79	598.53	596.12	579.58	580.91
Ta	0.38	1.47	0.60	2.19	2.13	1.69	2.21	0.72	1.48	1.23
Th	10.67	10.47	6.40	7.12	7.36	22.24	12.71	12.48	13.08	12.87
U	2.77	2.47	0.86	1.04	1.85	6.23	3.10	3.05	3.48	3.60
V	209.51	216.47	237.78	239.05	266.82	194.12	198.73	190.34	196.60	190.10
W	4.25	3.54	2.25	1.75	2.16	4.39	4.95	5.09	7.19	6.26
Y	25.35	25.28	22.59	20.88	24.43	28.42	23.87	23.91	24.10	24.04
Yb	2.38	2.90	2.57	2.32	2.65	2.90	2.37	2.14	2.18	2.49
Zn	84.82	90.12	78.37	70.44	98.18	89.13	88.07	74.01	77.90	78.14
Zr	168.39	171.51	108.76	81.41	126.26	262.65	171.15	170.58	173.45	173.58

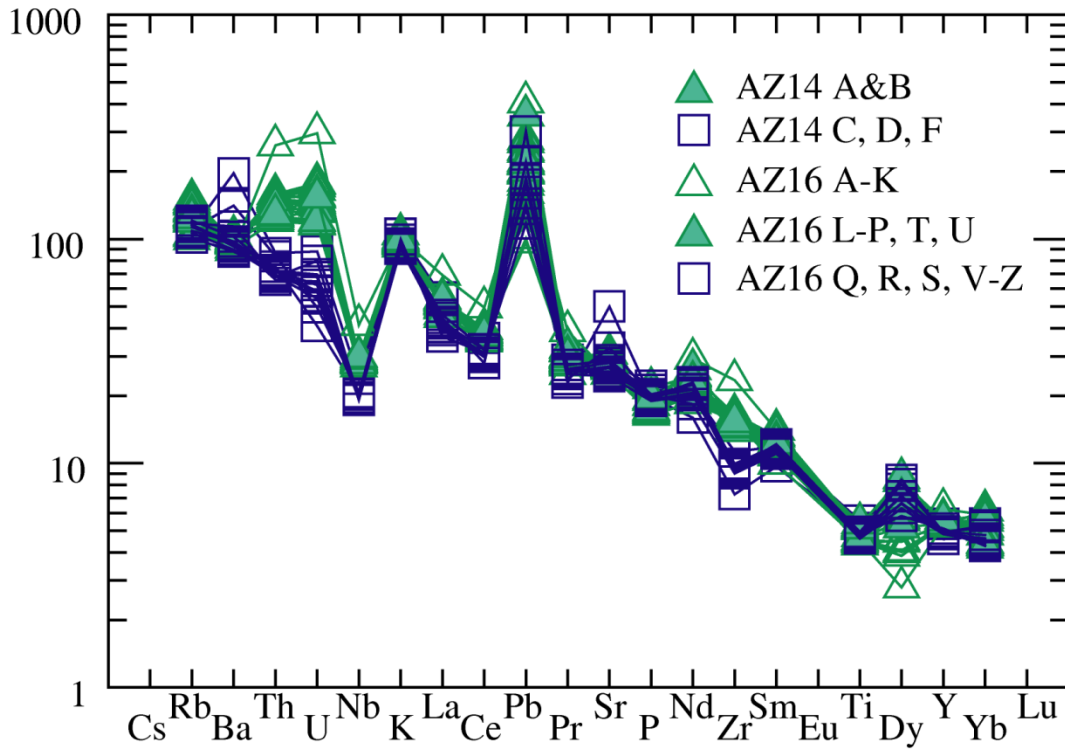
Sample Setting	AZ16F Sill	AZ16F Sill	AZ16G Sill	AZ16H Sill	AZ16I Flow	AZ16J Flow	AZ16K Sill	AZ16L Sill	AZ16M Flow	AZ16N Flow	AZ16O Flow
Major Elements (Wt%)											
Fe2O3	8.81		8.86	8.54	8.63	8.75	8.90	8.94	9.33	9.63	9.01
MnO	0.16		0.16	0.12	0.16	0.14	0.12	0.17	0.12	0.15	0.16
TiO2	0.99		0.98	0.99	0.96	0.98	1.03	0.99	1.13	1.15	1.11
CaO	8.55		8.37	8.70	8.59	8.42	8.66	8.47	9.15	8.49	8.42
K2O	2.93		2.93	2.96	2.89	2.85	3.00	2.97	2.91	2.87	2.94
P2O5	0.37		0.37	0.37	0.36	0.36	0.38	0.38	0.42	0.40	0.40
SiO2	51.92		51.96	52.58	52.45	52.12	52.80	52.63	51.76	51.16	51.18
Al2O3	16.24		16.57	17.04	16.52	16.21	16.65	16.80	16.85	16.48	17.12
MgO	5.73		5.78	4.88	6.30	6.25	4.97	5.89	4.97	6.64	6.00
Na2O	2.61		2.79	2.88	2.82	2.87	2.85	2.85	2.70	2.74	2.91
BaO	0.08		0.07	0.08	0.07	0.08	0.08	0.08	0.08	0.07	0.08
LOI	1.42		0.89	1.07	0.70	0.65	1.08	1.23	1.22	1.14	1.60
Total	98.39		98.86	99.15	99.76	99.01	99.43	100.16	99.44	99.77	99.32
Trace Elements (ppm)											
Ba	683.58	686.70	680.80	681.68	674.46	670.86	677.42	720.99	686.30	640.56	706.46
Ce	64.64	65.53	66.25	68.10	67.49	66.66	70.56	63.89	70.20	62.60	62.07
Co	30.62	30.69	28.72	28.98	28.86	29.56	29.69	31.46	32.04	32.16	29.35
Cr	267.57	268.37	240.79	257.54	242.86	329.55	235.90	203.04	212.61	219.65	183.86
Cu	54.20	54.32	64.55	66.70	61.14	62.54	64.66	69.71	72.11	70.75	74.58
Dy	4.10	3.29	2.06	4.50	4.55	2.85	4.59	3.80	4.74	6.32	4.72
Er	2.64	2.66	2.86	3.50	2.99	2.62	2.62	2.48	2.75	3.35	2.58
Ga	17.88	18.08	18.02	18.66	17.79	17.76	18.32	18.32	18.67	18.17	18.80
Hf	5.60	5.90	5.45	5.78	6.03	5.31	5.48	5.04	5.51	4.98	5.23
La	35.32	35.77	37.32	36.89	35.28	36.26	36.95	35.40	36.53	31.77	30.83
Mo	3.15	2.99	2.10	2.24	1.96	1.96	2.25	1.89	1.69	2.11	2.05
Nb	20.68	20.87	20.06	20.53	20.11	20.71	21.36	20.22	21.32	19.86	19.29
Nd	28.92	28.18	33.02	30.09	30.46	32.11	33.51	26.72	35.56	31.24	29.78
Ni	87.22	87.65	80.75	86.42	80.82	79.78	77.57	85.13	90.27	87.59	80.86
Pb	6.86	7.14	15.29	28.89	14.01	19.22	17.35	15.38	15.26	12.89	15.83
Pr	7.79	7.54	8.79	8.28	7.97	8.30	8.77	7.67	9.03	7.93	7.93
Rb	79.82	79.91	85.46	84.05	80.56	66.49	90.30	86.74	63.31	78.73	81.27
Sc	24.96	25.85	23.01	22.85	24.12	24.43	24.63	24.68	25.69	25.88	23.44
Sm	4.97	4.81	5.84	5.27	5.25	5.51	5.86	4.85	5.95	5.41	5.55
Sr	576.70	578.62	596.24	649.11	608.09	605.15	591.06	573.49	600.98	565.61	570.58
Ta	1.81	1.15	1.94	1.49	0.72	1.24	1.92	1.62	1.80	1.13	1.09
Th	13.15	13.08	13.04	13.10	12.91	13.11	13.48	11.10	11.80	10.24	10.43
U	3.23	3.69	3.29	3.24	2.95	2.79	3.73	2.81	2.80	2.44	2.55
V	200.12	202.20	195.36	195.71	189.20	197.08	201.09	207.42	218.64	225.54	207.13
W	4.39	4.38	5.17	4.43	3.47	3.54	4.12	4.11	3.69	4.05	4.73
Y	24.52	24.55	23.99	24.16	23.92	24.16	25.12	24.60	25.80	24.30	23.74
Yb	2.48	2.57	2.19	2.81	3.03	2.82	2.56	2.38	2.58	2.38	2.07
Zn	73.36	73.15	84.26	89.55	80.71	90.18	84.18	87.12	94.72	93.79	81.78
Zr	178.01	179.21	172.09	173.53	171.16	177.36	185.12	166.17	174.76	160.03	155.78

Sample Setting	AZ16P Flow	AZ16Q Flow	AZ16R Flow	AZ16S Sill	AZ16T Flow	AZ16U Flow	AZ16V Flow	AZ16W Sill	AZ16X Flow	AZ16Y Sill	AZ16Z Flow
Major Elements (Wt%)											
Fe2O3	9.13	9.39	9.07	9.62	8.54	8.64	9.47	9.52	9.35	9.21	9.40
MnO	0.16	0.18	0.17	0.17	0.15	0.17	0.17	0.17	0.18	0.17	0.16
TiO2	1.12	1.02	1.05	1.04	1.11	1.17	1.00	1.05	1.03	1.07	1.07
CaO	8.57	8.51	9.24	8.57	8.65	8.70	8.27	8.50	8.47	8.83	8.51
K2O	2.79	2.73	2.76	2.75	2.90	2.97	2.74	2.88	2.84	3.00	2.81
P2O5	0.40	0.43	0.43	0.42	0.42	0.42	0.41	0.44	0.43	0.44	0.44
SiO2	51.10	50.56	51.09	50.70	51.64	51.78	50.39	51.06	50.70	50.78	50.65
Al2O3	16.59	16.75	16.76	16.21	18.09	17.52	15.85	16.77	16.51	16.51	16.66
MgO	6.44	6.94	5.45	7.27	4.50	4.60	7.71	6.95	6.80	6.72	6.84
Na2O	2.71	2.52	2.65	2.50	2.91	2.88	2.92	2.63	2.53	2.71	2.57
BaO	0.07	0.07	0.07	0.07	0.08	0.08	0.07	0.08	0.09	0.08	0.08
LOI	1.22	2.04	1.30	1.91	1.15	1.03	1.73	2.06	1.89	1.09	1.85
Total	99.09	99.09	98.73	99.31	98.97	98.92	99.01	100.03	98.91	99.51	99.20
Trace Elements (ppm)											
Ba	674.05	614.25	626.14	648.10	676.55	665.80	660.18	678.70	795.31	715.46	681.20
Ce	64.38	54.84	56.88	49.62	68.35	65.58	52.83	54.40	54.20	55.23	57.30
Co	31.11	34.14	33.39	34.82	27.55	30.95	35.11	33.91	33.97	30.72	32.90
Cr	200.81	280.26	288.20	318.44	148.59	236.10	290.84	261.39	264.91	241.03	281.10
Cu	72.58	80.22	83.61	88.34	77.14	75.26	84.57	81.61	85.30	87.67	77.98
Dy	4.70	5.26	4.29	4.86	4.65	5.13	4.64	6.21	4.89	5.24	5.94
Er	2.23	3.46	2.67	3.15	2.77	2.64	2.84	3.35	2.86	2.81	2.94
Ga	18.58	18.32	18.93	17.75	19.87	19.61	17.55	18.03	17.79	17.58	18.16
Hf	5.68	4.12	4.85	4.46	5.74	5.79	4.27	4.50	4.33	3.90	4.38
La	34.99	27.91	29.33	30.52	37.53	36.59	27.74	26.96	28.82	25.22	31.54
Mo	2.41	1.92	1.89	2.21	2.00	2.52	1.97	1.90	1.85	1.99	1.67
Nb	19.87	13.76	14.54	13.67	20.84	21.19	13.85	14.40	13.97	14.52	14.43
Nd	30.04	31.05	28.83	27.93	30.71	31.08	27.20	30.26	27.36	24.87	28.99
Ni	85.08	130.14	125.14	137.38	77.46	98.97	148.93	127.85	118.29	93.47	107.00
Pb	25.22	15.63	12.41	13.26	14.31	15.52	10.23	8.33	21.43	13.04	9.67
Pr	7.91	7.27	7.26	7.10	8.32	8.20	6.90	7.14	7.04	6.55	7.56
Rb	77.06	64.38	67.63	73.27	76.06	78.54	73.80	69.05	74.55	76.65	71.73
Sc	25.41	23.81	26.14	24.33	24.79	24.84	24.01	23.36	24.29	23.91	23.94
Sm	5.19	5.19	5.32	5.01	5.24	5.43	5.03	5.12	4.98	4.90	5.40
Sr	567.64	541.19	591.30	560.46	631.49	598.89	515.82	527.39	570.42	690.53	607.11
Ta	2.01	1.96	1.60	2.63	1.67	1.30	1.33	2.18	2.40	1.21	1.48
Th	10.74	6.15	5.89	6.03	10.79	10.93	5.76	5.60	5.83	6.09	6.17
U	2.53	1.46	1.22	1.42	2.53	3.22	1.68	1.36	1.14	1.23	1.31
V	217.30	211.69	225.24	215.86	202.52	226.51	207.60	208.30	211.68	212.96	219.33
W	3.48	3.43	3.68	4.87	2.88	4.63	5.24	3.46	3.18	4.60	2.09
Y	24.78	22.19	23.26	21.97	24.40	25.31	22.00	22.36	22.30	22.58	22.39
Yb	2.17	2.16	2.11	2.20	2.73	2.12	2.28	2.56	2.26	2.36	2.60
Zn	91.72	83.44	92.05	82.55	94.17	97.69	78.49	78.52	79.67	81.40	80.75
Zr	161.47	106.83	111.37	103.15	163.97	170.65	107.36	109.60	106.99	101.02	105.12

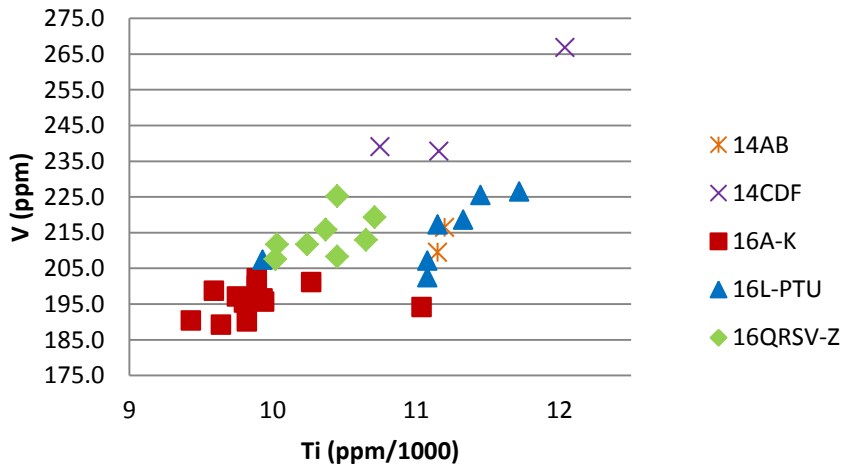
Table 6: XRF data of all basalts of section AZ14 and AZ16

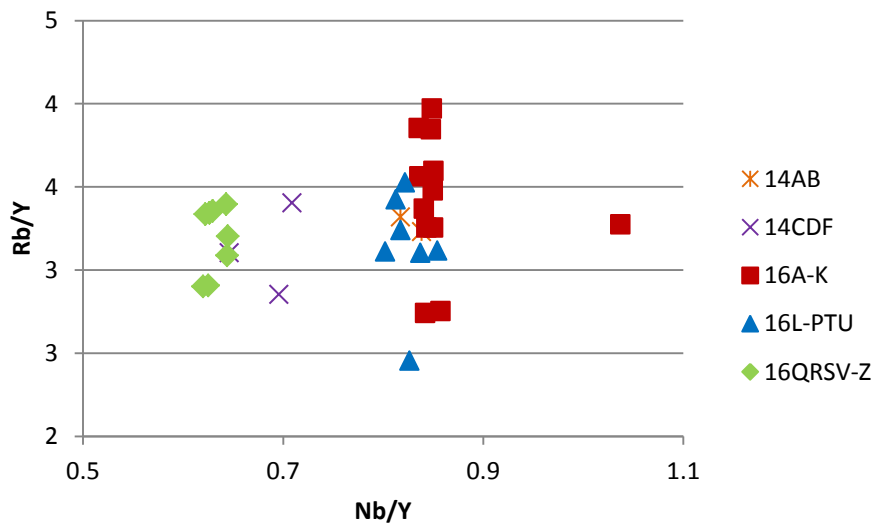
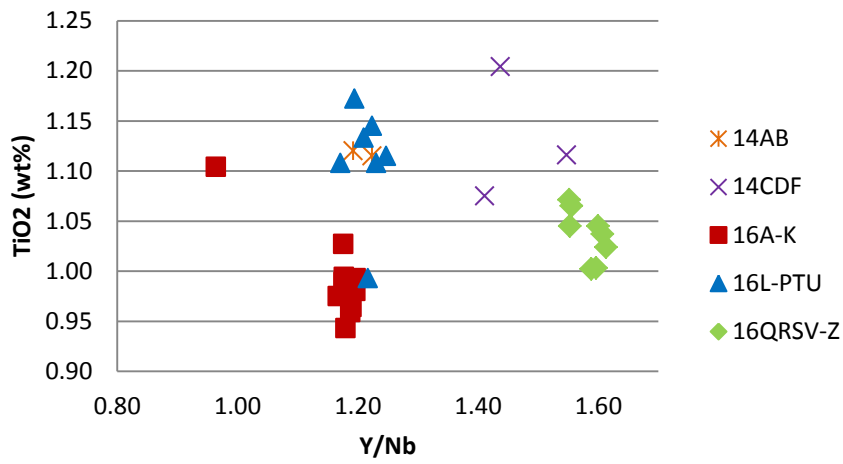
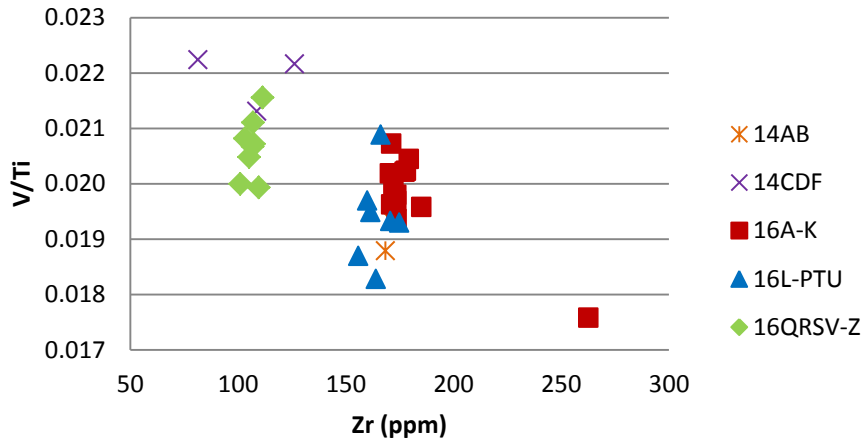
Rock/Primitive Mantle

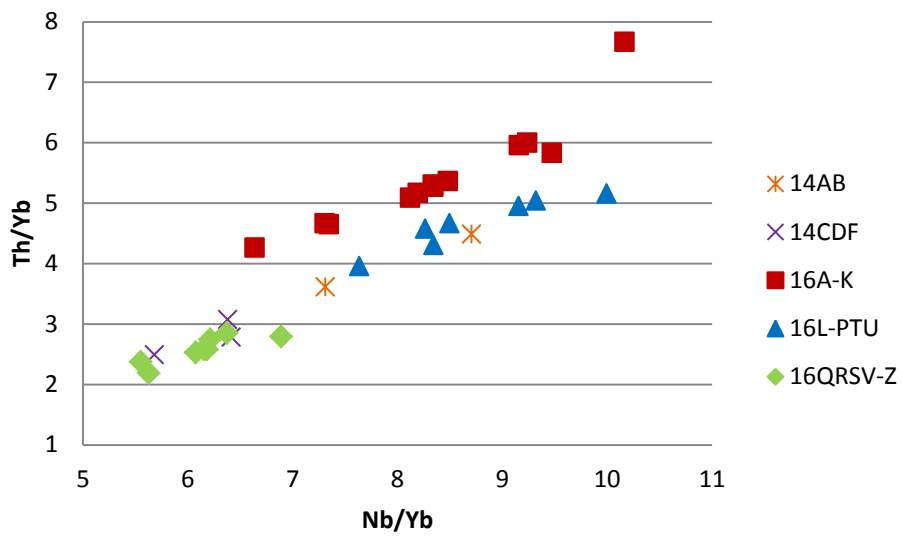
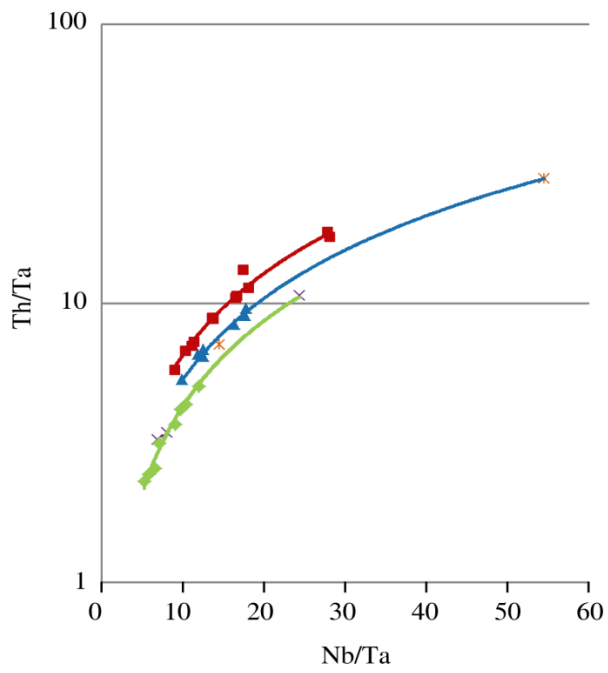
Sun/McDon. 1989-PM

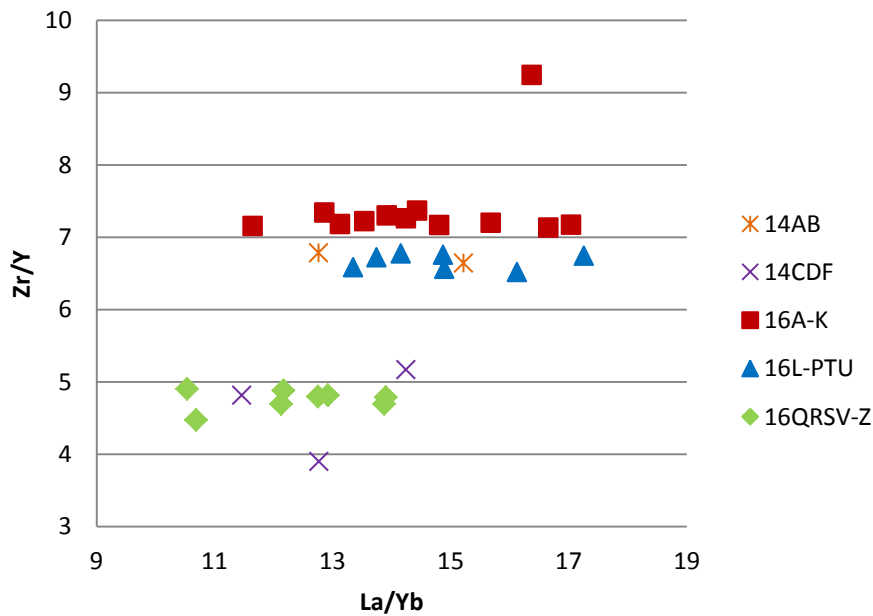
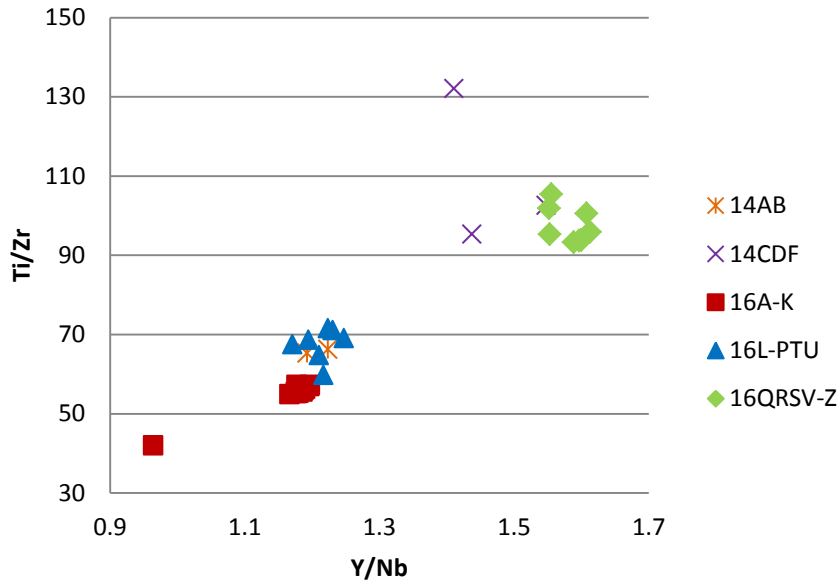


Primitive mantle normalized spider diagram (normalization values of Sun and McDonough (1989))





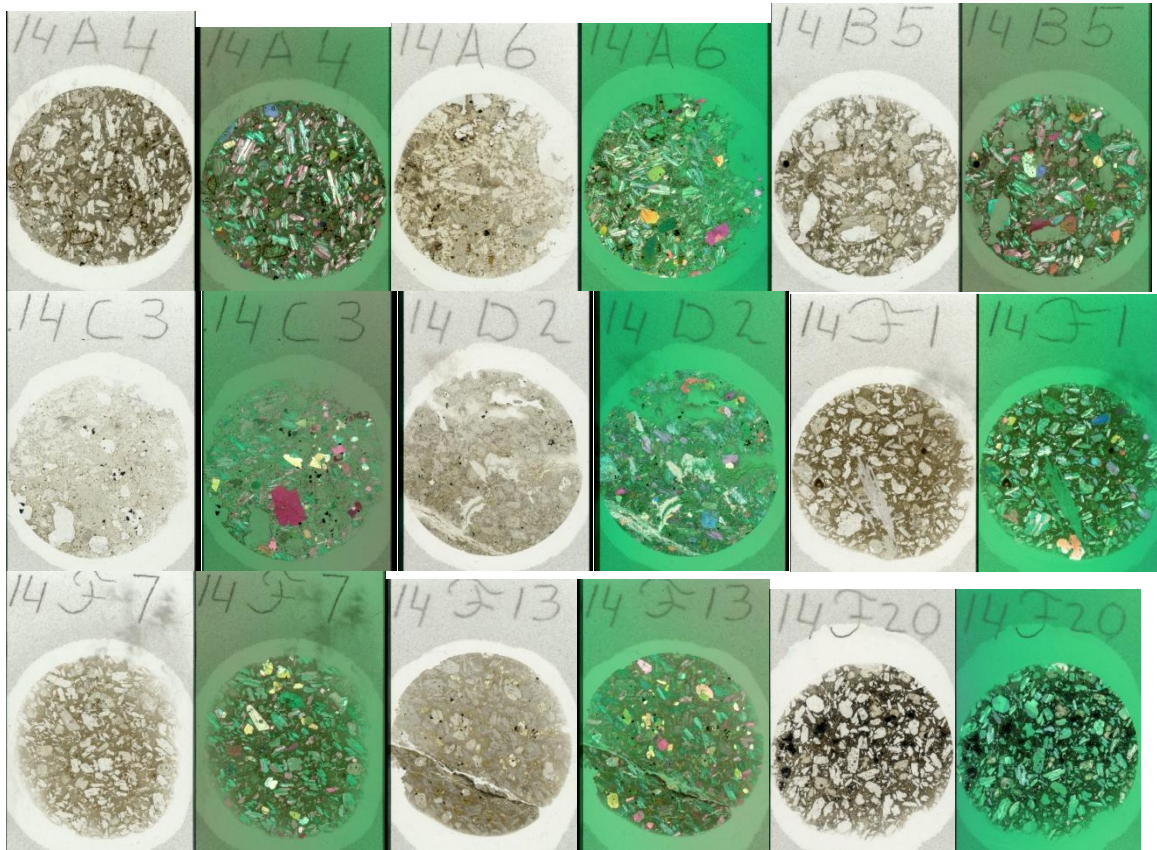


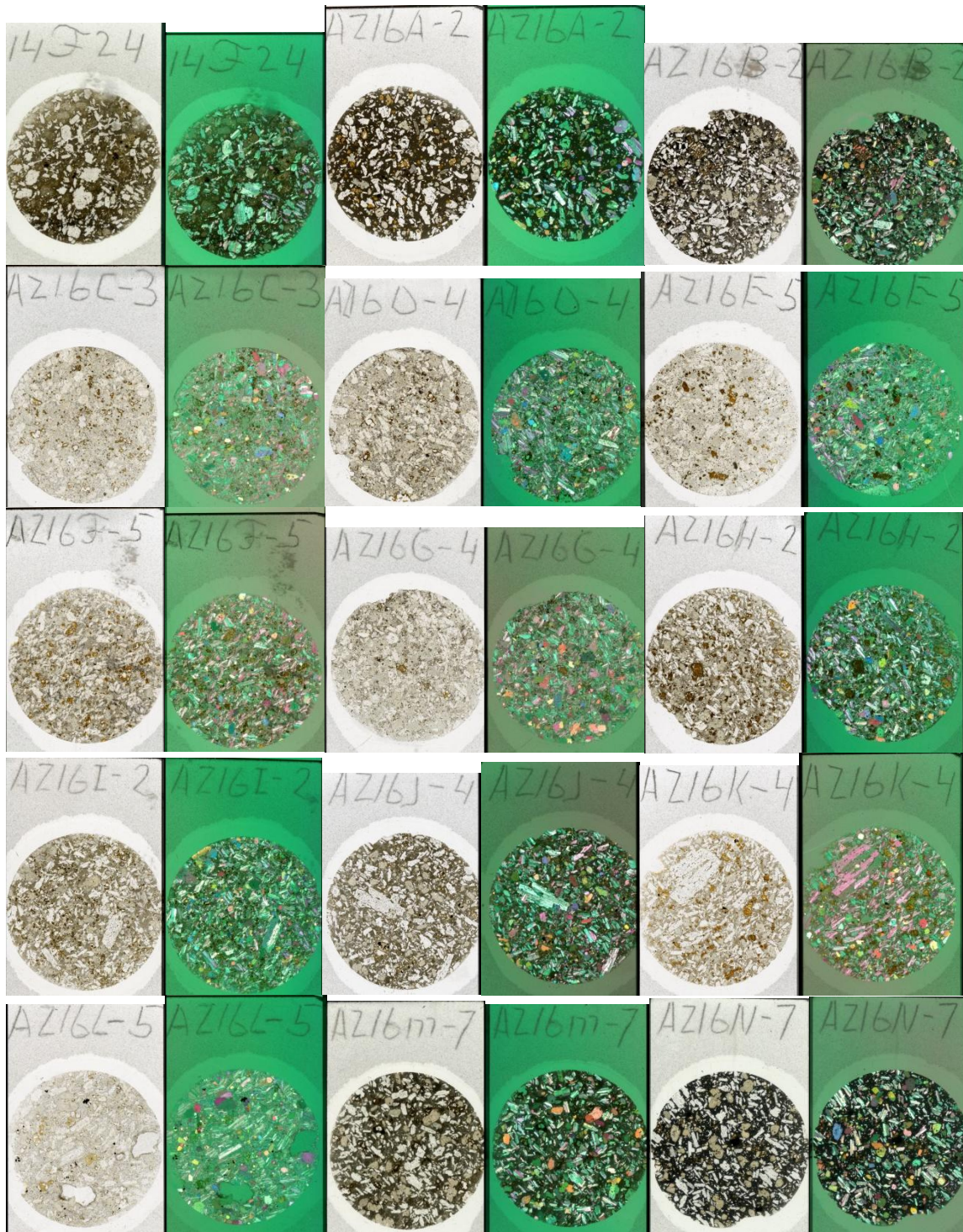


Summary of problems during XRF sample preparation

A cylinder with compressed air that rotates the dishes was broken. This however, is very unlikely to cause any measuring inaccuracies, as the rotation of the beads takes place after solidification of the beads. The platinum casting dishes were not flat anymore, causing beads to break very often. Normally, beads were not molten again, but a new casting powder was created. Only samples 16G and 16L were remelted using a program for broken beads, which does not include any oxidation steps. Casting dishes being unflat also lead to casting errors, causing the machine to run the melting program completely, but no casting happened, as the sensor was unable to detect the casting dish. In this case, the program was

restarted using the solidified melt. As the melt is at the temperature of 1200°C for longer, the amount of a certain element that is lost at that temperature might be larger. This can affect for example the amount of S, and possibly also the amounts of F, Na, Mg and P. This happened for sample 16B, which was melted 2 times before casting, and sample 16G, which was melted 4 times before casting. Another problem was that the sleeve that holds the platinum crucible was missing the 2 pins that keep this sleeve in place. The sleeve has to be exactly in the right position, in order for the temperature of the crucible to be measured. This happens through a hole in the sleeve. If the sleeve is slightly turned, the sensor measures the temperature of the sleeve instead of the temperature of the crucible. This temperature is lower than the temperature of the crucible, causing the machine to heat up the crucible too much. This might cause a loss in F, Na, Mg, P, and other light elements. However, it is not retraceable if (and if so, which) any samples were heated up too much. As the platinum dishes were not completely flat, the beads have a slight bulge. Thus, when measuring, the distance of the sample to the X-ray tube is not defined exactly, which might lead to measuring errors. From sample 16P onwards, the platinum dishes were flattened and polished (16P was cast on a flattened but unpolished dish), the compressed air cylinder was fixed, and the pins that keep the sleeve in place were restored. Thus, the results of 16P-16Z are more reliable than the results of 14A-14F and 16A-16O. After assessment of the first major element results, it was decided to make 16C, 16F and 16X again, as the total amount of major elements added up to less than 98%. These samples were also made in the flat dishes when the machine was repaired, so these three samples also have more reliable results.





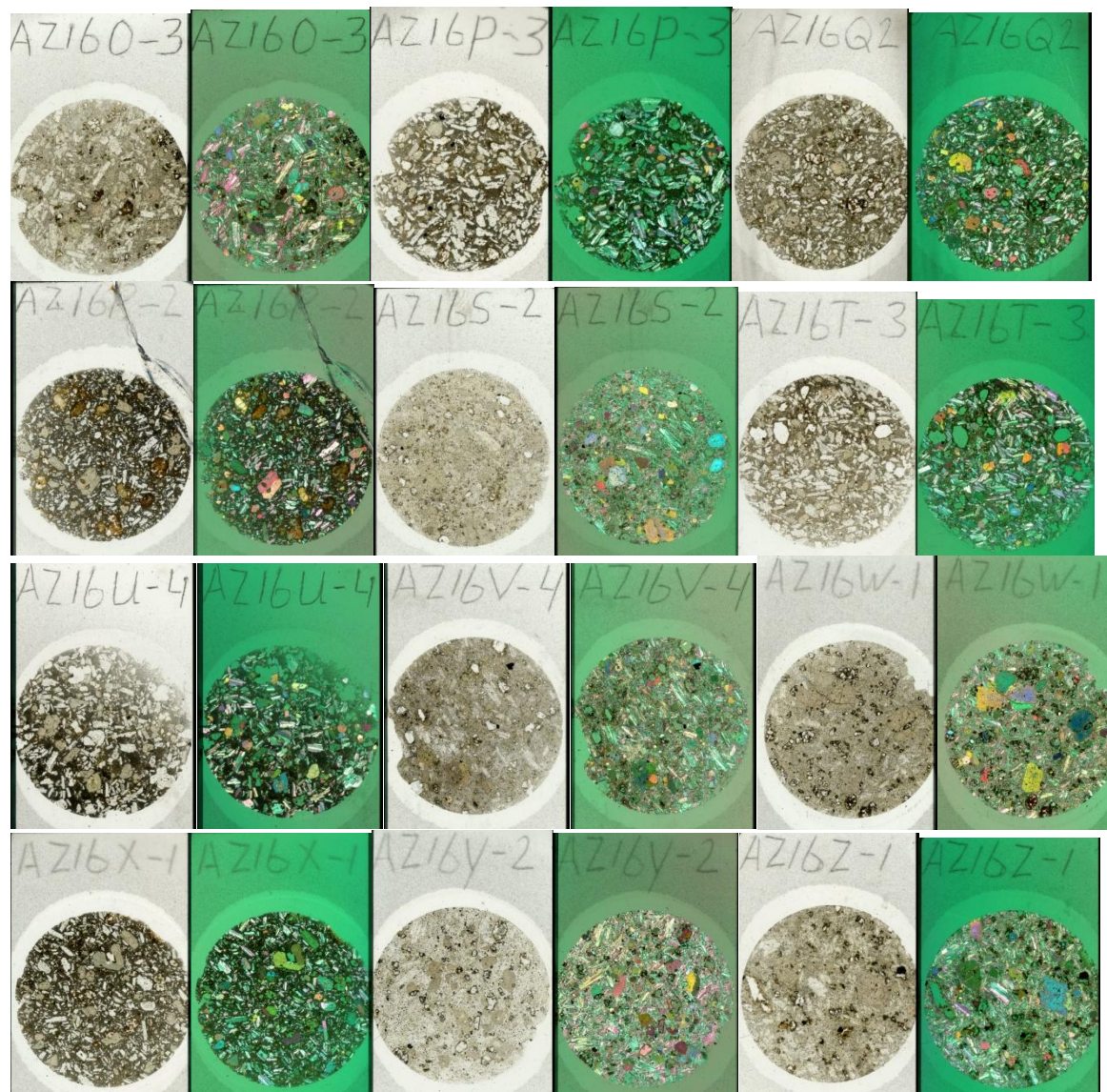


Figure 29: Scans of all thin sections of AZ14 and AZ16 in both plain-polarized and cross-polarized light (green background). Cross-polarized colors are unusual.

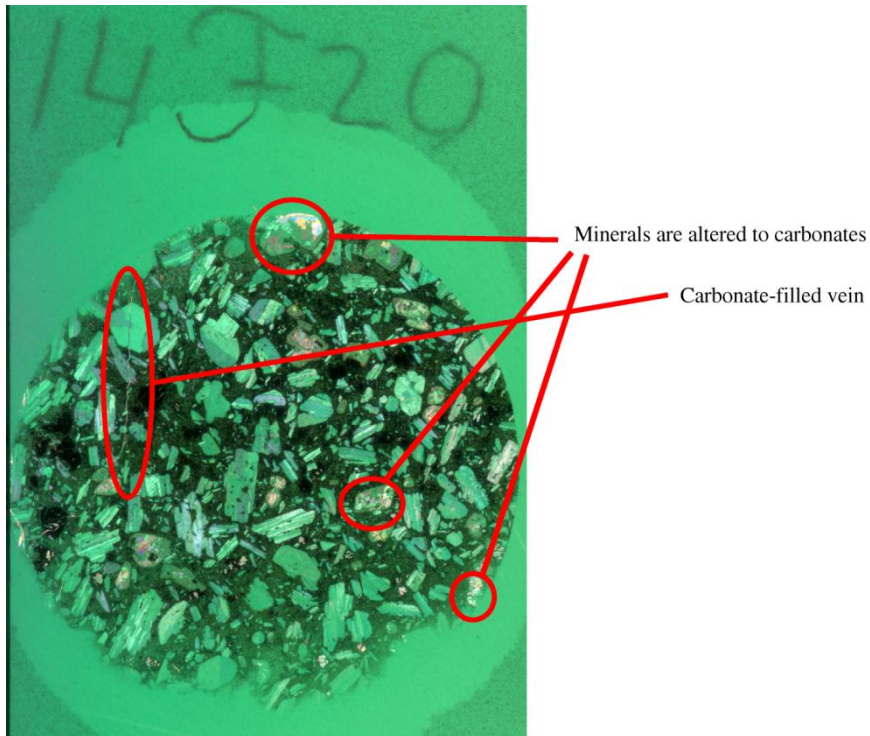
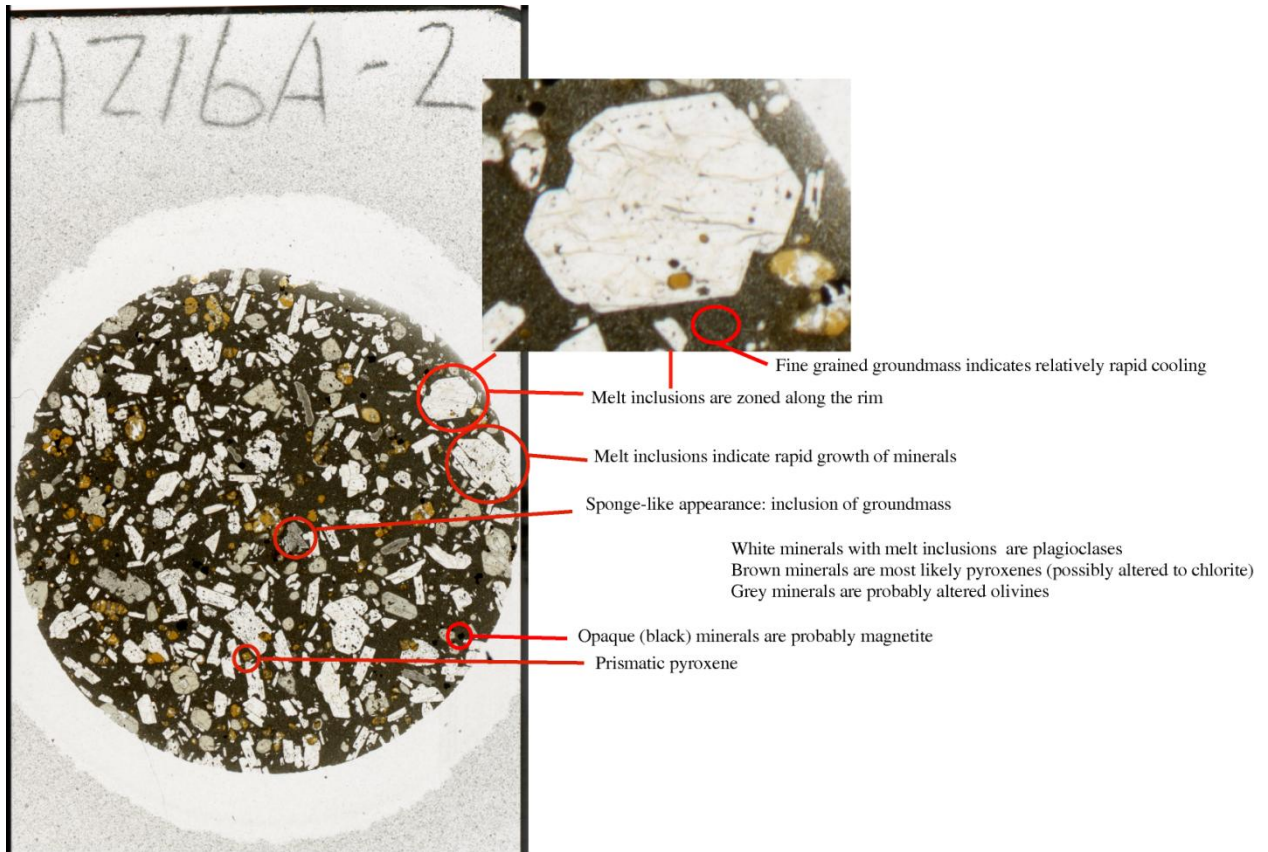


Figure 30: Thin section of AF16A.2 in plain-polarized light and AZ14F.20 in cross-polarized light

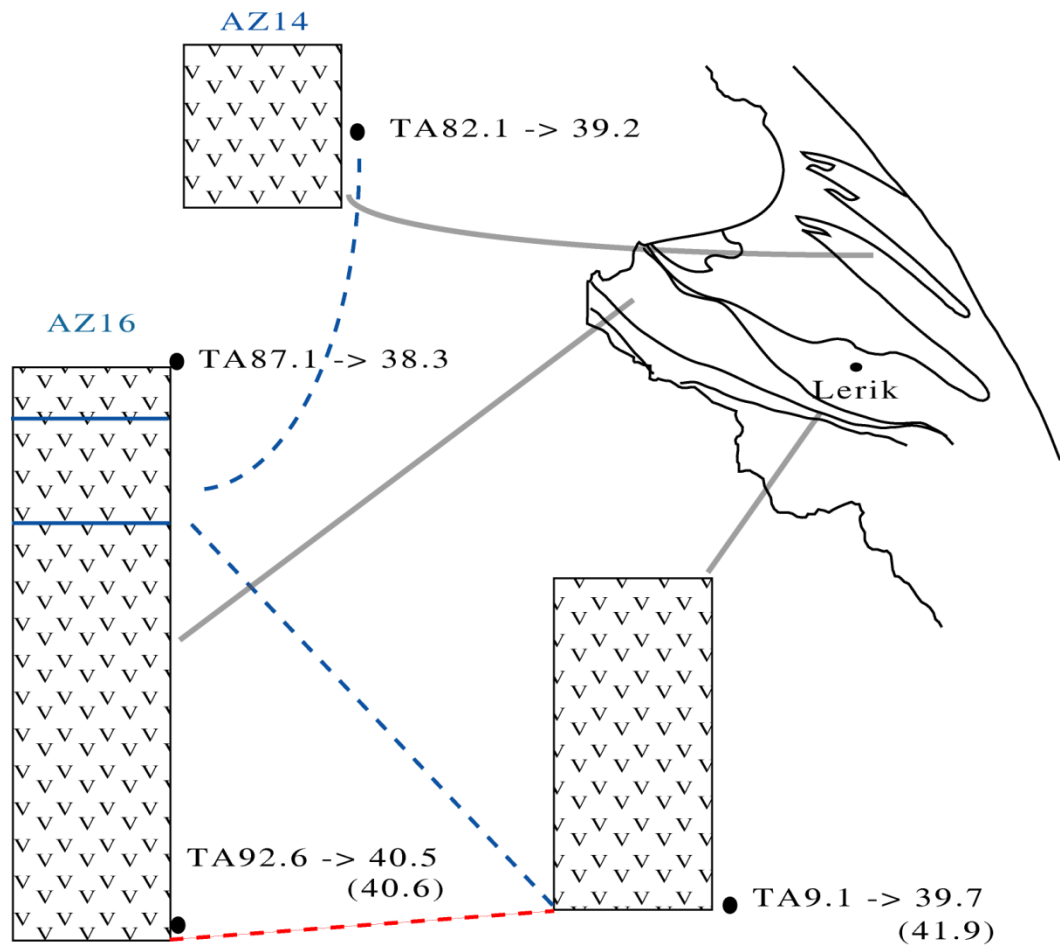


Figure 31: Ar-Ar ages of Vincent et al. (2005) used to date the three groups